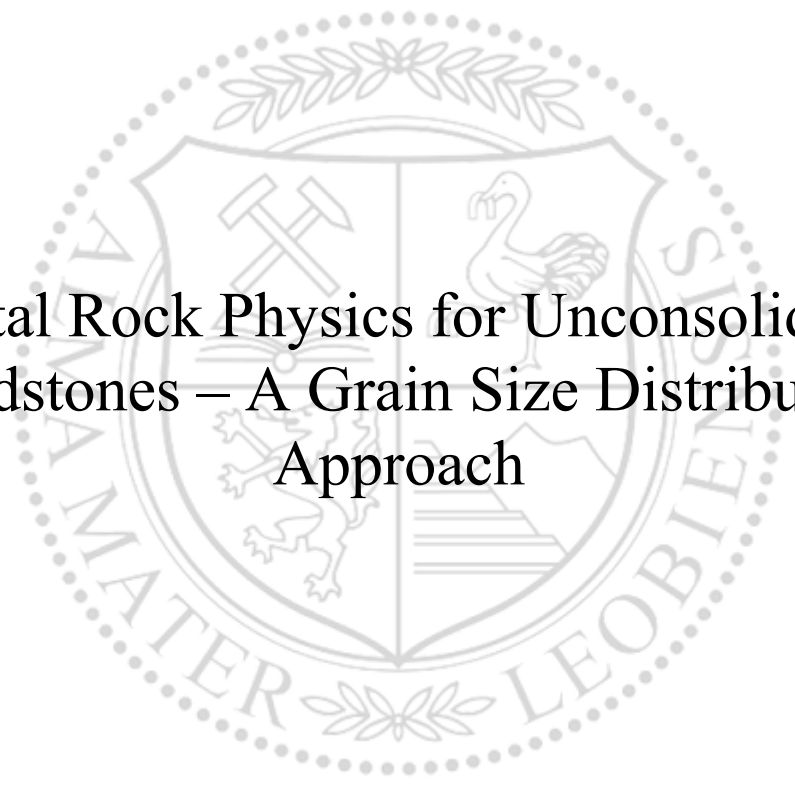Chair of Reservoir Engineering

Master's Thesis

Digital Rock Physics for Unconsolidated Sandstones – A Grain Size Distribution Approach

Alexandru-Mihai Badescu

December 2020

EIDESSTATTLICHE ERKLÄRUNG

I declare on oath that I wrote this thesis independently, did not use other than the specified sources and aids, and did not otherwise use any unauthorized aids.

I declare that I have read, understood, and complied with the guidelines of the senate of the Montanuniversität Leoben for "Good Scientific Practice".

Furthermore, I declare that the electronic and printed version of the submitted thesis are identical, both, formally and with regard to content.

Datum 01.12.2020

Signature Author
Alexandru-Mihai Badescu

Alexandru Badescu

Master Thesis 2020
Supervisor: Univ.-Prof. Dipl.-Phys. Dr.habil. Holger Ott
Co-supervisor: Dipl.-Ing. Pit Arnold
Industry advisor: PhD. Hendrik Rohler

Digital Rock Physics for Unconsolidated Sandstones – A Grain Size Distribution Approach

dpe DEPARTMENT PETROLEUM ENGINEERING

MONTAN UNIVERSITÄT

Dedicated to my parents and brother

Acknowledgements

I want to thank Prof. Holger Ott for his supervision throughout the development of this thesis, together with his vast knowledge offered in the area of Reservoir Engineering. Also, I want to thank Pit Arnold for the continuous support provided during the completion and review of this work together with the constructive discussions had on the topic of Digital Rock Physics.

Besides, I want to thank Dr. Hendrik Rohler and the OMV Petrom for providing the materials needed for the research and completion of my degree.

Finally, I want to thank my family, mentors and close friends who supported me during my studies. Many thanks to my parents for support in the last months, both moral and financial. Special thanks to my mentors Diana Nitescu, Stephan Hannke and Allen Bertagne, who always supported me in all my endeavours and who believed in me. From my friends I want to mention Roberta Cocos, Viktor Gredičak, Patrick Jasek and Marius Nitu for being there for me when I needed them for support.

Abstract

The setup of a digital rock model from 3D CT scans and 2D thin sections to derive petrophysical and multiphase flow properties has gained influence over the years. Primarily due to the improved computational power and scanning abilities, the replication of rocks in a 3D computational environment is widespread available. Through Digital Rock Physics (DRP), it is possible to derive petrophysical and multiphase flow properties, which are typically obtained by traditional methods such as routine core analysis or special core analysis, from a digital model. The technique proposes an alternative for unconsolidated sandstones, where the rocks are friable and often unusable for conventional methods. Unconsolidated reservoirs have often only limited information available, therefore grain size distributions obtained by sieving analysis are used as basic input.

The goal of this thesis is the development of a workflow to set up a model of an unconsolidated rock sample to evaluate multiphase flow processes. The main focus of this study is put in building models on basis of grain size distribution, assuming it to be the least amount of information available. As a result, the sensitivities of grain size binning, shape and orientation are investigated. The data used was provided by OMV Petrom.

The objective of this work is to obtain the pore throat size distribution as close as possible to the real rock using reconstructed 3D models and simulating MICP experiments in a computational environment (GeoDict).

The work here was conducted on rocks generated randomly on grain size statistical data and using the pore morphology method (Hilpert and Miller, 2001) to simulate the phase distribution inside the rock. By varying the original grain size distribution in different bins, models were created with both spheres and ellipses. Parameters like shape, grain dimensions, anisotropy and variations in bins were studied and ranked on how they are influencing the results.

In the end, the parameter that dramatically influences the improvement of the model is the choice of different shapes for the grain generation. Moreover, the simulation proved that using a model based on grain size distribution manages to match the pore throat sizes. Consequently, with better optimization of the workflow on matching the whole capillary pressure curve, crucial information for flow characterization like relative permeabilities, and capillary pressures can be extracted.

Zusammenfassungc

Digitale Gesteinsmodellierung, mit Hilfe von 3D Computertomografie und 2D Dünnschnitten zur Bestimmung petrophysikalischer und mehrphasenströmungsbedingter Eigenschaften, gewann über die letzten Jahre an Relevanz. Es ist in erster Linie der stärkeren Rechenleistung von Computern und dem Fortschritt in der Messtechnik verdankt, sodass 3D Gesteinssimulationen gut verbreitet sind. Durch digitale Gesteinsphysik (DGP) hat die Erdölindustrie eine schnellere Möglichkeit gewisse Eigenschaften, im Vergleich zu konventionellen Methoden wie die routinemäßige Bohrkernanalyse oder spezielle Bohrkernanalyse, herzuleiten. Das Verfahren kann bei nicht konsolidierten Sandsteinen angewendet werden, wo das bröckelige Verhalten des Gesteins Schwierigkeiten bei bisherigen Methoden hervorruft. Dennoch sind Studien über Gesteinsmodellierungen, mit dem Fokus auf Korngrößenverteilungen aus Siebanalysen, nicht weit verbreitet.

In dieser Arbeit wird eine Methode für die schnelle Evaluierung der Transporteigenschaften, in nicht konsolidierten Sandsteinen, welche durch Lagerstättenlaborstudien nicht hergeleitet werden können, konzipiert. Des Weiteren wird sich die Studie auf Korngrößenverteilungen, unter der Annahme, dass diese eine einfache und kosteneffektive Informationsquelle darstellt, konzentrieren. Der Datensatz, der von OMV Petrom zur Verfügung gestellt worden ist, besteht aus nicht konsolidierten Sandsteinen die eine Evaluierung auf Permeabilität und kapillare Drücke benötigen.

Das Ziel ist eine möglichst realitätsgetreue Porendistribution zu erhalten, basierend auf rekonstruierten 3D Modellen und Strömungssimulationen aus Experimenten in einem Computerprogramm (GeoDict). Hierzu muss ein Arbeitsablauf kreiert werden der die 3D Gesteinsmodellierung für nicht konsolidierte Proben, basierend auf Korngrößenverteilungen, durch die Transporteigenschaften im porösem Medium adäquat repräsentiert. Durch Generalisierung des Modells können die Befunde dann auf alle nicht konsolidierten Gesteine angewandt werden, um Porenraumevaluierungen schneller zu gestalten.

Die Arbeit wurde auf Gesteinsproben bezogen, welche mit zufälliger Korngrößenverteilung generiert wurden. Mit der Porenmorphologiemethode (Hilpert und Miller, 2001) wurde die Phasendistribution im Gestein simuliert. Durch Variierung der originalen Korngrößenverteilungen in multiplen Stufen wurden Modelle mit sphärischer und elliptischer

Körnung erstellt. Parameter wie Form, Korndimensionen, Anisotropie und die Variierung in Stufen wurden bewertet, um die Auswirkung auf die Resultate zu analysieren.

Letztendlich zeigte sich, dass die Simulation mit Hilfe von Korngrößenverteilungen, übereinstimmende Porenhalsdimensionen aufweisen. Durch Optimierung des Arbeitsflusses kann die Modellierung wichtige Information über Strömungscharakteristiken, wie relative Permeabilität und kapillare Drücke, extrahieren.

Stichwörter: Korngrößenverteilung, MICP, Digitale Gesteinsphysik, Porenmorphologiemethode, Porenhalsradius, Transporteigenschaften, Relative Permeabilität

Table of Contents

List of Figures

List of Tables

Nomenclature

θ	Contact angle	[°]
r	radius	[m]
σ	Interfacial tension	[N/m]
P	Pressure	[psi]
S_w	Wetting saturation	[-]
S_{wirr}	Irreducible wetting saturation	[-]
$S_{pn\text{-}w}$	Non-wetting phase saturation	[-]
$S_{rn\text{-}w}$	Residual non-wetting saturation	[-]
L	Length	[m]
A	Area	(m)
K	Permeability	[mD]
ρ	density	[kg/m^3]
Q	Flow rate	[m^3/s]
$\vec{f}$	Applied body force	[N]
μ	Viscosity	[cp]
$\vec{u}$	Flow velocity	[m/s]
d_k	Unit vector of direction	[-]
T	Orientation tensor	[-]
n	Number of grains	[-]

Abbreviations

CT	Computer Tomograph
DRP	Digital Rock Physics
FIB-SEM	Focused Ion Beam - Scanning Electron Microscopy
GSD	Grain Size Distribution
HPMI	High Pressure Mercury Injection
LIR	Left Identity Right
LPM	Low Pressure Manual
MICP	Mercury Injection Capillary Pressure
NRMSE	Normalized Root Mean Square Error
NWP	Non-Wetting Phase
PSD	Pore Size Distribution
REV	Representative Elementary Volume
RMSE	Root Mean Square Error
SVP	Solid Volume Percentage
XRD	X-Ray Diffraction
WP	Wetting phase

Chapter 1

Introduction

In every aspect of exploration and production, every petroleum engineer must know the rock and fluid flow properties of a given field. Only by understanding the physics that are governing the underworld, the reserves can be economically evaluated, and the reservoir can be assessed suitable for a future secondary or tertiary recovery flooding process. For this, rocks need to be studied, both statically and dynamically. One way to do it is through core analysis. Cores are extracted during exploration/appraisal phases, and they are analyzed for specific properties like porosity, permeability, grain size distribution, formation factors, cementation/saturation exponents, resistivity index and mineralogical properties.

Core analysis offers a quantitative measurement of oil and gas reservoir properties. It delivers the foundation of formation evaluation in building the static and dynamic reservoir models (McPhee, Reed and Zubizarreta, 2015). Estimating the relative permeability functions accurately is a necessary input for reservoir modelling in the pursuit of reliably evaluating fluid movement and designing or optimizing oil recovery processes Relative permeability varies differently inside the reservoir based on the pore structure, interaction between the fluids and rock-fluid. Traditional methods to determine relative permeabilities include the unsteady state, steady-state, and centrifuge method. Such methods are time-consuming and difficult to perform for unconsolidated rocks. The simulation of multiphase flow parameters on 3D digital rock models proposes an alternative to those experiments. Therefore, the questions arise whether it is possible to create those models for unconsolidated rocks and run simulations directly on them without the need to perform the lab measurement. This thesis will try to see how much information can be obtained from 3D models that are based on grain size distribution.

1.1   Background and Context

Unconsolidated sandstones pose difficulties in analyzing the probes for rock and fluid properties. They are very common for oilfields with a significant occurrence in the North Sea (Nordland Group Formation) and basins in Romania. In this study, the case from a Romanian field is investigated. OMV Petrom provided the data from a Romanian oilfield. The oilfield is currently in production.

Drive for such research came from the fact that these types of rocks are some of the most challenging material to work on within core analysis. Engineers have troubles to obtain results which accurately describe the reservoir properties. Extreme care must be taken during every step of coring, handling, transportation, and preparation of them. Even so, additional equipment and procedures are needed to be designed to minimize the sample disturbance. Some of these techniques were developed in the '60s by Ben Swanson and Gene Bowen and implied freezing the core material (Rosen *et al.*, 2007). However, these methods are time-consuming and taken into account the time to perform the experiments; it is difficult to assess the rocks rapidly.

1.2   Scope and Objectives

The thesis is trying to solve these limitations by using 3D models of reconstructed rocks and simulating the MICP experiment in a computational environment (GeoDict). The main goal of this thesis is to create a workflow in generating 3D rock models for unconsolidated probes, based on grain size distribution that can adequately represent the transport properties of the porous media. Grain size distribution is one of the most common pieces of information that can be quickly extracted. The workflow for creating this model should be then applied to any unconsolidated rock and help with the evaluation of the reservoir.

Chapter 2

Literature Review

Before diving into the practical part where the workflow was developed along with a presentation of the results obtained, the mercury injection capillary pressure method and sieve analysis technique is introduced. Furthermore, Digital Rock Physics procedures and previous work conducted in generating 3D rock models are presented with an emphasis on direct modelling methods (Blunt *et al.*, 2013).

2.1 MICP test for determination of drainage capillary pressure

For the development of the workflow, the capillary pressure curve obtained from mercury injection capillary pressure (MICP) experiments will be used as quality control. Capillary pressure distributions in a reservoir determine the distribution of saturation, therefore resulting in the volume of fluids (oil/water/gas) filling the pores. Good knowledge of the capillary pressure distribution helps in the reliable estimation of the hydrocarbon reserves (McPhee, Reed and Zubizarreta, 2015).

For a water-wet rock, the features of drainage and imbibition capillary pressure curve can be seen in Figure 2.1. For the water-wet case in drainage, the pressure is required for the non-wetting hydrocarbon phase to displace the initially pore-filling water in order to reach the irreducible water saturation, S_{wirr}. After that, if the rock is exposed to water at the irreducible saturation, it will spontaneously imbibe and achieve a specific water saturation at zero capillary pressure along with a non-wetting hydrocarbon phase saturation S_{pn-w} (King *et al.*, 1986). This is called a spontaneous (positive or static) primary imbibition. To get the irreducible oil saturation, pressure must be applied to the wetting phase. This is called the forced imbibition.

Usually, water is the wetting phase in most of the reservoirs, as the depositional environment is believed to have been occupied by water. Therefore, the desaturation curve from 100% to S_{wirr} is referred to as the primary cycle, and the increase from S_{wirr} to S_{m-w} is referred to as primary imbibition indifferent of the wettability of the system. The way of testing the capillary pressure is done through 3 methods: centrifuge capillary pressure, semi-permeable membrane (porous plate) and last but not least, the mercury-air (mercury injection). Since tests are run in a laboratory, some corrections need to be done using the two parameters (IFT and contact angle). Typically, the diameter of the plugs analyzed is between 1" and 1.5".
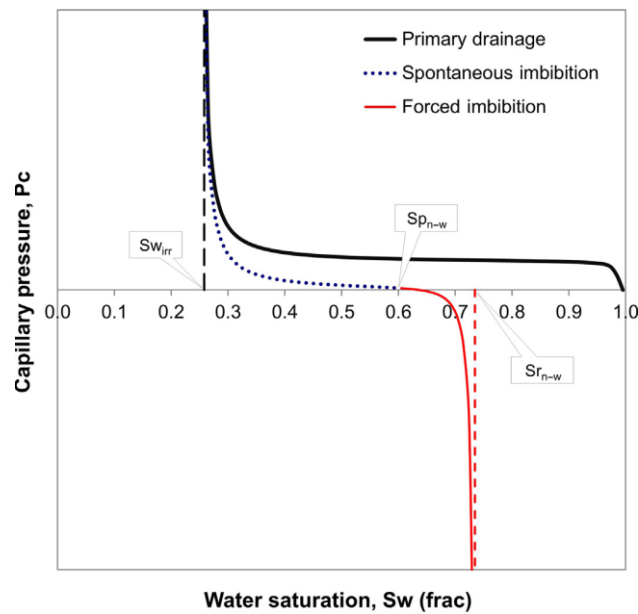
Figure 2.1 Example of primary drainage and imbibition capillary pressure curves (McPhee, Reed and Zubizarreta, 2015)

The most important things that a primary drainage capillary pressure test offers are information about reservoir quality, pore throat size distributions, wetting characteristics and predicting fluid saturations in the reservoir versus height. In the current study, the interest is on the pore throat size distribution.

The mercury injection capillary pressure (MICP) experiment involves injecting mercury into an emptied and dry core sample under a controlled pressure (capillary pressure). Mercury is treated as a non-wetting phase fluid which displaces the air considered here to be the wetting phase. The "displacement" term is misused though, as the air is compressed until no more air exists in the probe. The volume of mercury injected at each pressure steps determined the phase saturation (S_{Hg}), while 1-S_{Hg} defines the wetting phase saturation. It requires only a few hours (up to 8h) to perform rather than days or weeks in the porous plate technique method. There are two types of tests, low-pressure manual (LPM) and high-pressure mercury injection automated

(HPMI) which are used. In the case of the data set received from OMV Petrom, an automated high-pressure system was used.

2.1.1 High-pressure mercury injection (HPMI)

During this test, the injection pressure can go up to 60000 psi and therefore get information about the smallest size pore possible and all the connected flow paths. Some drawbacks of this tests are represented by the fact that there might be errors at high pressures with regards to water saturation/capillary pressure measurements. Another thing is that no irreducible wetting phase saturation is obtained as air will be compressed at high pressure, and the pore volume will be filled with mercury. In the end, the probe will be unusable as mercury will be retained in the sample.

The probes need to be cleaned by Soxhlet extraction and dried in the oven, at the start of the experiment. This is done for the complete removal of clay bound water from the system. The automated mercury porosimeter can accurately generate capillary pressure. Such equipment can be seen in Figure 2.2. The probe is contained in a penetrometer, which consists of a sample cup with an electrical contact cap where the analyzed material is placed. It is connected to a metal-clad, precision-bore, glass capillary stem. More information about the procedure can be found in the book of McPhee (McPhee, Reed and Zubizarreta, 2015).
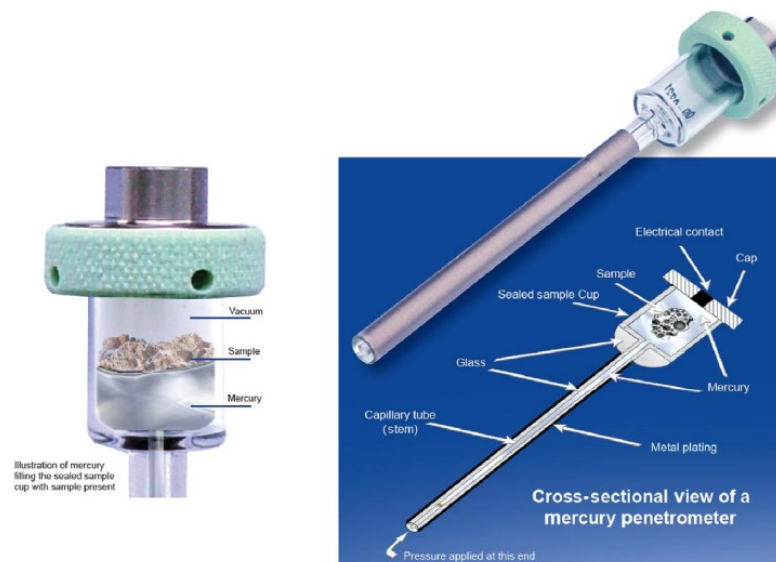
Figure 2.2 Schematic of automated mercury injection high-pressure penetrometer. (McPhee, Reed and Zubizarreta, 2015)

2.1.2 Pore Throat Size Distribution

After the experiment is completed and the capillary curve is obtained, the pore throat sizes can be extracted (Pickell, Swanson and Hickman, 1966; Swanson, 1979). As the high-pressure mercury injection tests result in a significant number of data points, they are preferred to define the pore throat size distribution relationship. Based on the Young Laplace equation radius of a pore throat can be calculated (2.1), where Pc is capillary pressure in Pa, σ is the IFT, between mercury and air in N/m, θ is the contact angle(degrees). At the same time, r is the pore throat radius (micron).

$$Pc = \frac{2\sigma\cos\theta}{r} \qquad (2.1)$$

Plotting the pore throat radius penetrated by mercury at a given capillary pressure against the fractional saturation of the wetting phase is used to show the pore size distribution. This is of importance as it helps to also compare the pore throat radius distribution from the experimental and modelled rock. The pore fractional pore volume injected is equal with the difference of wetting saturation between 2 points (McPhee, Reed and Zubizarreta, 2015).

The formula is presented below:

$$PSD = \frac{dS_w}{d[\log(r)]} \qquad (2.2)$$

2.2   Sieve Analysis

The sieve analysis represents another piece of information used in the study of the rock models. The grains diameter embodies in this case, the input data for the 3D models. To obtain the grain size distribution, a sieve is used. Other methods recently discovered and used are laser diffraction method (Di Stefano, Ferro and Mirabile, 2010) or laser granulometry (Celia Magno *et al.*, 2018). In the presented case, the data was done using a sieve sifting. The sonic sifting method was first introduced in the '60s when Charles Ward patented the technique. (Ward, 1962). The procedure is relatively simple. Grains are placed in the upper part of the apparatus and will fall through the sieves by using sound energy. Sound waves are creating a column of air to lift and separate the fine particles. The smaller grains diameter will fall through, and each sieve will retain a specific volume. Using this volume, the percentage of grains between each sieve interval can be approximated. Of course, there is a degree of uncertainty in how many of

the smallest sizes grains do not pass the sieve based on the timeframe in which the sieving occurs and the shifting.
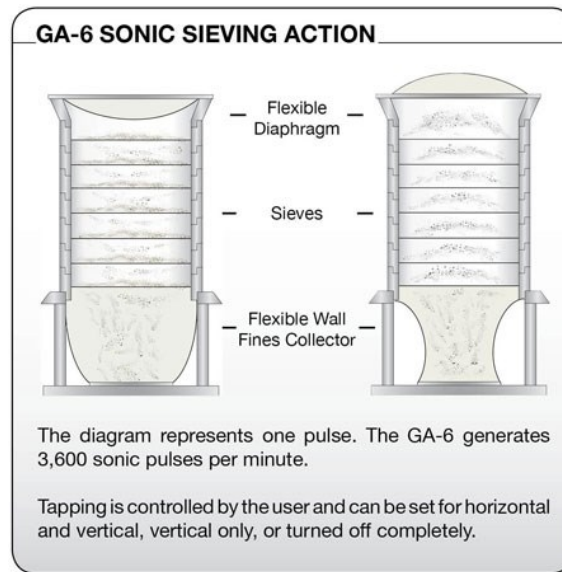
Figure 2.3 Sieving apparatus (Ward, 1962)

2.3   Digital Rock Physics

Getting around the initial parameters that are going to be used, the next step is to create 3D models of the rock that will be based on the grain size distribution, and quality checked using pore space information from capillary pressure. For the generation of the models, the technique of digital rock physics is used. Some papers describing the overall advancement in this area are from Blunt and Berg (Blunt *et al.*, 2013; Berg, Lopez and Berland, 2017). There is a broad description of the methods of imaging and model generation techniques. Although imaging methods will not be used, some of those model generations will be employed here.

On short, DRP is a rapidly growing domain in academia but also the oil and gas industry. The goal of DRP is to calculate petrophysical measurements that cannot be performed for specific reasons in a lab, in an acceptable time frame. Some of these measurements include permeability absolute and relative, capillary pressure and electrical and acoustic rock properties. (Hunter, Hofmann and Espejo, 2018). DRP is usually based on micro CT scans images that are segmented for the extraction of information but can also be based on grain size distribution data.

DRP is applied to estimate the physical properties of rocks by using numerical simulation methods based on high-resolution images of core plugs. In opposition, routine core analysis or special core analysis is done through laboratory tests on plugs. DRP is a suitable method in

rapid assessment of rock properties, but it lacks the precision in evaluating fluid properties. It can be tried to be used as a standalone method for very homogeneous rocks. However, it proves to be especially useful in enhancing special core analysis data. It is regarded in the industry as a necessary complement of lab experiments (Liu, Jin and Wang, 2018). Given the short time of analysis and the quality of the data obtained, it can be stated that this method has the potential to improve overall reservoir characterization in terms of physical parameters.

There are three classes of data that can be obtained from DRP.

- First-class is single-phase flow like porosity and permeability.
- The second class is represented by multiphase properties between fluids like primary drainage capillary pressure and saturation.
- The third class is represented by rock-fluid and fluid-fluid interactions like relative permeability and imbibition capillary pressure.

The first two classes of digital rock results are influenced by the digital representation of the pore network, but for the third additional information are required. Another critical point is the fact that it is hard to simulate fluid-fluid and rock-fluid interaction interfacial tension, wettability and contact angle. (Berg, Lopez and Berland, 2017). In the current study, all three classes will be tried to obtain.

DRP process in general consists of obtaining high-resolution X-ray image slices of the plug and therefore, segment the image, reconstruct, and create a digital model of it. By numerical simulation, the digital rock model is evaluated in terms of rock properties and physical processes. (Glover, 2016). In the case of DRP on CT scans, problems that might arise are linked with the fact that the probes on which the X-ray analysis is made are small. Therefore, it is hard to upscale the obtained results with high accuracy. Other ways also proved were based on grain size distribution extracted either from sieve analysis (Bryant and Blunt, 1992) or 2D thin sections (Bakke and Øren, 1997). Both can represent the pore model with accuracy. The only problem with this is that the 2D thin sections miss the third dimension. Therefore, the approximation through grain sizes obtained from 2D images can become tricky and needs special stereological tools (Iowa, 2020).

A simple workflow in DRP is described in Figure 2.4. Starting with rock characterization which can be done either through 2D thin sections, CT scans, FIB-SEM sections, XRD and sieve analysis grain or pore space information can be determined. Following this, a 3D model is constructed using a different combination or only one data from the above mentioned. When the 3D digital rock model is obtained, additional properties can be extracted.
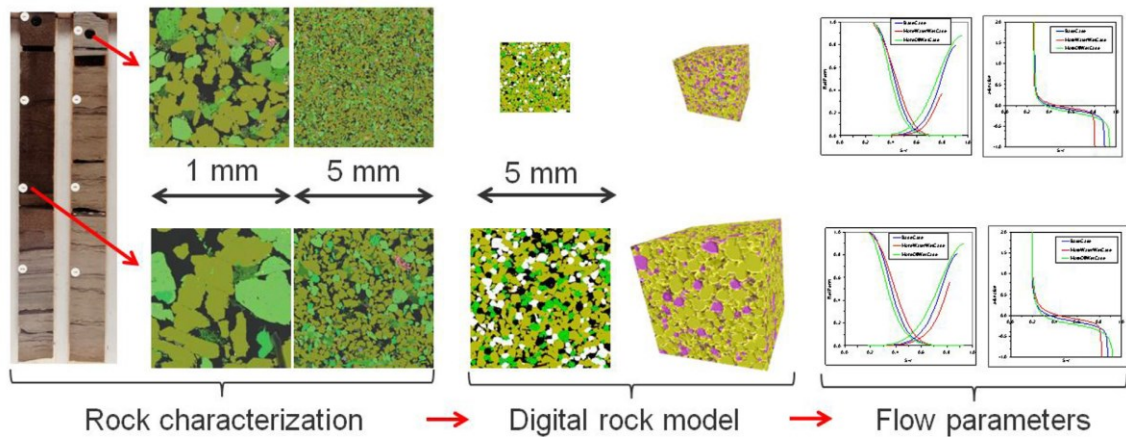
Figure 2.4 Flow chart of the workflow for generating the flow parameters (Berg, Lopez and Berland, 2017)

Another thing that a researcher has to keep in mind when performing DRP is the resolution. Resolution is limited to voxel sizes in the range of micrometres, and even in the current study, it causes problems in assessing the capillary pressure in the higher NWP saturation ranges. Depending on the chosen resolution for a good result and an optimal computational time, some of this data can be missed.

The most significant and most crucial advantage of DRP is that it can perform experiments that are difficult to do without a real-world apparatus in a relatively small-time frame. What's more, the boundary conditions in the simulator can be set whenever an experiment needs to be repeated, without the concern that the rock probe might be deemed unusable as in the case of MICP test in real life (Handoyo *et al.*, 2017). The computational power has also increased in the last years at a much lower price and therefore simulating higher resolution rocks is starting to become more and more feasible (Rassenfoss, 2011). The benefit of using a different discretization is that more points are available, for example, in evaluating the capillary pressure curve. An instance can be seen from Hilpert where the resolution is changed in evaluating a rock model based on a sandstone (Figure 2.5) without difference in the shape of the curve. Only benefit from using a smaller or bigger structure is related to the number of data points obtained.
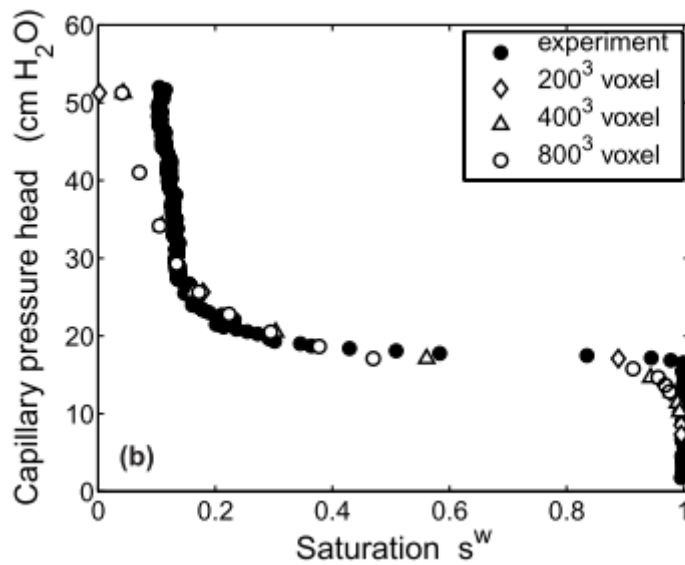
Figure 2.5 Influence of spatial resolution on primary drainage curves for a modelled sandstone
(Hilpert and Miller, 2001)

Although DRP presents advantages, especially in terms of fast evaluation, it still has some flaws. Some of the disadvantages that DRP has besides the need to define the wettability is that choosing the representative elementary volume (REV) might interfere with properties determination. REV is defined as the smallest required sample size that can describe accurately the same lithology (Goldfarb, Ikeda and Tisato, 2018). The REV is also hard to choose it, and on which property depending on resolution, henceforth error can appear in evaluating the data correctly. The power to compute the 3D models is tremendous, and this might require more costs. Also, as scientists want improved models, some trade-offs must be made if a better geometry with a smaller domain is desired or higher domain with compromised geometry. Therefore, the time to compute a better geometry will take longer. As stated before, in the upcoming years, this will be overcome and will become easier to run high-resolution models.

2.3.1 Rock models generation

Most of the DRP studies are run on CT scans or multiple 2D thin sections obtained from microscopy studies. Although this seems to be good ways to recreate the rock, they are expensive, and the image processing poses a significant challenge in the correct assessment of the pore space.

Starting with spheres pack models from Finney (Finney, 1970), scientists tried to recreate rocks inside a computational environment with much higher accuracy. Packs of spheres were used in the early days by Bryant and other authors (Bryant and Blunt, 1992; Bryant, King and Mellor,

1993) in simulating the flow through such generated models for unconsolidated sandstone. The models were based solely on well-sorted sphere quartz grains. Their studies which proved to obtain a working model were later continued by Coelho (Coelho, Thovert and Adler, 1997). In his paper, Coelho also applied a random pack of aspherical particles to see their influence on transport properties. Such a model can be seen in Figure 2.6. Ellipsoidal grains are defined by the semi-axes, taken into account that two dimensions are equal. He has proven that when using ellipses in structures, the permeabilities will differ due to a much more complex flow path.
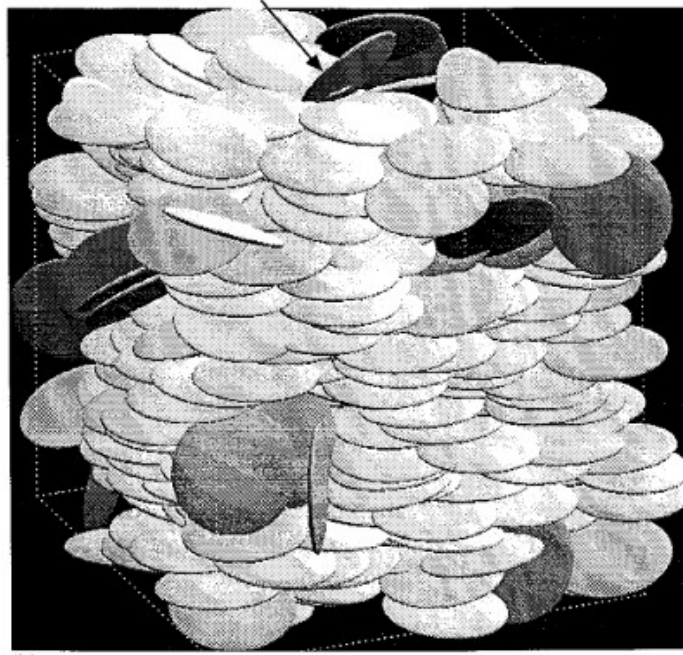
Figure 2.6 Pack of oblate ellipsoids. (Coelho, Thovert and Adler, 1997)

Other studies that focused on 3D recreation based on extracted GSD were made by Bakke and Øren (Bakke and Øren, 1997; Øren, Bakke and Arntzen, 1998; Øren and Bakke, 2002, 2003; Lopez *et al.*, 2010) and later Lehman (Lehmann *et al.*, 2006). These methods are regarded as statistical due to the grains that are extracted from scans and distributed. Although it is easy to obtain dimensions from 3D scans, using 2D sections is cumbersome and requires using stereology principles to interpret it (Iowa, 2020). These principles will not be covered here, as it is not the primary purpose of this thesis.

The models of Bakke and Øren are constructed on a process-based simulation which implies sedimentation, compaction and diagenesis. The process was applied to different rocks from homogeneous like Berea, Bentheimer, Fontainebleau up to unconsolidated heterogeneous rock from the North Sea. The statistical information about the pore structure in rocks is determined by mercury injection data along with GSD from thin section images. The mercury injection tests are used to quality check the results of the experiments. A similar procedure will also be employed in this study. Most of these studies yielded outstanding results for relative

permeability and capillary pressure estimation Figure 2.7. This shows that choosing packs of spheres or ellipses might be an excellent way to describe the pore space.
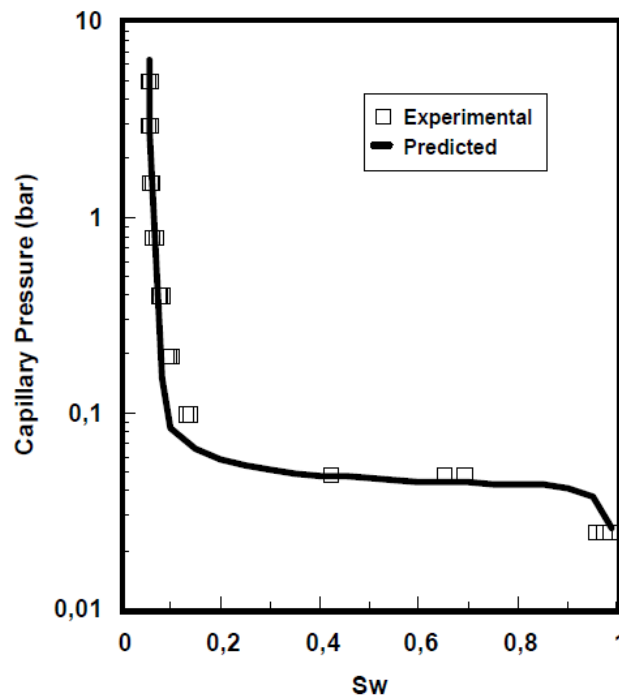
Figure 2.7 Experimental and predicted capillary pressure for the Bentheimer sandstone (Øren, Bakke and Arntzen, 1998)

During this process-based modelling, the sedimentation is starting with the grain size distribution. In this case, all the grains are treated as spherical. They are sedimented based on a low energy sedimentation process. A new sand grain having a radius r settles on the grain bed. The newly deposited grain is reduced to a point, and the radii of the other grains in the grain bed are increased by r. After the new grain is deposited in a stable local position, all the different grain radii are reset to their original values. The radius of each new grains is reduced to 0 before deposition. The radii grains in the grain bed are increased by an amount equal to what radius the former grain had. This makes the new grain to be represented by a point and the grain bed to be described as a solid surface, which geometrically is more comfortable to explain. After the grain centre (point) is deposited in a stable position, all the other grains are reset to the original values. Then the procedure is repeated until the box is filled (Figure 2.8). Some sort of deposition algorithm is also used in GeoDict for sedimentation in a cube. The location in the grain bed of each sand grain depends on how the process takes place either in high or low energy.
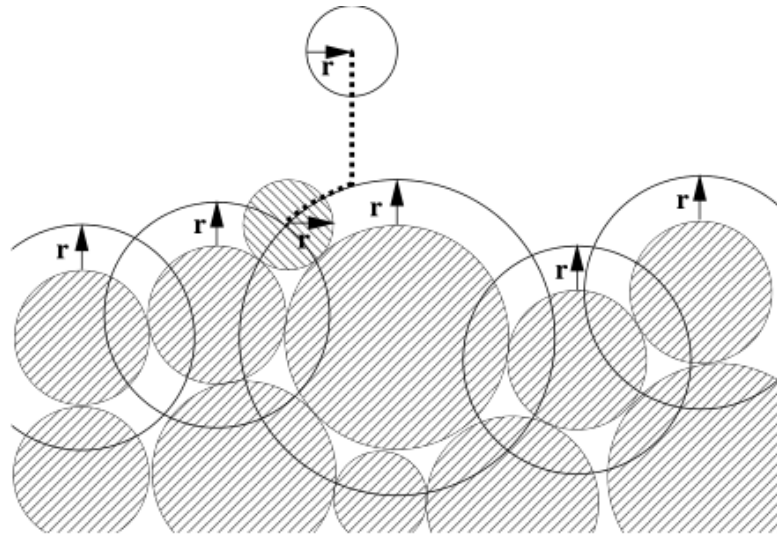
Figure 2.8 Schematic showing the modelling of low energy sedimentation. A new sand grain corresponding to a radius r settles on the grain bed. First, it is reduced to a point while the radius of the grains in the pack decrease. The point is deposited in a local minimum, and all the grain radii are returning to the previous values. (Bakke and Øren, 1997)

The other step important in rock generation is the diagenetic processes. Processes that could be modelled are quartz cement overgrowth and subsequent clay coating on the surface. Quartz growth is simulated by increasing the radius of the grains. Another way, clay precipitation is done just by adding layers randomly. The verification of the model was done in their case by comparing the porosity of the thin section of the plug with 2D sections taken from the newly generated model. Also, the pore space that they obtained can be seen in Figure 2.9. The structure is then approximated to a skeleton and after that by a simple ball and stick representation. This kind of skeleton is called a network model while the other is regarded as a direct model (Figure 2.10).
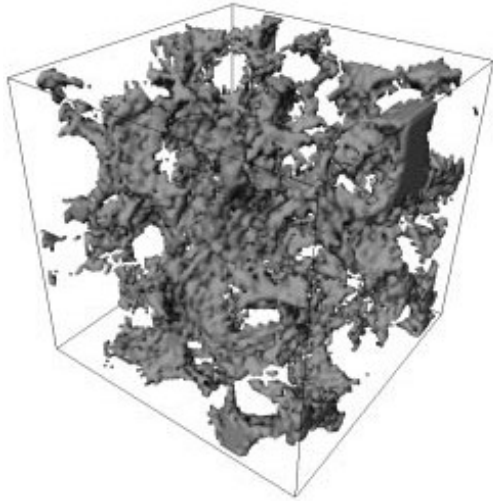
Figure 2.9 Iso-surface of the pore space of the 3D model created (Bakke and Øren, 1997)
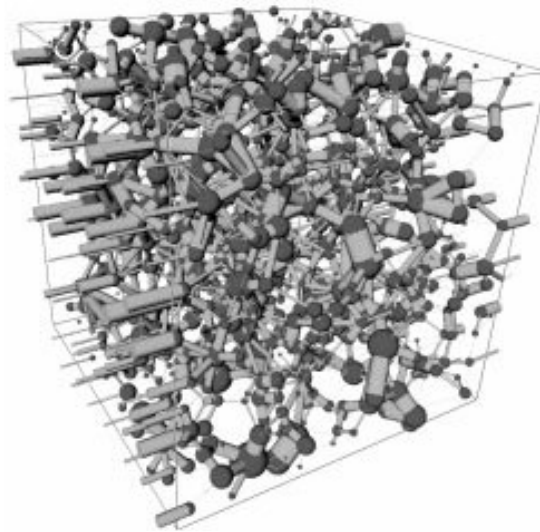
Figure 2.10 Schematic of the same pore space represented by ball and stick (Bakke and Øren, 1997)

In a newer paper, Lehman (Lehmann *et al.*, 2006) also treated the topic of voxel size in these types of simulations. To better represent the pore medium, a voxel size of 10-20 % from the mean particle radius was used. The voxel size has a direct effect on the transport processes and also on the capability to simulate more or less from the pore space. For example, the pore space needs to be corrected due to the chosen resolution. The porosity is modified for the rock model to represent reality. This unresolved space is better seen in the capillary pressure curve (Figure 2.11). Such a procedure will also be carried out for this ongoing study.
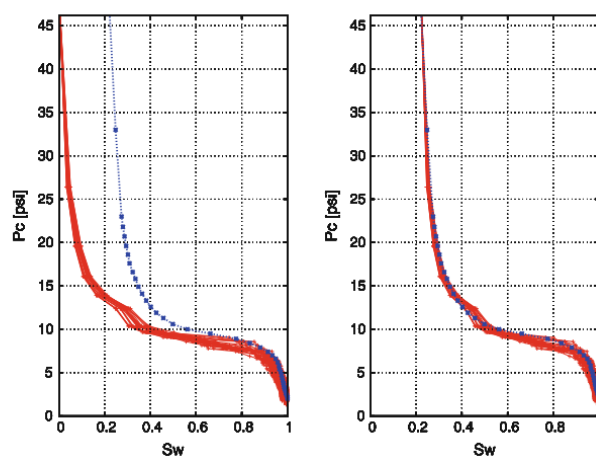
Figure 2.11 The computed (solid line) and measured (dotted) drainage capillary pressure curves for a Berea sandstone sample. The markers on the curves mark the data points. The left-hand-side plot shows computed curves with no adjustments of parameters, whereas the right-hand-side plot shows calculated curves rescaled due to unresolved pore space (Silin et al., 2011)

2.3.2 Rock Properties Simulations

Once the model generation is obtained from images, scans or statistical grain size data, the next part of the digital rock physics technique is represented by the flow simulation. Blunt describes in his paper (Blunt *et al.*, 2013) that there are two main categories in the modelling of the flow, especially the absolute and relative permeability. One is direct modelling, and the other one is network modelling. Network modelling started with the work of Fatt in the '50s (Fatt, 1956) when he characterized the pore space and pore bodies as a stick and balls representation. Then later, other authors start using Lattice Boltzman simulations on rock models obtained either through the reconstruction of CT scans (Bosl and Nur, 1998) or grain size distribution (Bryant and Blunt, 1992).

Although all of this looks promising, flow modelling, either direct or through networks is hard to simulate. Fluid-fluid and rock-fluid interaction interfacial tension, wettability and contact angle are difficult to determine. Another problem is to relate the fluid-rock properties to reservoir properties. Typically, this is solved by ageing rock samples in crude oil from a relevant oil reservoir. While scanning electron microscopy (SEM) can help with that and measure the contact angles, it is still cumbersome to represent the transport properties (Berg, Lopez and Berland, 2017).

Direct modelling implies the creation of rocks based on images. Images can be obtained through CT scans or by 2D thin sections. The difficulty in the design of rocks from 2D thin sections is caused by the problem to appreciate the 3D dimensions of the pore space. It is more computational demanding compared with the pore network model and limitation occur on what is happening below the voxel size. Contrasted to network modelling where a network of balls and sticks is extracted from the rock this method uses the principle of voxels and direct calculation of the flow based on Darcy's law (2.4), Navier Stokes equation and conservation of mass ((2.4)(2.5)). The green term, which is the inertial term, can be disregarded as the flow is considered to take place in a viscous force dominant environment. Direct modelling is suitable for high-velocity flows. Differently, when modelling endpoint saturation where capillary dominated forces are present, the pore network modelling is more useful. A graphical comparison between these two methods can be seen in Figure 2.9 and Figure 2.10, where one rock is modelled in these two ways.

In the present study, direct modelling will be employed for the final permeability evaluation. Also, the relative permeabilities are calculated using the same technique. Though instead, of relying on the Lattice-Boltzmann methods as before (Bosl and Nur, 1998; Ramstad *et al.*, 2012), the Navier Stokes equations will be calculated directly using LIR (Left Identity Right)

algorithm developed by Sven Linden, which is much faster. More information about the method it is computing the flow equations can be found in his papers (Linden, Wiegmann and Hagen, 2015; Goral *et al.*, 2020) as this will not be detailed in this thesis.
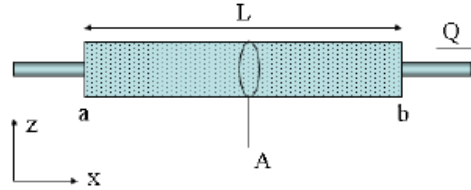
Figure 2.12 Darcy Law description (Hilden, Linden and Planas, 2020)

$$Q = \frac{-kA}{\mu} \cdot \frac{(P_b - P_a)}{L} \qquad (2.3)$$

$$-\mu\Delta\vec{u} + (\rho\vec{u} \cdot \nabla)\vec{u} + \nabla p = \vec{f} \qquad (2.4)$$

$$\nabla\vec{u} = 0 \qquad (2.5)$$

For the calculation of capillary pressure and saturations inside the rocks, a sort of network model is employed called pore-morphology. Pore morphology method even though it is taking place on the model directly is calculated using geometrical techniques. Taking the advantages of fast simulations using inscribed spheres to simulate flow (Silin and Patzek, 2006) the morphological characters can be represented, compared to the usual pore network modelling. Developed by Hilpert in the early 2000's it using as an input the grain size distribution and the porosity as a stopping criterion (Hilpert and Miller, 2001). By modelling the rock and then running simulations using purely geometrical methods, the drainage and imbibition can be simulated. This kind of simulation is regarded as quasi-static (Hazlett, 1995) and is a one-phase flow for each of the two process drainage and imbibition. The geometrical methods of erosion, dilation and opening are employed for the calculation of saturations inside the pore space directly on the rock model. The capillary pressure of fluids is calculated purely mathematical based on Young Laplace equation (2.1) and is approximated as spheres. If a sphere with a certain radius is entering through the pore space, then that is the pressure associated with the fluid to flow. The simulation though is a bit more complicated and implies at first for the drainage case the occupation of the whole pore space with the NWP. Where the NWP is disconnected from the boundary communicating with the NWP, then that is the residual

saturation remained. All of this is possible by dilatating or eroding the area around the grains with a certain voxel number. The process can be seen in Figure 2.13.

The results obtained through such methods in evaluating the transport properties looked promising and was later employed inside the GeoDict software package. Shape and entry pressure of the capillary are well matched on homogeneous rocks (Hilpert and Miller, 2001), and therefore, it can be used to evaluate the pore space properly.
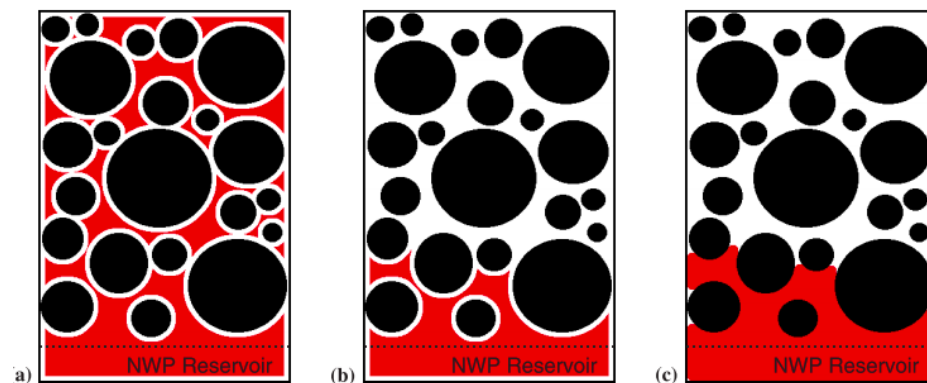
Figure 2.13 2D simulation of drainage in and pore space. The lower part is NWP connected, after the dilatation of the grains with NWP the separated phases are removed and after the erosion of the area around the grain with the same number of voxels the residual saturation of the NWP can be obtained, by approximating the NWP phase with spheres. (Hilpert and Miller, 2001)

Although it can simulate the drainage case properly, Berg (Berg *et al.*, 2016) discovered that the morphological approach does not represent the imbibition process. To calculate relative permeability in imbibition, a model that simulated both capillary and viscous forces is required. As a quasi-static process, it is less computationally demanding at the expense that only the connected pathway flow is captured. Therefore, ganglion dynamics are not taken into account, and residual saturation from imbibition remains high. The motion of the disconnected fluid phase causes ganglion dynamics. Unfortunately, in a quasi-static displacement, the disconnected fluid phase is treated as unmovable. A mass exchange exists between the connected and disconnected fluid phases hence influencing the pore-scale fluid distribution, including the configuration of the connected phases. Dynamic models capture viscous capillary displacement in a much more efficient way, but they are more complex to use.

In terms of contact angle and wettability, they only account in the end as a post-processing step in the Young-Laplace formula. As this a purely geometrical technique, it does not account during the simulation for wettability, but rather at the end in the calculus. Hence, no exact flow simulation with varying wettability can be performed.

Chapter 3

Input data & Methodology

3.1 Input data

The data set that was used in this study came from Romania and is represented by unconsolidated sandstones. Although many probes were available, they do not have all the required information that could help in the process of generating the 3D rock models and also to validate the porous medium properties of these rocks. Some pictures of the probes can be seen in Figure 3.1. The probes are friable, and therefore just bits of information for each could be obtained. 27 samples from 11 wells represented the data. The core material was stored unsealed, and material is poorly consolidated and fragile. The 27 probes are defined as follows by 6 core samples, 17 core chips and 4 fined grained sandstones also in the form of core chips.

Figure 3.1 Sandstones probes (labelled as code B16390 – right and B16407 – left). Both are unconsolidated sandstones

The 6 plug samples were cut, trimmed, and cleaned by Soxhlet Toluene and Methanol Drying oven at 60°C. One out of 6 plugs does not have information about permeability. Information

about porosity is available for all the others. Thin sections were available for one probe (B16407) along with scanning electron microscopy (SEM) images and information about X-ray diffractometry (XRD). Flooding experiments to determine S_{or} and relative permeabilities were performed. Unfortunately, no grain size distribution (GSD) data was available.

The 17 core chips were also cut, trimmed, and cleaned by Soxhlet Toluene and Methanol Drying oven at 60°C. Basic properties like porosity and bulk volume were calculated. Eight probes had XRD data and thin sections. Only two samples from 17 had information about the GSD from sieve analysis.

Fine-grained sandstones represented the last 4 core chips. Porosity and permeability were determined by using crushed rock analysis. Again, no information about grain size distribution was available.

Out of all 27 probes, 21 of them had mercury injection capillary pressure (MICP) tests. That was important as it offers information about the pore throat size distribution inside a rock. The data available is presented in short in Appendix A. The things not presented are the XRD-data, the thin sections, the SEM pictures, and the macro CT scans, which were not used for this study.

In the end, only one probe qualified for the creation of 3D rock models. It had both the GSD and the MICP data to validate the reconstructed model inside GeoDict. The selected sample was **B16390**. In Figure 3.2, the distribution of grain size based on sieve analysis is presented. The porosity measured by MICP was 40.4%, and the one measured through the Helium method was 42%.
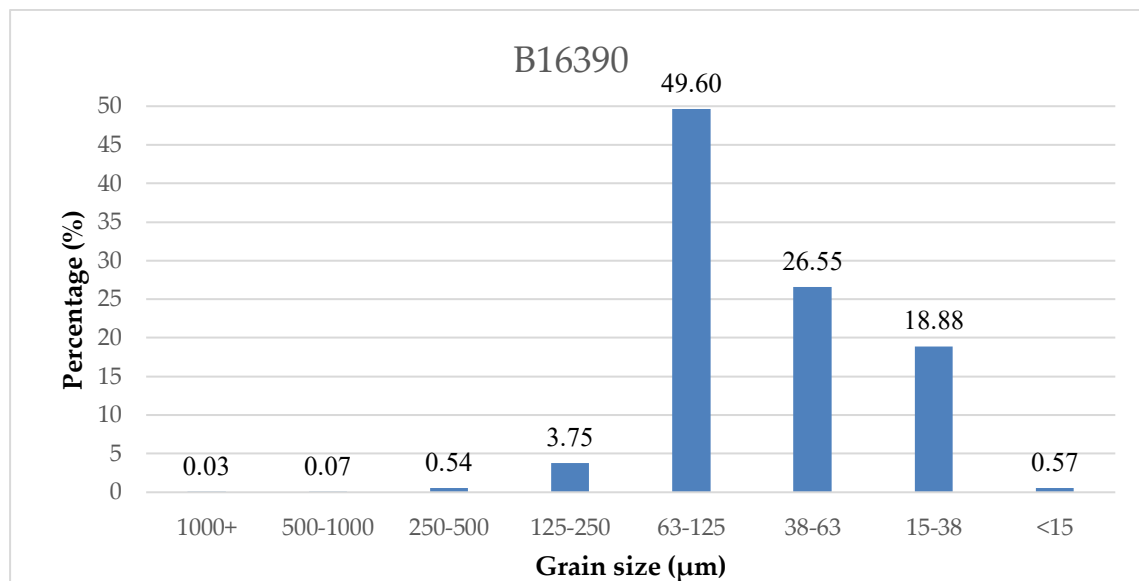
Figure 3.2 Grain size distribution of the analyzed probe.

The results were compared with the capillary pressure curve (drainage) from the MICP experiments (Figure 3.3). The MICP was performed beforehand, and the data from the experiment was available. The values of pressure from the laboratory (60000 psi) are enormous in comparison with what can be simulated in a 3D computational environment (100 psi). Moreover, in real life, most experiments are stopped at 5 bars (72 psi) as capillary pressure experience inside the reservoir is assumed to be below these values (Berg, Lopez and Berland, 2017). Likewise, the pore throat distribution (Figure 3.4) was calculated, and it will be used during the recreation of the rock in the simulator for the matching of the model.

Pressure vs Saturation
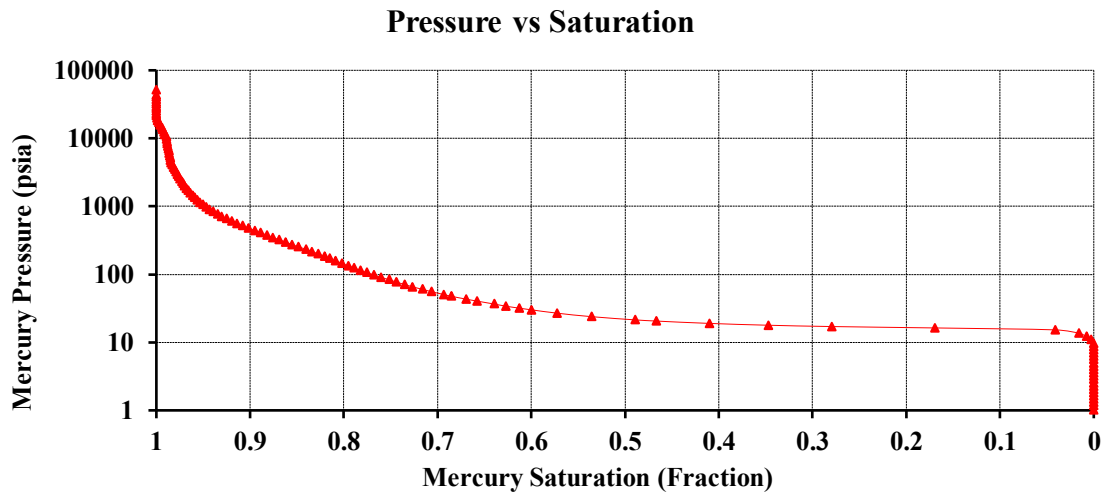
Figure 3.3 MICP drainage experiment for probe B16390

d Sw / d Log Pore Throat Size vs Pore Throat Size
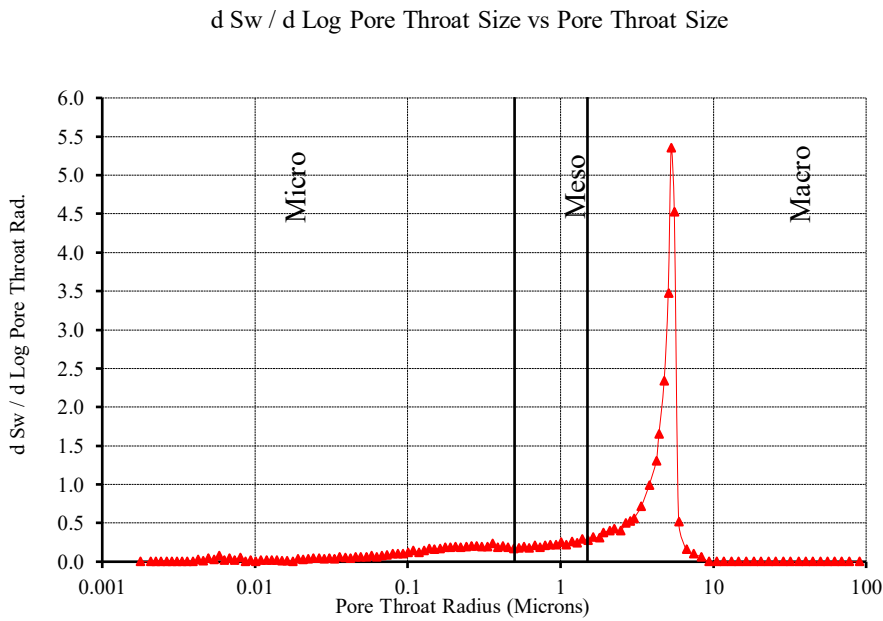
Figure 3.4 Pore size distribution for probe B16390

3.2   Creating Digital Rock Models

As stated in the beginning, the purpose of this thesis is to design a workflow in creating rock models that mimic the pore space based on only grain size distribution. The creation of the 3D Rock Models was done using the GeoDict software. The reason for choosing a software-based application is established on the idea that it is easier to use and much faster to apply in an industry environment. Moreover, software capabilities are tested to see what the software limitations are in the reconstruction domain of 3D rocks. The steps of creating the rocks are presented in here along with the simulations performed. For the creation of rocks and simulation of the flow through the porous media, three packages from GeoDict were used (GrainGeo, FlowDict and SatuDict).

GrainGeo is used to create 3D models of granular structures for different types of materials, by compaction, packing or pilling objects of different shapes. It can replicate with a high-fidelity material like ceramics, particle filters for cars, polymer concrete, electrode materials for batteries and finally granular structures like rocks.

For the modelling of the rocks, the input can be grain size distribution, pore size distribution or grain shapes. The simulation is creating the structures by randomly distributing grains, by pilling them or by packing the spherical grains. The distribution is controlled by the structure size, the density, the porosity, or the grain shape. After the structure is created, compaction or growing sediments processes can be run. (Fingerle, Rief and Planas, 2020)

The majority of the models were created by a random generation which was based on the grain size distribution (Finney, 1970; Bryant and Blunt, 1992; Bryant, King and Mellor, 1993; Hilpert and Miller, 2001; Guodong, Patzek and Silin, 2004) and having the porosity set as a stopping criterion (Hilpert and Miller, 2001). For this, the "Create grains" option was used together with macros written in Phyton for bulk simulations. For the other model which tried to mimic the process-based modelling (Bakke and Øren, 1997; Øren, Bakke and Arntzen, 1998; Øren and Bakke, 2002, 2003) the „Pile Grains" method was used in which grains were falling and settled down by a local minimum. „Sinter and Crystallization" method was therefore implemented to simulate the geological sedimentation and particle growth. A description of the methodologies is presented in this chapter.

3.2.1 Random generation of grain packs

Using the function "Create Grains", a rock in a given domain with a predefined selected resolution is created. The domain is represented in *Figure 3.5*. A voxel (blue cube) is representing the resolution of the model. In this study case based on the discoveries that the number of voxels is not trivial beside generating more or fewer data points, it was chosen to go with a cube of 800*800*800 μm^3 (Hilpert and Miller, 2001) for faster time simulation. Taking into account also that for a good pore space representation, the voxel size should be less than 15% of the mean grain size (~75μm), the minimum voxel length is chosen way less for a better representation (2 μm) (Lehmann *et al.*, 2006). For this choice, the maximum sphere of grain or pore space that GrainGeo can simulate is equal to sqrt (3)*voxel length $\approx$ 4μm due to the limitation of the software.

Geometrical configuration:

- Nx = 400 voxels
- Ny = 400 voxels
- Nz = 400 voxels
- Voxel length = 2 μm
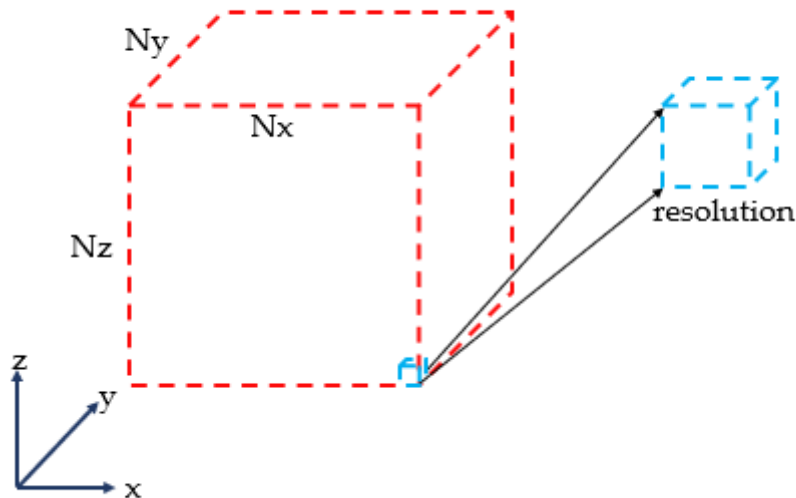
Figure 3.5 Simulation domain for the rock generations

Inside this generated cube, the grains are generated in the model at one time without simulating a natural sedimentation process, but more mimicking the packing of spheres or other shapes (Finney, 1970; Bryant and Blunt, 1992; Bryant, King and Mellor, 1993). The grains distribution inside the model is made uniformly meaning that the centre values are uniformly distributed across the structure. A parameter like density or porosity stops the creation process. In this case, the stopping criterion was chosen to be the porosity of the rock, as it was known. The same procedure by using porosity as a stopping criterion for the generation of models was used by

Hilpert (Hilpert and Miller, 2001). Most of the random packings that were created based on this method had the grain size distribution extracted from 2D pictures or CT scans. For these cases, the simulations were based solely on data from sieve analysis. The sieve analysis was split in bins to see how the variation in grain diameters affects the results, and how to reach faster to match the pore space properties.

For probe **B16390**, a few simulations were run with the natural rock porosity of 40%. Then after plotting the MICP results, it was observed that the maximum pressure that could be obtained was around 100 psi. The MICP was calculated using the SatuDict module (Widera, Linden and Planas, 2020), which employs the pore morphology method to determine the distribution of the two phases inside a porous media. The technique was described in the Literature Review Chapter, and it is based on solving a purely geometrical problem by using the Young Laplace formula (2.1) and maximal inscribed spheres technique (Hazlett, 1995; Hilpert and Miller, 2001; Silin and Patzek, 2006). This proved that the software, together with the model, generated has some limitations. These limitations are presented below and have to be considered from the beginning of the simulation in future works.

1. The first limitation was linked with the unresolved pore space. Comparing the resulted pressure from the simulator and calculations (≈100 psi) with the pressure obtained by the real MICP pressure (≈60000 psi) it was clear that the model was not representing the same pore space of the real rock. Young-Laplace formula was used to calculate the maximum pressure that the 3D rock model can have (2.1). Here σ (interfacial tension) is equal to 0.48 N/m, and the θ (contact angle) is equal to 140°.

   Resolution is considered here to be a limiting factor, and therefore, the whole pore space cannot be accessed in higher ranges on non-wetting saturations. Based on the results from the simulation, the capillary pressure curve does not cover out of the entire pore space. Figure 3.6 describes how much of the pore volume is inaccessible for the example of the rock **B16390**. Based on the calculation, a <u>106 psi</u> can be maximum reached by the capillary pressure. After plotting the newly translated capillary pressure that resulted in the simulation, around 23% of the pore space from the rock is not accessible. Therefore 77% out of 40% porosity that the probe has, is accessible in the simulation. That will represent a porosity of 30.8% in the simulation model for the rock **B16390**.

   Such a correction was also used by others before as it hard to match the same pore space as the real rock with a smaller model (Silin *et al.*, 2011). Therefore, it should be stated that this needs to be done for further probes, also at the beginning of the simulations to be sure that the models are genuinely validating the experimental data.

Pressure vs Saturation
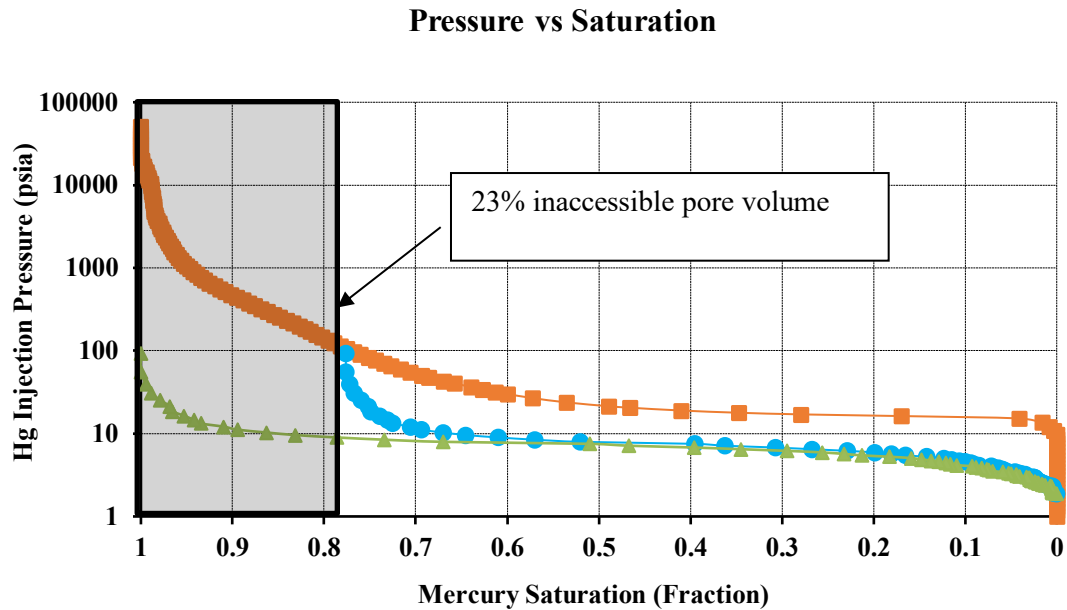
Figure 3.6 Orange line – MICP experimental data; Gray line – Simulated case based on original GSD (spheres) with 2 μm resolution and 800*800*800 μm³ dimensions; Blue line – Same case with the recomputed saturation

2. The second limitation noticed was linked with the number of bins selected. When the simulations are run with a high number of probabilities and intervals, the numerical methods tend to reduce the number of intervals and merge probabilities. That was noticed to happen in cases where the sieve intervals were split into 6 or 7 bins. The example can be seen in the figure below. For the case with a bin of 6 the input data could not be replicated inside the computational environment in a manageable way. Especially at boundaries of the sieve sizes, the percentages are moved or merged, and other values of the grain size distribution are obtained. This does create a higher difference between the simulations, and it is good to keep in mind that a high variation in data might cause different results.
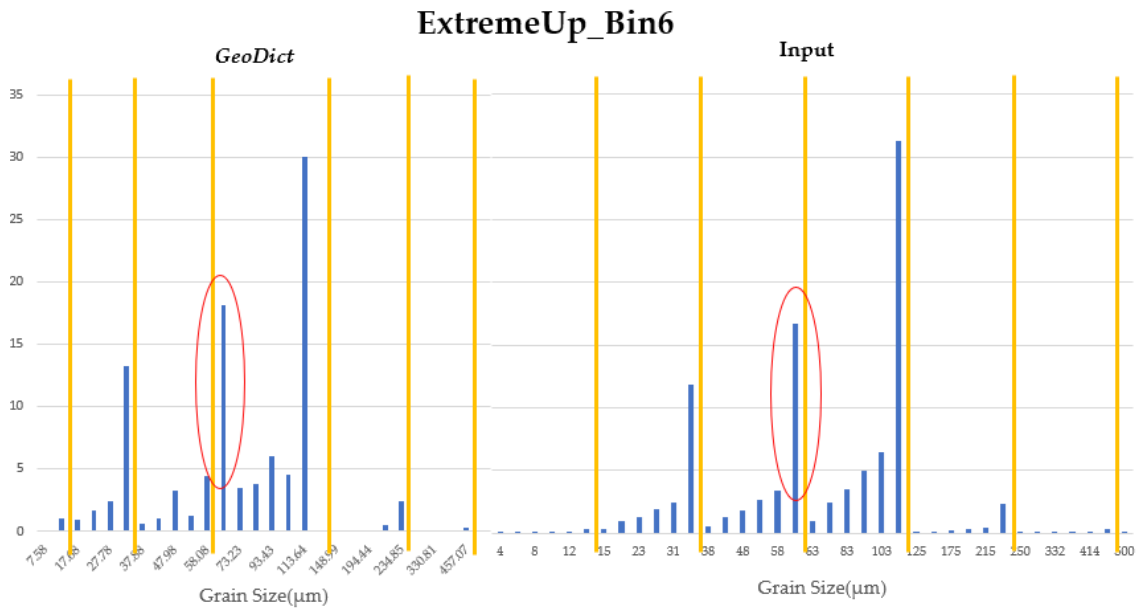
Figure 3.7 Differences between the input data and what GeoDict used for the simulation

3. The third limitation that was noticed was linked to the maximum sphere dimension generation that could be done inside the model. Because the initial grain size distribution is until 1000 μm and the model is only 800 μm on every direction, generating a grain with a diameter of 1000 μm will result in filling of the pore space completely. Therefore based on the lowest probability of such grain in the real rock to occur (0.03%) and on the model limitations, it was decided to calculate how big the diameter can be to replicate the rock model better. Based on the computed grain volume, it resulted that a maximum diameter of 250 μm can be used (*Figure 3.8*). One grain of 250 μm diameter is representing 2.2% out of the grain volume. The grains over 250 μm represents around 1%. Therefore, it is much closer to the reality to assume this as the maximum diameter, compared with a diameter of 1000 μm which results in a single grain volume of $65.4*10^6$ μm^3. Hence, the volume of this grain in my model will represent 18% out of total grain space, which will be untrue compared with 0.10% in reality. Fortunately, GeoDict can create only parts of such a grain at the box boundaries and therefore manages to fit the volumes if the variation is not huge. If the variation in the number of probabilities is high, then most probably it will not replicate the grain size distribution (Figure 3.7) and errors might appear.

V_t=358.4*10^6 μm^3

$V_s = 0.022 * V_t$

V_s=8.181*10^6 μm^3
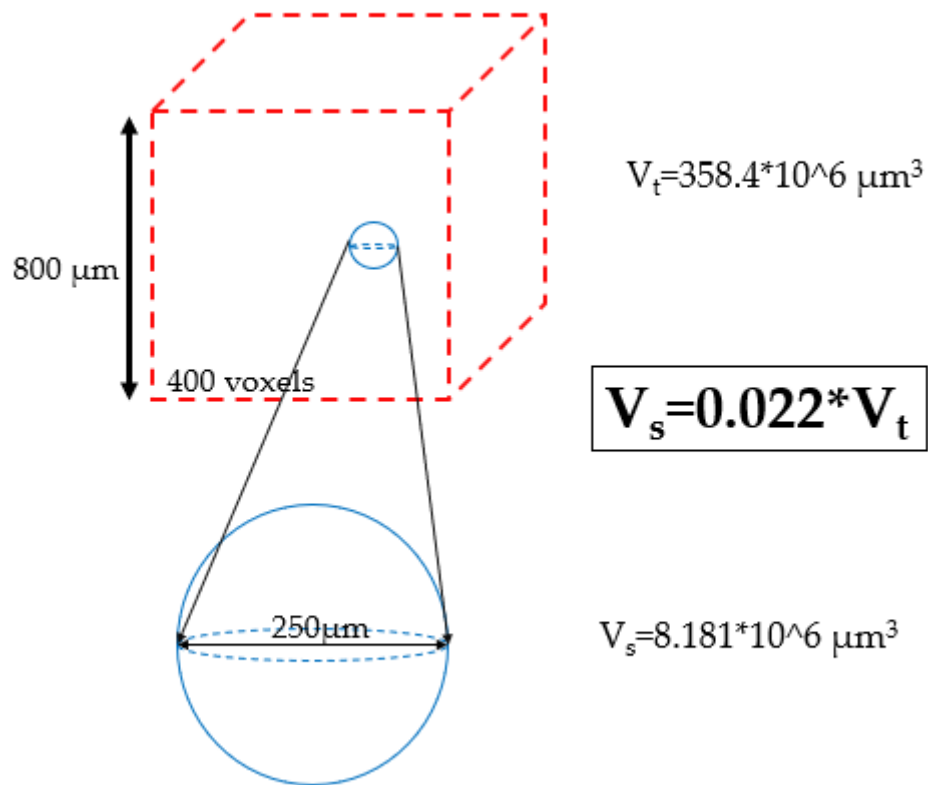
Figure 3.8 The maximum sphere dimension that can be accounted for in the model is 250 μm based on a grain volume of 358.4*10^6 μm³. The volume of a sphere of 250 μm represents 2.2% out of the entire volume.

Once these limitations were settled, grains were generated in the model based on the given grain size distribution. After the grain generations occurred, remove overlap procedure was employed. Here is crucial as the simulation is for unconsolidated sandstones. Hence no overlap can be present. This method was also encountered in the paper of Lehmann (Lehmann *et al.*, 2006). Shifting, deforming, and rotating processes of grains along with a before and after image can be seen in *Figure 3.9*.
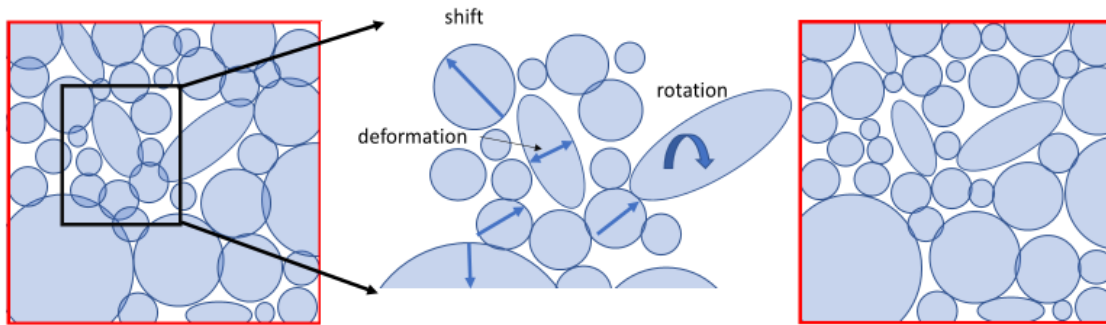
Figure 3.9 Left: Grains are generated randomly in space, based on the input sizes from the sieve analysis; Centre: Grains are rotated and moved until the desired overlap is reached. Right: The rock model is achieved with a minimum of overlap (<0.9%)

Regarding the types of grains, the software can handle from spheres, ellipses to complex polyhedron or fibres. In this case, the approximation of real grains consisted of spheres or ellipses. Moreover, the type of material can be specified. However, as the simulations were only trying to predict the transport properties in porous media using an exact representation of the pore space, it was of little value to use mineralogy (Bryant and Blunt, 1992). The process of validating the pore space characteristics was achieved by getting closer to the capillary pressure curve by only varying the shapes and sizes of the grains, and therefore specifying the type of material would not have helped in the chosen approach. For the diameter of the spheres and ellipses, the grain size distribution was used in different variations. For the spheres, the grain creation is simple as to each diameter a probability corresponds already to the grain-sized distribution. For the ellipses build, the dimensions of the minor axis (Diameter 2 and Diameter 3) are considered equal, and the major axis varies (Coelho, Thovert and Adler, 1997). As the data set presented before only deals with grain size distributions without specifying the type of grains, it could be assumed that the Diameter 1 is all the time higher than the other two by a ratio equal or higher to the golden ratio (1.6180) (Huntley, 1974). The sketch of the simulation models for sphere and ellipses taken from GeoDict can be seen in Figure 3.12.
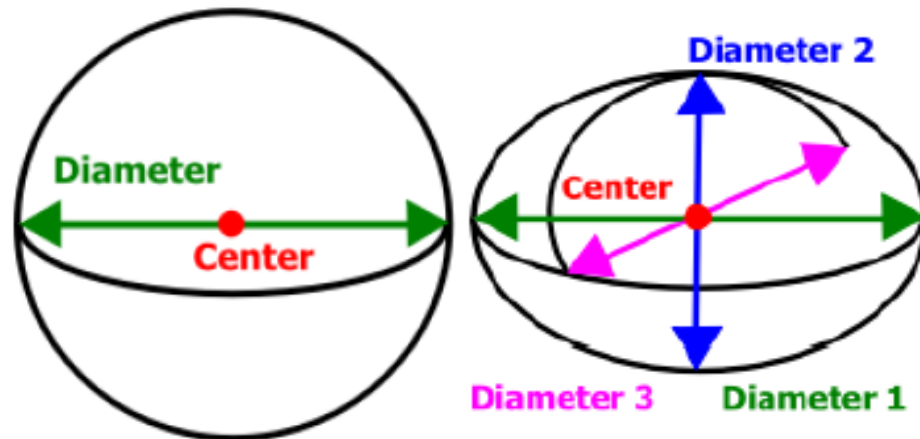
Figure 3.10 Diagram of the simulated grains. (Fingerle, Rief and Planas, 2020)

The present study used a pattern in analyzing the data. First, it started with sphere simulations, as from the literature, this shows a good match (Finney, 1970; Bryant and Blunt, 1992; Bryant, King and Mellor, 1993). Then ellipses were added in specific amounts with varying the major and minor axis dimensions, to see how close to the real MICP curve it can get. The variation in the minor and major axis was considered as probably during sieving analysis some elongated grains might or might not pass by the smallest diameter.

3.2.1.1 Generating random models with spheres

Starting from the original grain size distribution, it was varied the number of bins in each sieve interval and treat all of them as spheres. That was done by splitting each interval into different bins and distribute the values in different ways, like normal, parabolic or upper or lower for a specific interval. A descriptive legend of what each distribution means and the names associated can be found in Appendix B. For the Base Case simulation, original grain size distribution was used without the last intervals as previously mentioned in the limitations. A detailed description of how the data from sieving analysis was distributed for the rock **B16390** can be seen in Appendix C.

The workflow employed was based on starting first to simulate models with spheres, where the diameters from the sieve analysis were split in bins from 2 to 7. Each sieve interval from Figure 3.12 was divided into a smaller interval of 2,3,4,5,6&7 values. The schematic of the way the simulations were performed can be seen in Figure 3.11. The vertical axis shows the simulations done for each interval for the sphere cases. On the y-axis, the other cases are presented, like sphere and ellipses and/without anisotropy included. All topics will be discussed in the Results

chapter in detail. A short description is given below on the way the distribution of values looks like for the case when each sieve interval is split into 5 values by 7 different modes.
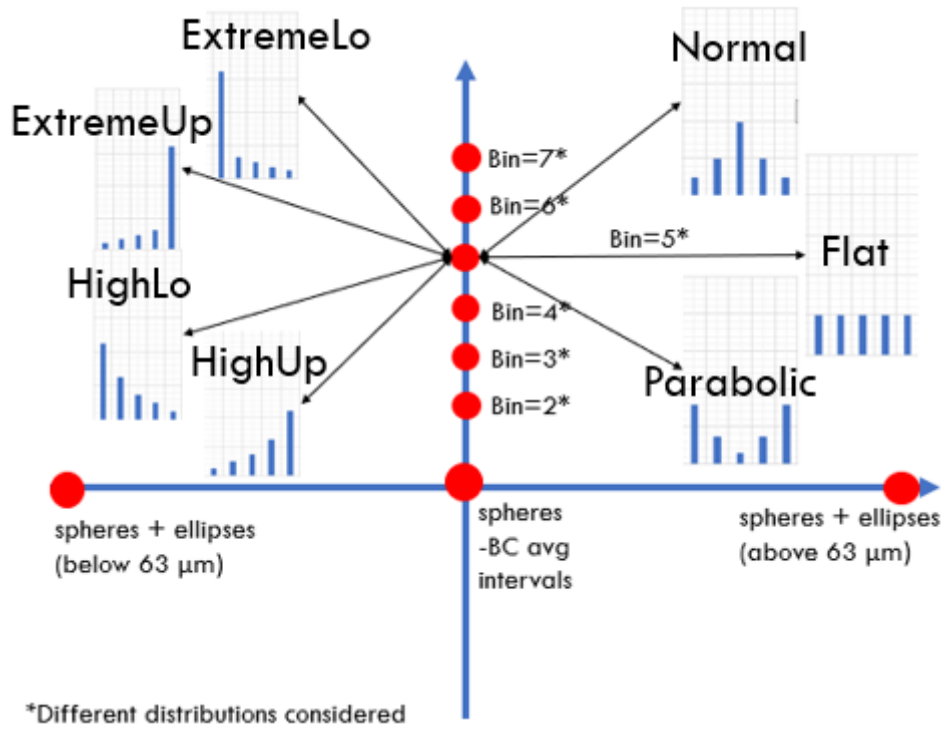
Figure 3.11 Schematic of how each distribution was realized and the further steps in the simulation

Original
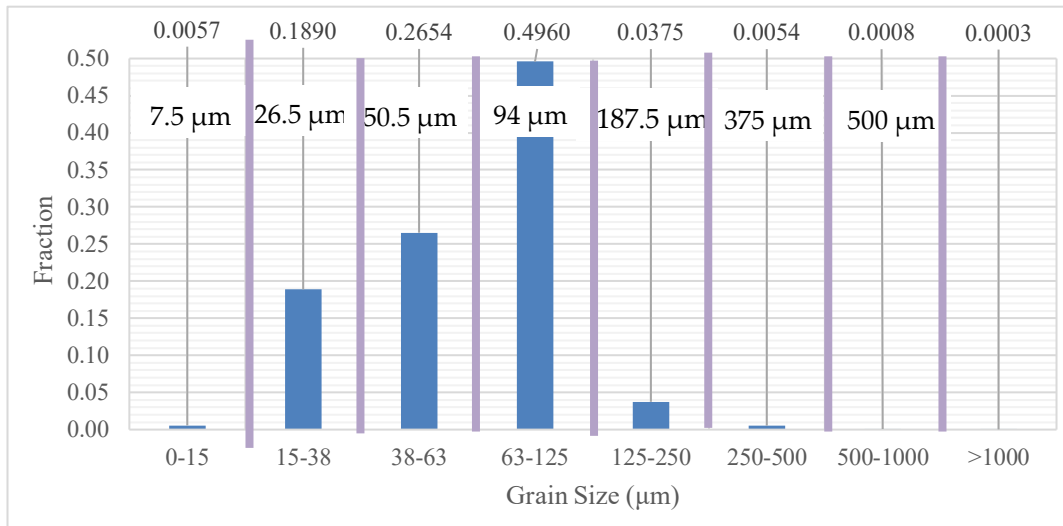
After distributing
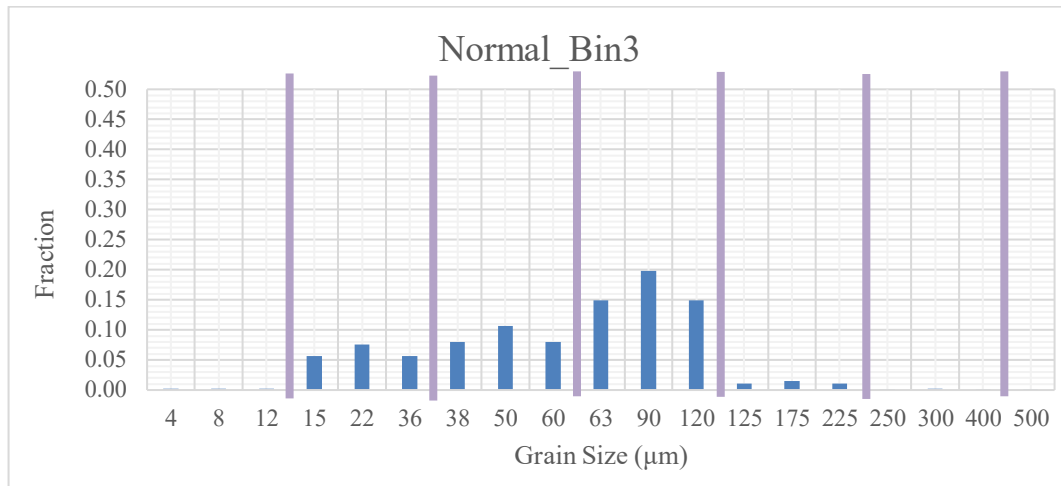
Figure 3.12 Up – Original grain size distribution for the probe B16390 The average values above were used as an input for the simulation of the first case (Base Case). Down – Redistributed grain size for a bin of 3 using a normal distribution.

After these simulations of the capillary pressure curve were analyzed, it was decided to perform this split in bins of the sieve analysis just to a certain extent, not until the maximum assumed dimension. As it is going to be seen in the results, only some cases were performing better in each bin simulation, as more variations got into less satisfactory results. Therefore, the decision made was to split these better performing cases only below a specific interval. The cases were as follow:

- Type A: grains were only distributed in bins below 38 μm (19.47% of total grains). Over 38 μm the lowest values were considered as grain sizes with the full percentage attributed to it for the entire interval. (Figure 3.13)

- Type B: grains were only distributed in bins below 63 μm (46.01% of total grains). Over 63 μm the lowest values were considered as grain sizes with the full percentage attributed to it for the entire interval. (Figure 3.14)

- Type C: grains were only distributed in bins below 125 μm (95.61% of total grains). Over 125 μm the lowest values were considered as grain sizes with the full percentage attributed to it for the entire interval. (Figure 3.15)
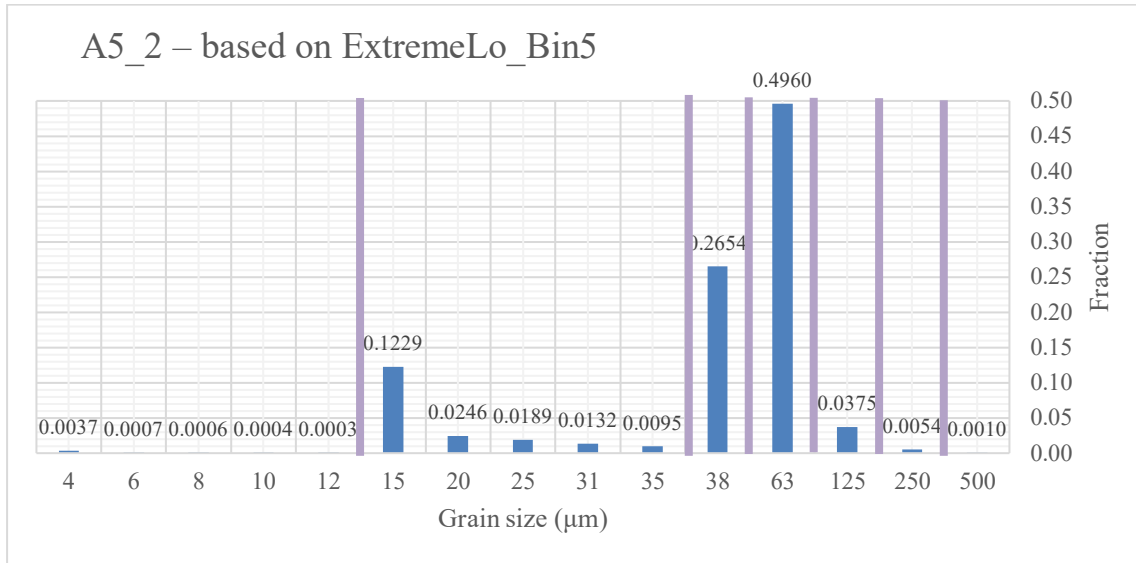
Figure 3.13 Case with a bin of 5 distributed for the sieve intervals below 38 µm
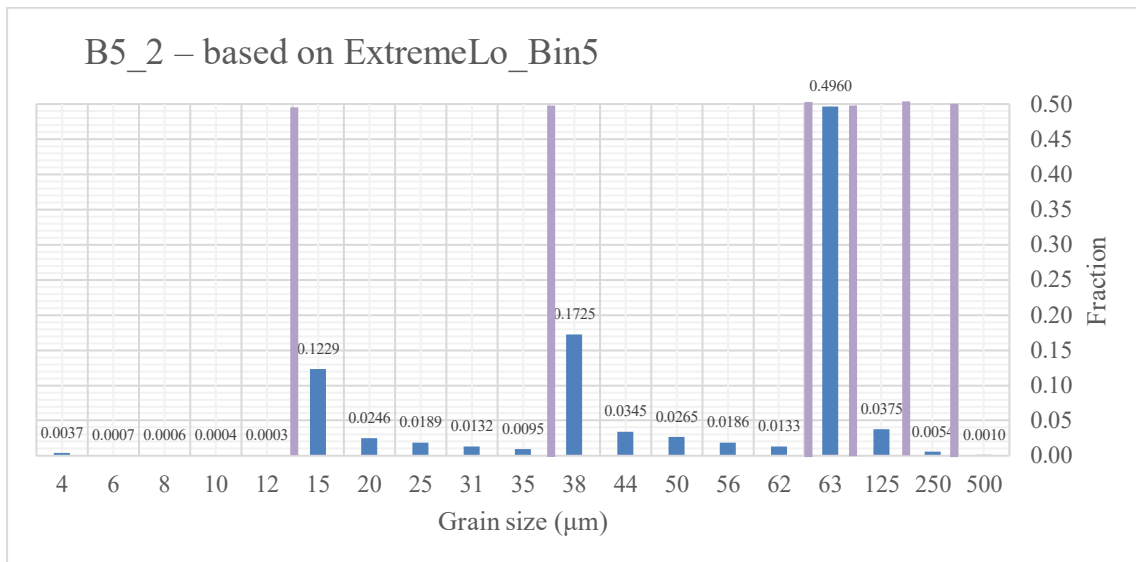
Figure 3.14 Case with a bin of 5 distributed for the sieve intervals below 63 µm
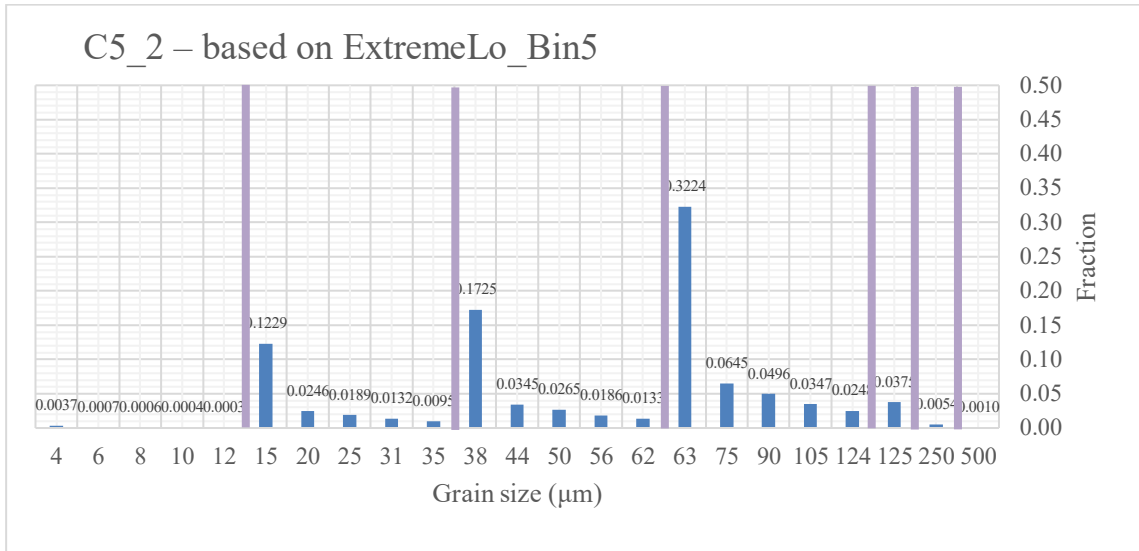
Figure 3.15 Case with a bin of 5 distributed for the sieve intervals below 125 μm

More examples can be seen in Appendix B & C, along with the legend explaining each simulation name. Also, each case in A, B, C, was based on best performing cases from the first simulation. For a detailed description, please visit Appendix B, where the model names are explained.

Other tests that were performed on the newly created models were to see how the absolute permeability looks like, and how it varies in models. The comparison could not be made with the experimental data, as the probe did not have a proper permeability value.

3.2.1.2 Generating random models with spheres and ellipses

Another set of simulations considered for the sensitivity analysis and in matching the capillary pressure curve has consisted of spheres and ellipses. Some of the previous models of distribution from spheres that yielded great results were taken and also used with ellipses. The variation was done both in the lower and upper part of the sieve sizes just to test how it will change and to have a better understanding of the parameters change.

The simulations were run on the 2 cases from spheres (B5_2 based on ExtremeLo_Bin5 with values varied only below 63 μm/C5_2 based on ExtremeLo_Bin5 with values varied only below 125 μm), that showed a match with the capillary pressure curve from the sphere cases.

The naming is described as follows:

- B5_2_I – based on the same rule of variation as B5_2, only 4.39% were ellipses between 125 and 250 μm

- B5_2_II - based on the same rule of variation as B5_2, only <u>20.92%</u> were ellipses between 63 and 250 μm

- B5_2_III - based on the same rule of variation as B5_2, only <u>37.46%</u> were ellipses between 63 and 250 μm

- B5_2_IV - based on the same rule of variation as B5_2, only <u>53.99%</u> were ellipses between 63 and 250 μm

- B5_2_V/C5_2_V – based on the same rule of variation as B5_2/C5_2, only <u>26.54%</u> were ellipses between 38 and 63 μm

- B5_2_VI/C5_2_VI – based on the same rule of variation as B5_2/C5_2, only <u>18.90%</u> were ellipses between 15 and 35 μm

For the last two cases, other cases were run where the minor and major axis values were inversed. This was explicitly performed to test the instances when, for some reason, not all of the elongated grains are falling through the sieve. For sensitivity analysis, it was decided to do 2 cases for the last simulations just to see how it varies if minor and significant axis are swapped. The cases naming and description are below

- B5_2_VIII/C5_2_VIII – based on the same rule of variation as B5_2/C5_2, only <u>26.54%</u> were ellipses between 38 and 63 μm – minor axis of ellipse becomes major

- B5_2_IX/C5_2_IX – based on the same rule of variation as B5_2/C5_2, only <u>18.90%</u> were ellipses between 15 and 35 μm - minor axis of ellipse becomes major

For a better understanding of the input data, Appendix D can be checked to see how the distributions look.

One particularity of these models with ellipses is that now isotropy can be accounted for. When spheres alone are used, orientation does not play a key role due to the symmetrical shape of the spheres. Although, if ellipses are introduced, one should specify the direction of the grains. All objects generate in the granular structure have either isotropic or anisotropic orientation. A clear description of the anisotropic or isotropic behaviour can be seen in Figure 3.16. To orient, the grains, the orientation tensor matrix needs to be modified. Orientation tensors are symmetric second-order tensors and are calculated as the dyadic product of the d_k from all n fibres divided by n, where d_k (*(3.1)*) is the unit vector describing the direction of the kth grains and n the number of grains. In multilinear algebra, dyad means taking two vectors and multiplying them. The result is a second-order tensor, which carries two associated direction and magnitude. It is used as it contains physical or geometric information. A dyadic is referred to as a sum of dyads. (Mitiguy, 2009)

$$d_k = \begin{pmatrix} x_k \\ y_k \\ z_k \end{pmatrix} \qquad (3.1)$$

The orientation tensor T is dyadic and is calculated with the following formula:

$$T = \frac{1}{n}\left(\sum_{k=1}^{n} d_k d_k^T\right) = \frac{1}{n}\sum_{k=1}^{n}\begin{pmatrix} x_k x_k & x_k y_k & x_k z_k \\ y_k x_k & y_k y_k & y_k z_k \\ z_k x_k & z_k y_k & z_k z_k \end{pmatrix} = \begin{pmatrix} t_{11} & t_{12} & t_{13} \\ t_{21} & t_{22} & t_{23} \\ t_{31} & t_{32} & t_{33} \end{pmatrix} \qquad (3.2)$$

The elements on the diagonal define the orientation strength for the X, Y and Z directions. Their sum is up to 1. For example, if t_{11} is equal to 1, that means that all grains are oriented in the X direction (Figure 3.16, centre image). In the same manner, it will be if t_{33} is equal to 1, all the grains will be oriented in the Y direction. If the values are similar for all three directions, then the result will be a uniform distribution for the grain orientation. (Figure 3.16, right image).
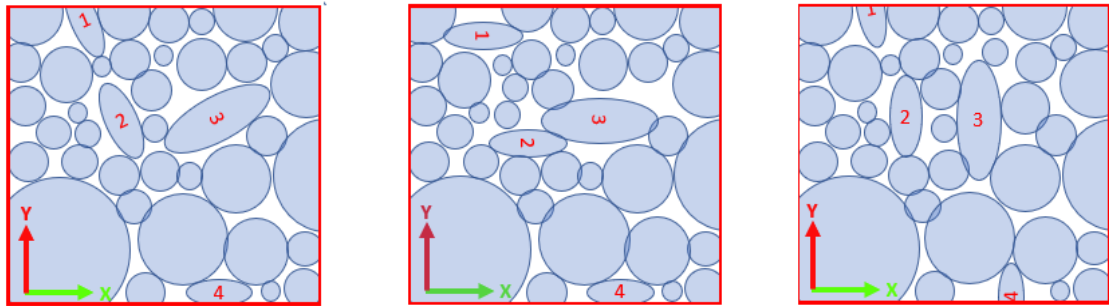
Figure 3.16 Left: All elongated grains(ellipses) are oriented in equal percentages in all 3 directions; Centre: Grains are oriented anisotropically only in the X direction; Right: Grains are oriented anisotropically only in the Y direction.

Six simulations with changing orientation tensor were run on one of the cases (B5_2_III), to see the influence of the anisotropy on the capillary drainage curve and permeability. The values can be seen in Table 1.

Table 1 Values chosen for the orientation tensor

	Case 1	Case 2	Case 3	Case 4	Case 5	Case 6
t_{11}	0.7	0.1	0.1	1	0	0
t_{22}	0.2	0.7	0.2	0	1	0
t_{33}	0.1	0.2	0.7	0	0	1

3.2.2 Geological processes rock creation

Based on the process-based modelling, a model was created using a similar method in GeoDict. The "Pile Grains" module mimics the sedimentation process, as it was a technique used before by other authors (Bakke and Øren, 1997; Øren, Bakke and Arntzen, 1998; Øren and Bakke, 2002, 2003). The grains are deposited one by one in an environment constructed with the same dimensions as before. The deposition is done without overlap. Each grain is falling in the model without the possibility to be included in another grain. Stopping criteria are the same as the ones presented in "Create Grains" module with the addition of another one called "Fill to Rim" (Figure 3.17). This was set as a stopping criterion for the models as it is one of the best reproductions of a sedimentation process. The grains were created as before based only on an input grain size distribution, with simulating spheres and ellipses.
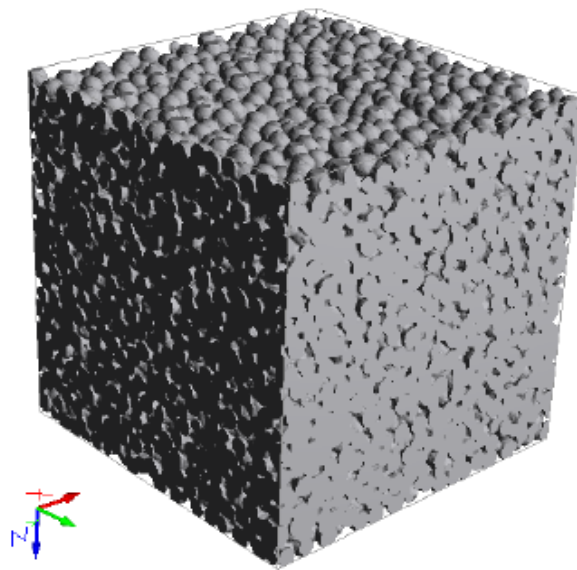
Figure 3.17 Fill to rim model with spheres (Fingerle, Rief and Planas, 2020)

Simply, the process is based on dropping object after object in the inflow plane. The grains are chosen to be deposited in one direction like X, Y or Z and the deposition is done by finding a stable minimum, where each object is checked to have a stable state, a process seen in other paper before (Bakke and Øren, 1997). If the results are unsatisfactory, then several shifts and rotations can take place. A higher shift value will rotate the grains further and mimic a high

energy depositional environment while a smaller shift value will reproduce the opposite (Figure 3.18).
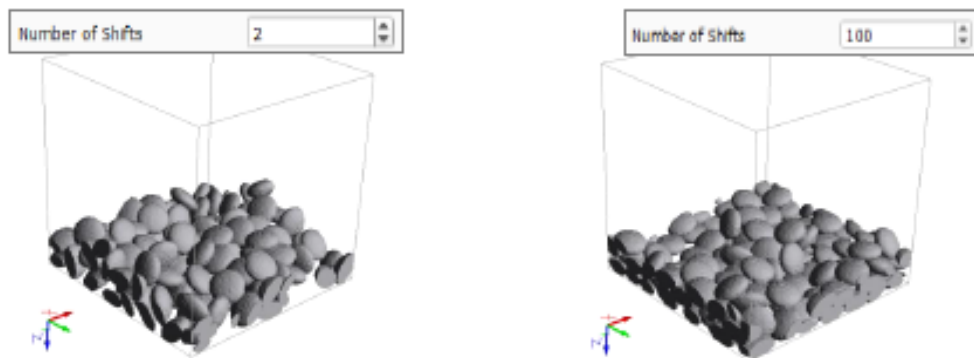
Figure 3.18 Right: Effect of a low number of shifts; Left: High number of shifts

As the porosity is hard to match by filling the boxes with grains, the "Sinter and Crystallization" module is applied. During this process, a created rock can be compressed or inflated until the desired parameter is reached. Grains are deformed on their touching points, and an interface material can be generated on their surface.

Using shrinkage option, the percentage by which the structure is compressed or increased in each direction can be defined, while using the solid volume percentage (SVP) the sintering process will continue until the input SVP is exceeded. This way, the desired porosity can be matched. The only problems remain on the faces of the model. As the grains are deposited gravitationally, the upper and lower part might have faces with bigger pore spaces and therefore affect the results of simulated capillary pressure. Only one case was run based on this process as it did not show outstanding results. The case was one with spheres and ellipses with the same distribution as the one in B5_2_III.

Chapter 4

Results and Discussion

The results were analyzed to see how the modelled capillary pressures and pore throat radius distributions fit for the unconsolidated sandstone (**B16390**). First, the results from spheres random packs will be presented. After that, the ones from spheres and ellipses will be shown both from random packs and sedimentation process. A sensitivity analysis in which each parameter influence is demonstrated will summarise the chapter. Finally, the computed relative permeabilities will be shown for some simulations along with the workflow developed on this probe, and which with some optimization can be used on any other unconsolidated sandstone.

4.1   Spheres random packs simulation results

The first sphere simulation was run as presented in the methodology chapter on the original grains size distribution. This represented the Base Case and the start for the sensitivity analysis. Based on that, the variation of bins was performed which resulted in different entry pressures. As this rock is not homogeneous, the use of randomly sphere packings are not reproducing with accuracy the pore space as in the case of Hilpert determinations (Hilpert and Miller, 2001). The results from a simulation with a bin of 3 and 6 can be seen below. The results plotted are only comprising the highest and lowest pressure obtained.
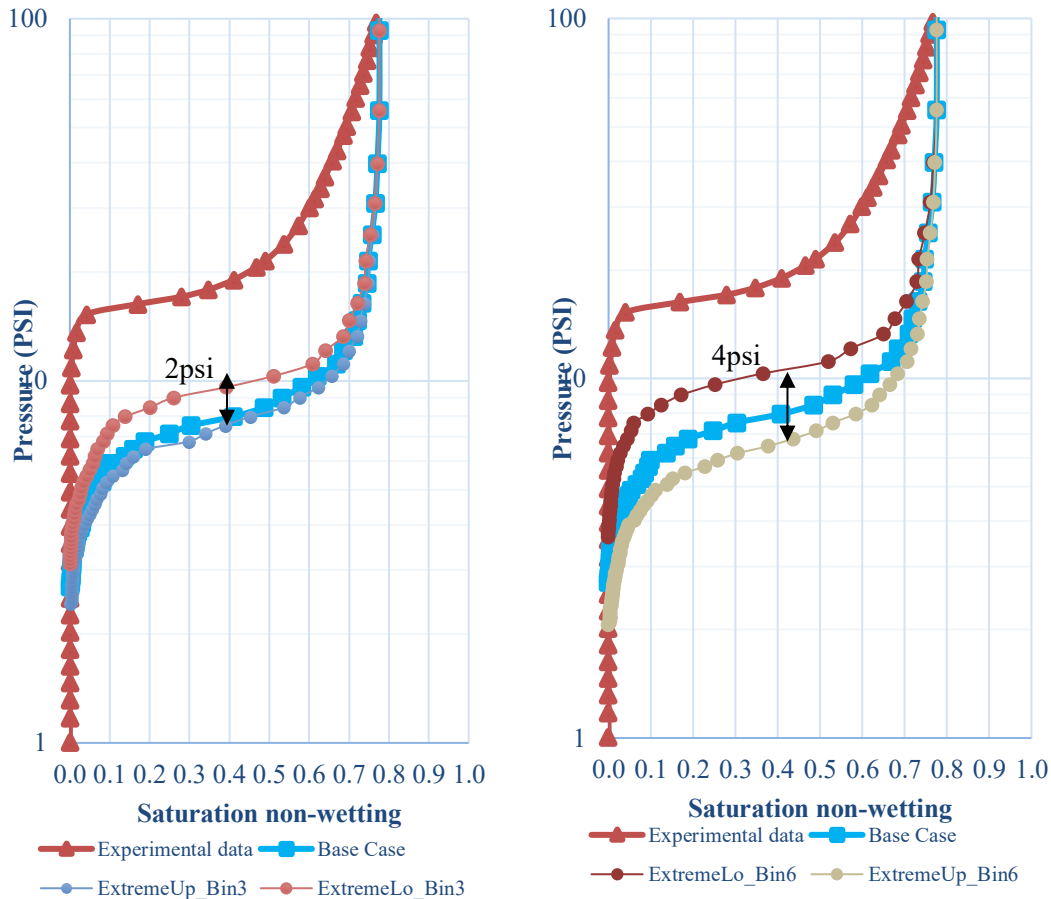
Figure 4.1 Capillary curve simulations for different cases with different bins.Left: Bin=3; Right: Bin=6

From the Figure 4.1, it can be noticed that the cases with a higher percentage distributed to the lower size grains (ExtremeUp) yielded better results than the instances where the higher percentage was distributed to the bigger size grains (ExtremeLo). The rock probe is known to have a poor to moderate sorting. This means that the dimensions of the grains are varying and is more common to have a random distribution than a normal one. Another noticeable effect of varying in bins is that as the bin number is increased the difference between the highest and lowest pressure is increasing from 2 psi to 4 psi in the middle of the curve.

The difference between the capillary pressure curves of best cases simulated at a porosity of 30% and the capillary pressure curve from the experiment is between 8 - 13 psi in the middle of the plateau (S_{Hg}=40%). This is because the entry pressure is low, which in turn results in a lower capillary pressure plateau. In the upper saturation part S_{Hg}, the difference is, even more, around 50-60 psi. The upper saturation part difference is due to the recalculated curve and the resolution of the voxel. As the saturation increases, the smaller pores remained to be filled, and the model does not consider the microporosity, which also plays a role in here.

The entry pressure is much lower than the one in the experimental data for all cases. That means that still, pore throat radius of the model is not matched with the experimental data. Using only spheres, the pore throat radius is higher than in the actual rock. Also, the 3D model is not accounting for the closure correction so the entry pressure will be difficult to match as voids exist at the model faces.

Running sensitivity analysis on the obtained curves further details can be observed (Figure 4.2). The sensitivity is done on the whole P_c curve using the normalized root mean square error (NRMSE) (Equations (4.1)&(4.2)). Moreover, the sensitivity analysis of the P_c curve was split into NWP saturation intervals for each area of interest. The intervals were chosen to be representative for the entry pressure ($S_{NWP} < 0.1$), the plateau of the P_c curve ($0.1 - 0.5$) and higher saturations part where the P_c curve behaves non-linear ($S_{NWP} > 0.5$). In Equation (4.1) n is the number of values, y_i is the ith observation of experimental data and $\hat{y}$ the predicted y value from the simulations. The normalized root mean square error (Equation (4.2)) is therefore obtained by dividing the RMSE to the average of the observed values $\bar{y}$. The results of the cases described in Figure 4.1 can be seen in Figure 4.2.

$$RMSE = \sqrt{\frac{\sum_{i=1}^{n} (y_i - \hat{y})^2}{n}} \qquad (4.1)$$

$$NRMSE = \frac{RMSE}{\bar{y}} \qquad (4.2)$$

As the data is distributed in more significant bins, larger grains appear in the model in a higher percentage. Hence, the results are showing a higher variance between the lower and highest pressure. Sometimes the lower capillary pressure values are even lower than the Base Case simulated on the average dimension from the sieve analysis. Compared with the experimental data all sphere cases are around 0.45 and 0.75 offset. As a close fit will mean an error equal to 0 is fair to say that these models are nowhere near the real situation. Studying the bin cases, it can be seen that the models with a distribution ExtremeLo although performing better have an offset of 0.67 from the experimental data for each of the bin distributions. The worst performing are the cases ExtremeUp where the distribution is done with a higher percentage towards bigger grain size. Cases like the Normal distribution, Parabolic or Flat does not show promising results and therefore were not plotted. This is somehow expected as the rock is poorly sorted.

Comparing each of the zones described earlier, an improvement is seen in the higher-pressure cases from the average case (Base Case). Varying the bin also shows that there is no improvement in obtaining a better fit to the experimental data. Either a bin of 3 or 6 yields more or less same deviation in terms of higher pressure curves. On the plateau interval (0.1 -0.5) the smallest deviation is obtained. Also at the entry pressure, a good improvement is noticed. The

difficulty in matching the zone of entry pressure is linked with the closure correction effects that are not performed. The last portion described by the highest saturation is not showing a great improvement. This can be caused, as stated before, by the fact that my resolution is not good enough and also the microporosity is not considered in my models.
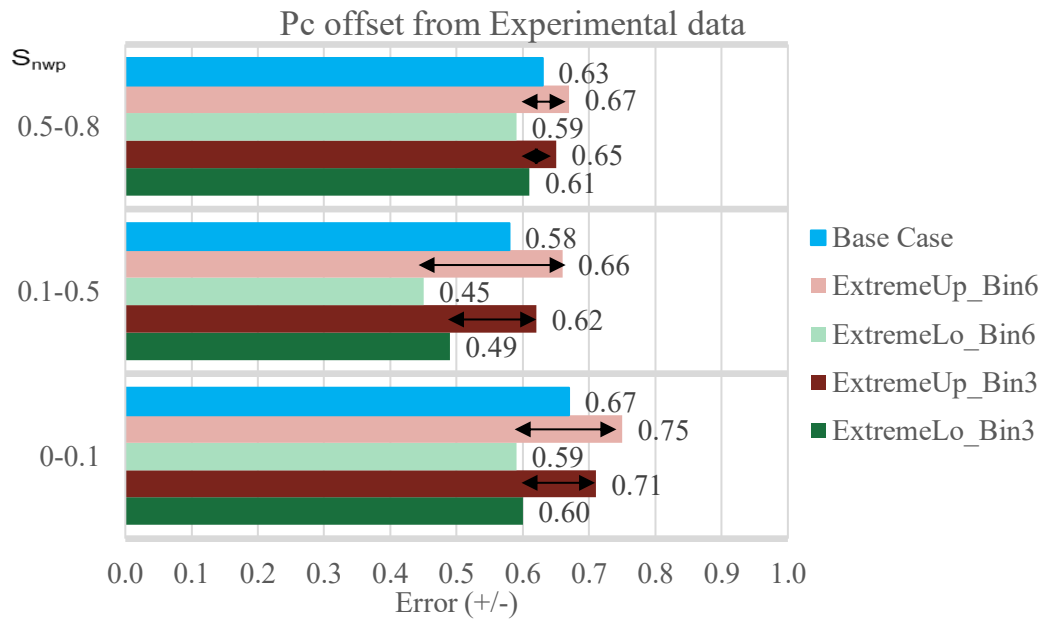
Figure 4.2 Sensitivity analysis for the sphere cases when the bin is varied. The black line represents the Base Case (where the values were averaged, and no bin distribution was considered). The calculation is based on the NRMSE on the whole P_c curve

In Table 2 the summary of the cases with the highest and lowest pressures on each bin are presented. Except for 2 cases with a bin of 5 and 7 all, the other instances respected what was determined before (highest pressure when varying in the lower part, lowest pressure when varying in the higher part of the grain sizes). The results in simulations with a bin of 5 and 7 although different are not uncommon. As the rock is poorly sorted cases where symmetrical distribution is employed can perform worst or the same as when higher percentages are assigned to bigger grain sizes.

Table 2 Cases highest and lowest variation from the experimental data

Highest Pressure	Lowest Pressure
HighLo_Bin2	HighUp_Bin2
ExtremeLo/HighLo_Bin3	ExtremeUp_Bin3
ExtremeLo_Bin4	ExtremeUp_Bin4
ExtremeLo/HighLo_Bin5	Normal_Bin5
ExtremeLo_Bin6	ExtremeUp_Bin6
HighLo_Bin7	Flat_Bin7

As the results looked promising, it was then tried to construct on the cases with the lowest deviation from the experimental data and vary under a certain interval only. The choice of this was built on the premises that most of the grains are already in the lower part of the interval with most of them being below 125 μm (95%). Likewise, below 63μm the percentage is 46.01%, which again represents almost half of all the grains in the rock. As a consequence, faster processing time is achieved. The cases naming and methodology was explained in the previous chapter and can be found in Appendix B.

In Figure 4.3, the deviations of each case can be seen that is becoming lower than before. Comparing with the Base Case is a 14% improvement. Comparing the dimensions of the bin it can be seen that the influence is small and most of the results are based on the way the distributions looks like. However, the distribution of around 4 - 5 bins is promising and introduce enough variation to represent reality. The best results are obtained when the variation occurs below 63 microns, while the least is obtained when varying below 125 microns. Distributing between 63 and 125 microns instead of considering all grains of one dimension creates bigger grains that in exchange will translate into higher pore throat radius inside the model. This will lead to a decrease in capillary pressure. Even so, the difference between these 2 cases B and C is minimal. The advantage of using this method is that is reducing the time to compute the models. The drawback is that a lower distribution will mean a reduced real-life representation of the rock.

After analyzing all the cases from the sensitivity analysis, the one based on the lower P_c offset from experimental data was chosen for the introduction of new shapes. This is based on case ExtremeLo_Bin5, and it will be called B5_2. For comparison in the next simulations also the least performing from the same case was chosen (C5_2).
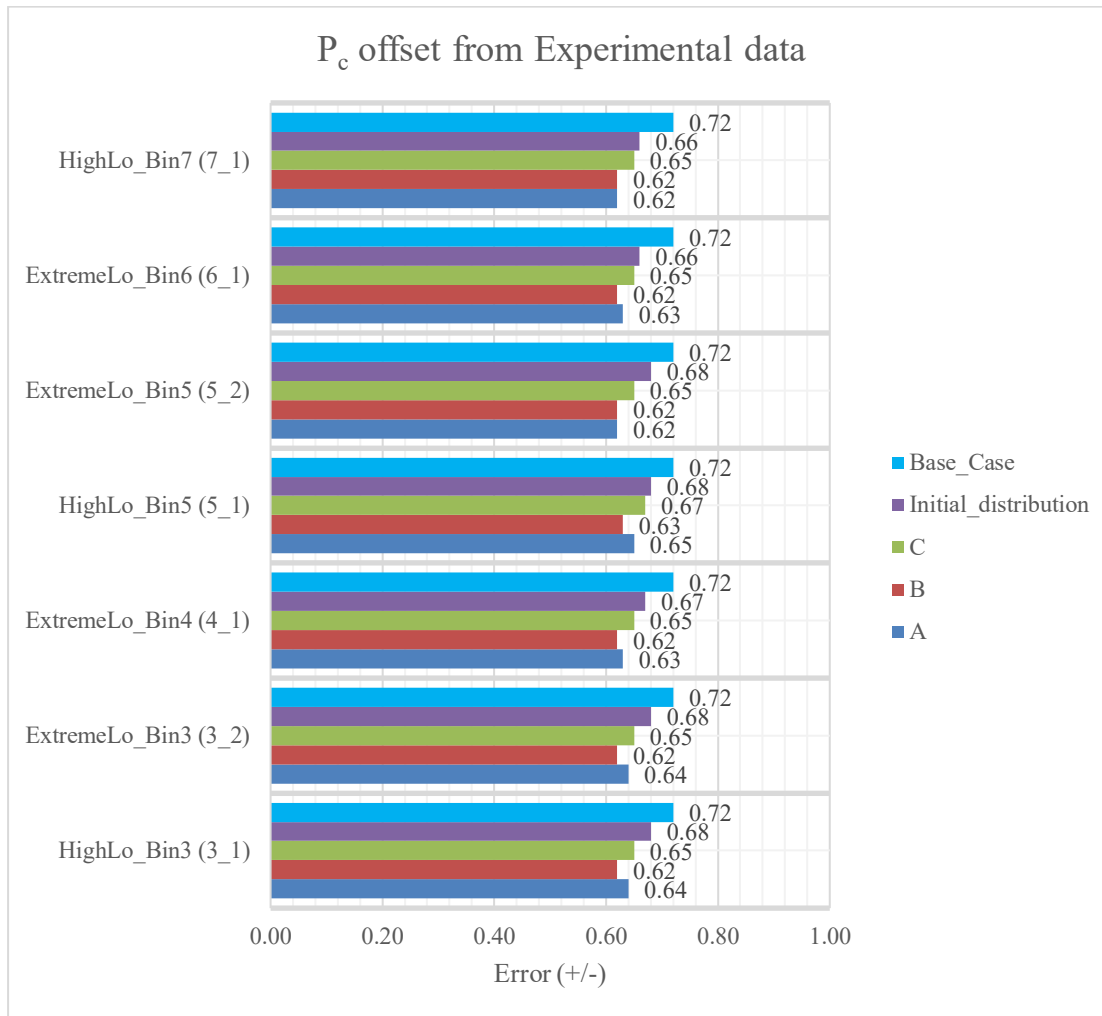
Figure 4.3 Sensitivity analysis sphere cases A, B and C

The differences between some of the examples for the chosen simulation cases are shown in Figure 4.4. Graphically the P_c curves are close, and the sensitivity analysis confirms this behaviour. Still, the models are not heterogeneous enough to fit the experimental data. Compared to the previous model (ExtremeLo_Bin5), an increase of around 3 psi is observed for each of the newly simulated cases. Punctually on this case, the simulation yielded errors of around 0.48 for the entry pressure zone and around 0.58 for the zone with higher saturation of NWP. Compared with the previous simulations (around 0.6 in both) an improvement in the entry pressure is noticed (16%) but with minor effects on the higher saturation ranges (3%). The P_c curve at the plateau is enhanced by a higher factor as the entry pressure, now having an error value of around 0.37. Still, the error is unacceptably high, and more tests have to be performed.
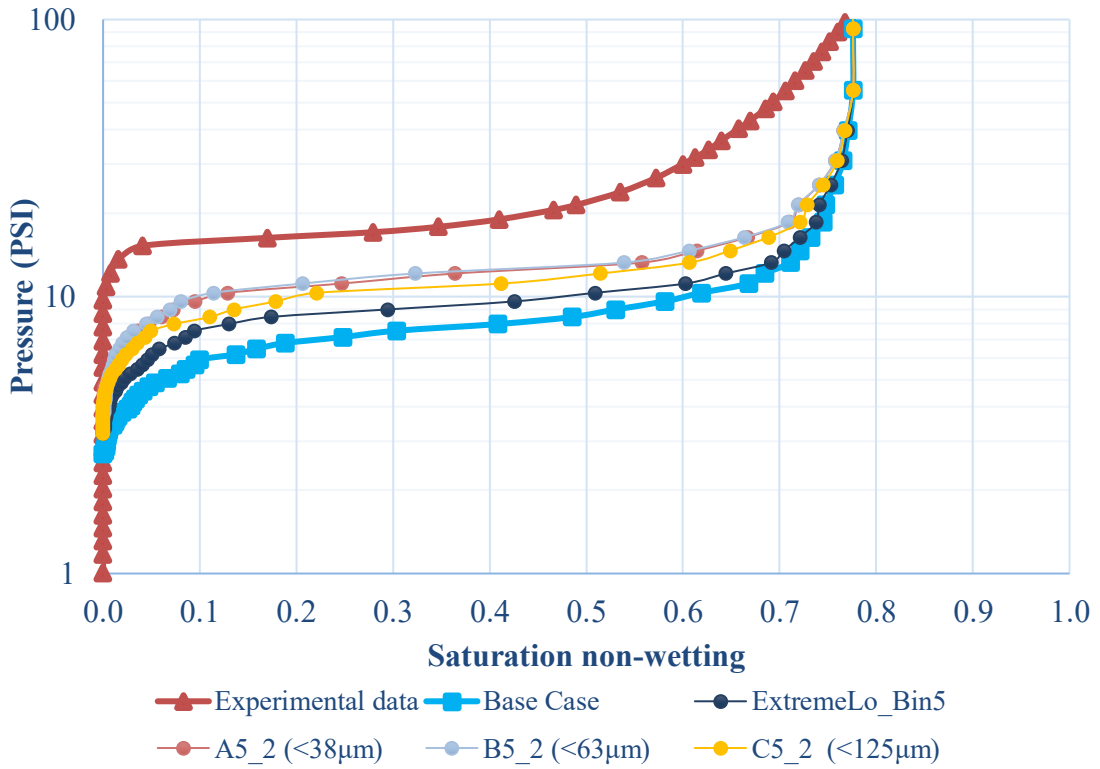
Figure 4.4 Capillary pressure curves for the cases where the distribution in 5 smaller domains for each sieve was done under a particular dimension (A<38 µm /B<63 µm /<125 µm). Comparison with the initial distribution case and base case (average)
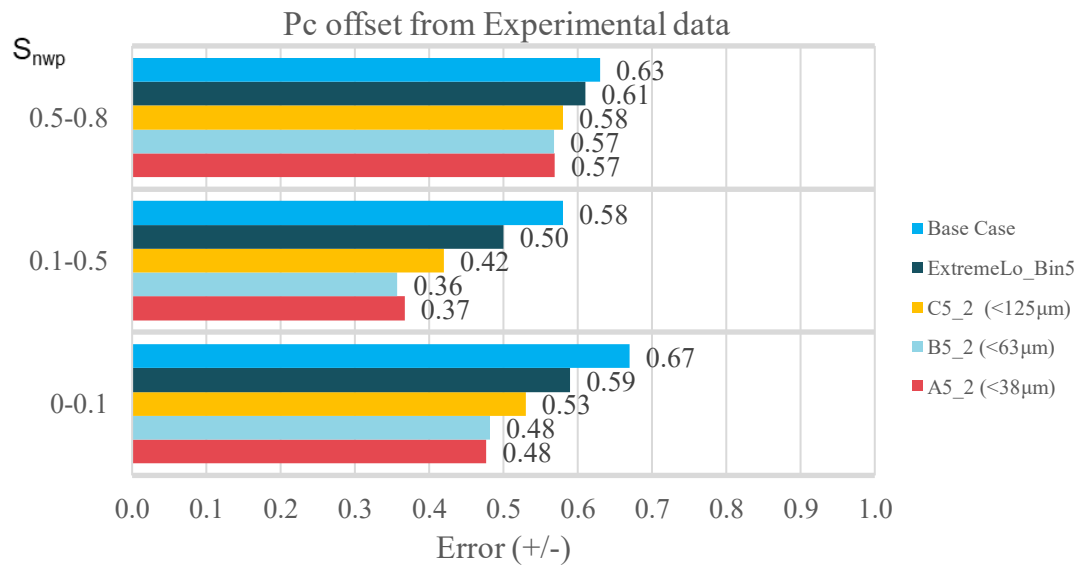
Figure 4.5 Comparison of error for each interval from the P_c curve between sphere cases.

To see how this distribution varies the rock properties, the permeability was also studied. In Table 3, the absolute permeabilities are shown and how they differ in each of the 3 directions for the simulations mentioned above. For the first cases A and B, the values are very close on all directions beside Z. The difference of permeabilities in Z cannot be accounted to any effect

other than the fact that probably in that direction, the B case has a more tortuous path and a smaller pore throat radius. In case C, where the variation of the larger size of grains occurs, the results show an increase in permeability and a decrease in capillary pressure curve. This can be easily seen in the MIPC data Figure 4.4.

Table 3 Absolute permeabilities values for the cases with spheres and bins of 5 distribution in the sieve intervals.

	A5_2 (<38μm) K [mD]	B5_2 (<63μm) K [mD]	C5_2 (<125 μm) K [mD]
X	2163.7	2169	2592.3
Y	2222	2222	2687
Z	2248	2024	2563

Looking at the pore throat radius distribution Figure 4.6 for these three cases, it can be noted that the pore sizes are far off. Same as the capillary pressure, the A5_2 and B5_2 models are about the same with a lower distribution for the A5_2 case. The C5_2 shows a deviation to the right in the upper grain size, which also translates to a lower capillary pressure curve. This comparison also indicates that due to the resolution below 1 micron, the data from the simulations is not available. The numbers in the case of spheres show that there is potential for getting closer to the real pore space. However, no more simulations could be performed to obtain a much better response by only using spheres. Analyzing the influencing parameters, it can be stated that varying in a certain number of bins does not influence so much the results. It introduces variety but more important is how the data is varied in those bins. So, the type of variation like Normal or Extreme in the lower or upper part needs to be taken into account. Also, this is linked with the type of rock analyzed (good or poorly sorted). In terms of bins, several (4 or 5) is enough to make a good distribution representation and therefore it can be stated that this is a sweet spot in terms of variation. Varying in certain intervals where more grains are present results in a good representation of the rock and a faster computational time. As most of the cases with spheres were considered it was decided to go to the next level and implement the use of ellipses together with spheres and enhance the level of heterogeneity.

d Sw / d Log Pore Throat Size vs Pore Throat Size
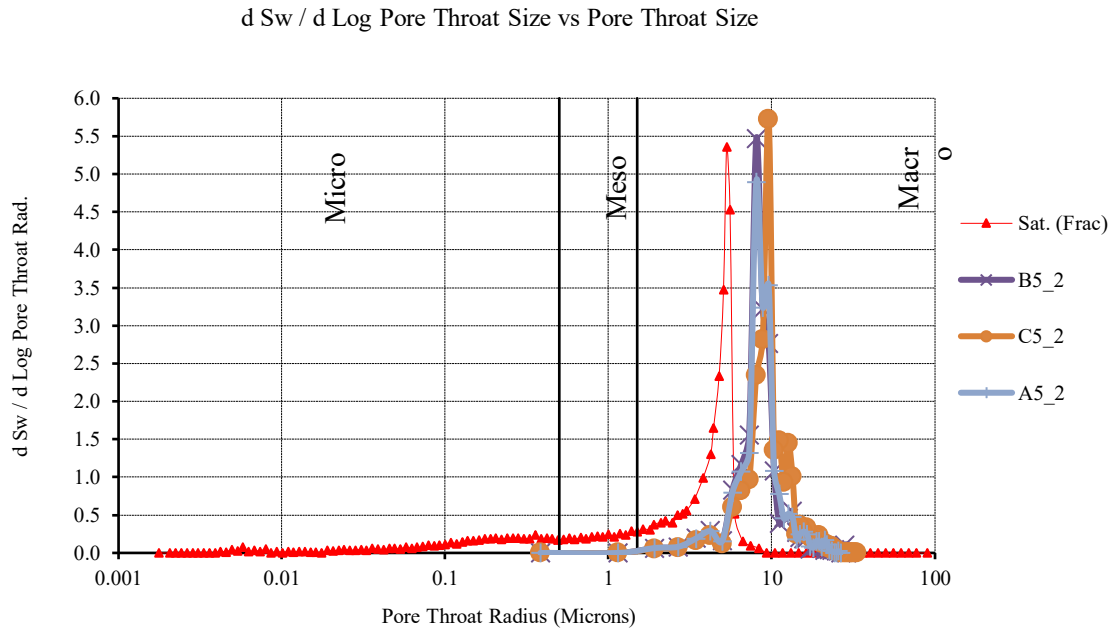
Figure 4.6 Pore throat radius distribution. With red is shown the experimental data

4.2   Spheres & Ellipses random packs simulations results

The use of ellipses in generating rock models is not new. Other authors also used ellipses as grains in simulating porous media characteristic. (Coelho, Thovert and Adler, 1997; Matsumura, Jenne and Jackson, 2015). Selecting the cases B5_2 and C5_2 was the choice for this simulation. Here, the shape was changed by maintaining the same distribution rules. The construction of the models was explained in the previous chapter.

The first four simulations were done on the case B5_2 (I, II, III and IV). Ellipses were considered in the upper part of the grain size distribution over 63 μm (Figure 4.7) and having the major axis between 63 and 250 microns, while the minor ones were 1.7 times less. These simulations are considering that the sieve analysis is not filtering most of the elongated grains by the minor axes, but by major.

Regarding the capillary pressure for the higher saturation of NWP, the model still not reaches the same curvature as the experimental data. Again, the entry pressure is not matched and most probably could be linked with the closure correction that should be done on the 3D model.
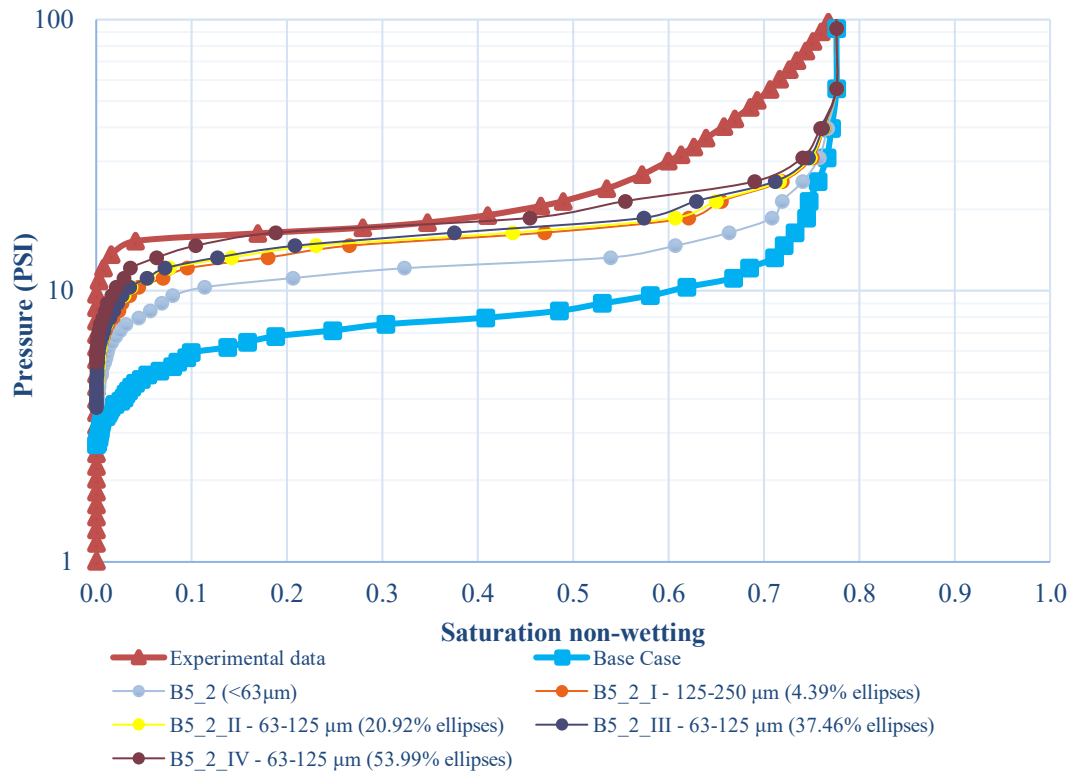
Figure 4.7 Capillary pressure curves for the sphere and ellipses cases. Ellipses are having the major axis over 63μm.

Based on the sensitivity analysis, the best result in terms of capillary pressure curve was obtained in the case where 53.99% per cent of grains over 63 μm were considered ellipses (B5_2_IV). In Figure 4.8, it can be seen in each zone how close the simulation is to the real P_c curve. In the case, B5_2_IV the plateau is almost fitted with an error value of 0.04. Compared to the first cases with spheres, the difference is almost 92%, the level of heterogeneity is increased and therefore it can be deemed, representative. For the entry pressure zone between 0 and 0.1 saturation, the values are somehow close at 0.19 deviation. Regarding the higher saturation zone, an improvement from the sphere cases is made but not high. The deviation is still 0.45 and the error is too high to assess that pore space. The other three simulations showed also an improvement and it can be stated that the results improve proportionally with the increase in the number of ellipses. This proves that changing the shape will affect the transport properties inside the porous space. As the number of ellipses increases the capillary pressure increases due to much more complex flow paths.

Pc offset from Experimental data
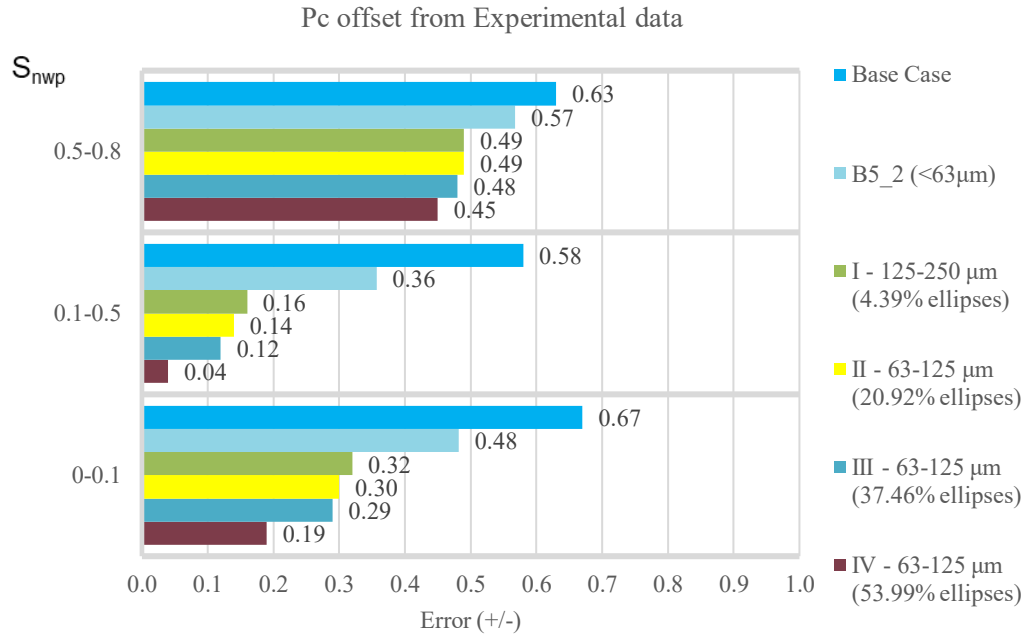
Figure 4.8 Sensitivity analysis spheres with ellipses varying in the upper interval.

In terms of pore throat size distribution, the results look confident, with the simulation of spheres and ellipses case B5_2_IV showing promising results. Even though the match of the entry pressure and the match at the higher saturation is not reached the pore throat size distribution has a close appearance to the one obtained experimentally.

d Sw / d Log Pore Throat Size vs Pore Throat Size
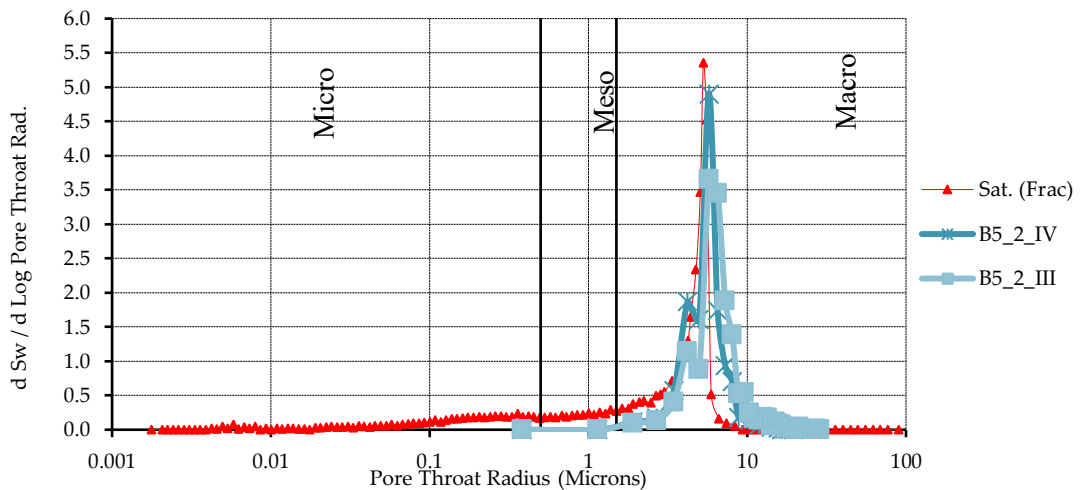
Figure 4.9 Pore throat size distribution. Red line represents the experimental data

Analyzing the absolute permeability values, it can be noticed that as the number of ellipses is increased, the pore throats are reduced, and therefore a decrease in permeability is obtained. The values of permeability from spheres are even 50% higher than the ones where ellipses were

considered. For the case with ellipses and spheres, the values of absolute permeability are going from around 1.3 D to 960 mD. The ellipses tend to reduce the pore throat size and therefore get a better fit with the MICP data even when a small percentage is considered. The values of permeabilities can be seen in Table 4.

Table 4 Absolute permeabilities values for the cases with spheres and ellipses

	B5_2 (<63μm) - spheres K [mD]	B5_2_I (4.39% ellipses) K [mD]	B5_2_II (20.92% ellipses) K [mD]	B5_2_III (37.46% ellipses) K [mD]	B5_2_IV (53.99% ellipses) K [mD]
X	2169	1300	1237	1182	960
Y	2222	1283	1234	1156	971
Z	2024	1277	1235	1206	970

Moving to models where ellipses account for the lower dimension in the sieve analysis (V, VI), the capillary pressure curve response is different, achieving higher entry pressure than any other simulations (Figure 4.10). In the cases where ellipses are between 38 and 63 μm (V), the results are showing a perfect match. On the contrary, when the variation is between 15 and 38 (VI), the values tend to increase more and obtain higher entry pressure. This shows that using predominantly ellipses in the lower part of the grain size interval results in an overestimated prediction of the transport properties. This is caused by the fact that a pack made of smaller grains creates a smaller pore throat, and therefore an increase in the pressure. This effect is seen in both cases, B and C, which are resulting in the same results overall. Hence, in the cases of sphere and ellipses, the difference between varying below 63 or 125 μm does not play a significant role as in the case of using only spheres and varying bins. This is a clear sign that the controlling parameter has been changed from spheres simulation where variation in grain dimensions was showing results to how the ellipses are distributed.

The sensitivity analysis performed on these cases resulted in a better response in the entry pressure range. From 0.19 deviation in the IV case to 0.14 in the V case with ellipses between 38 and 63 μm. The pressure at the plateau has the same error in correlation as before and the same is represented for the higher part of the saturation interval. No change is observed in the 0.5- 0.8 range as is clear now that to fit that part, the resolution should be increased. The other case (VI) is giving higher capillary pressure than the experimental data. Therefore the error in there is higher in all saturation ranges, besides the upper one where due to a higher entry pressure, a higher plateau is reached. Comparing the deviation for cases B and C where the

variation is different it can be seen that the same response is obtained. As mentioned before, this means that in the case of spheres and ellipses does not matter how we distribute, as it is more important the size that the ellipses have.
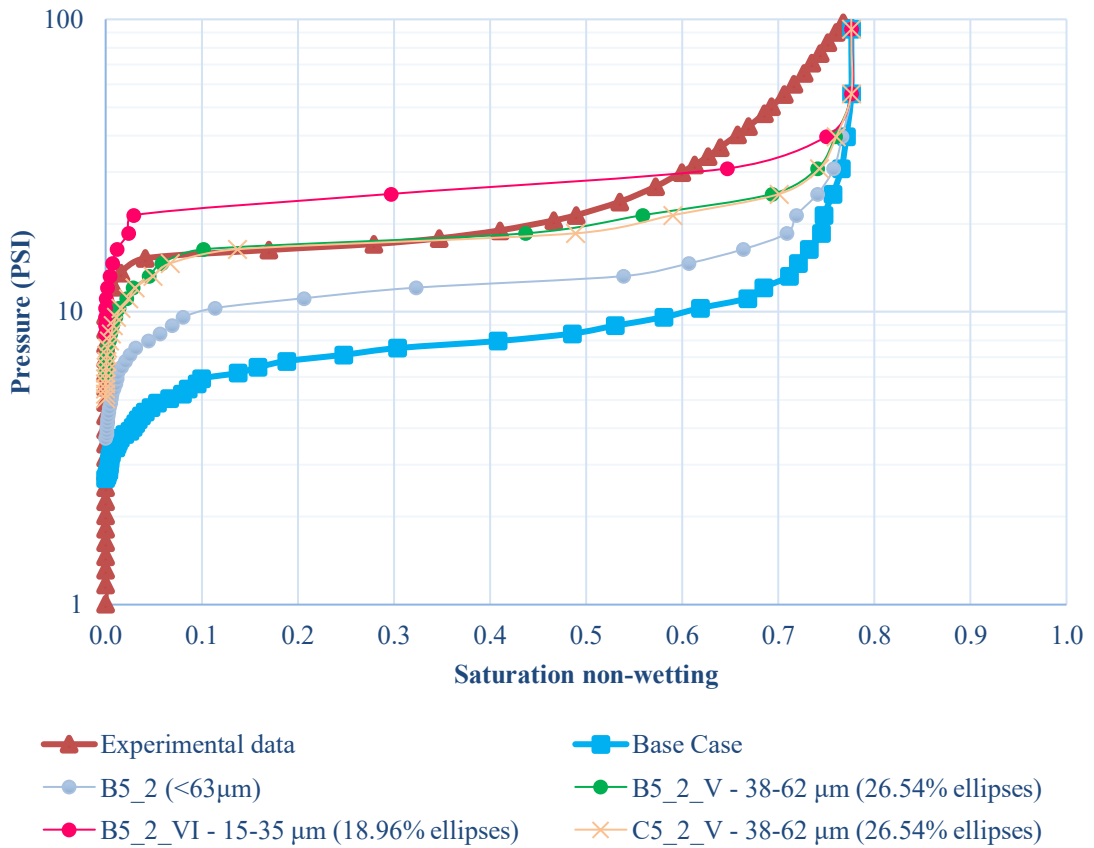
Figure 4.10 P_c curves of cases V and VI for sphere and ellipses.
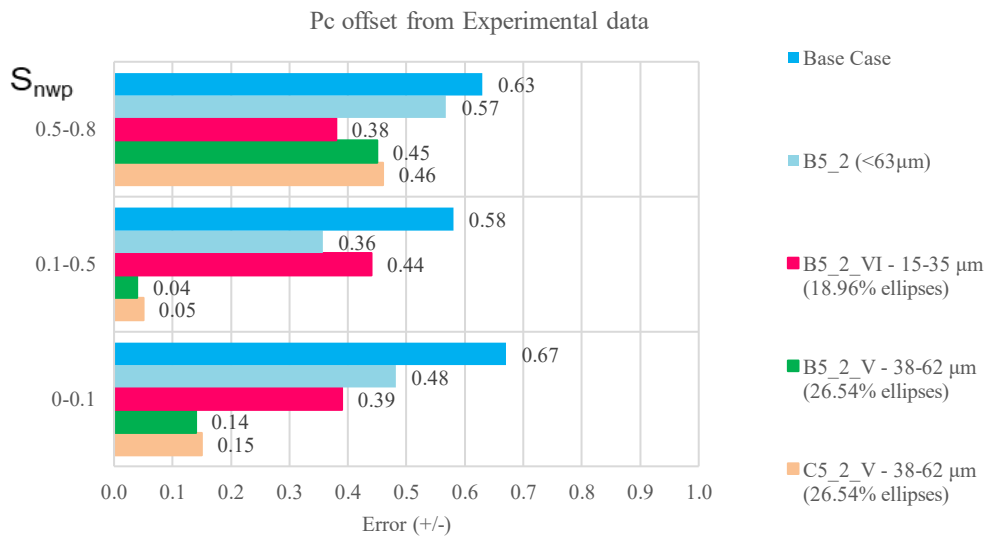
Figure 4.11 Sensitivity analysis for the sphere and ellipses cases when the lower intervals are considered.

Regarding pore throat size distribution, both cases B and C are showing suitable matches for case V. It is therefore easy to say that there is no single solution to this problem and by doing this sort of variation, more of them can be discovered.

d Sw / d Log Pore Throat Size vs Pore Throat Size
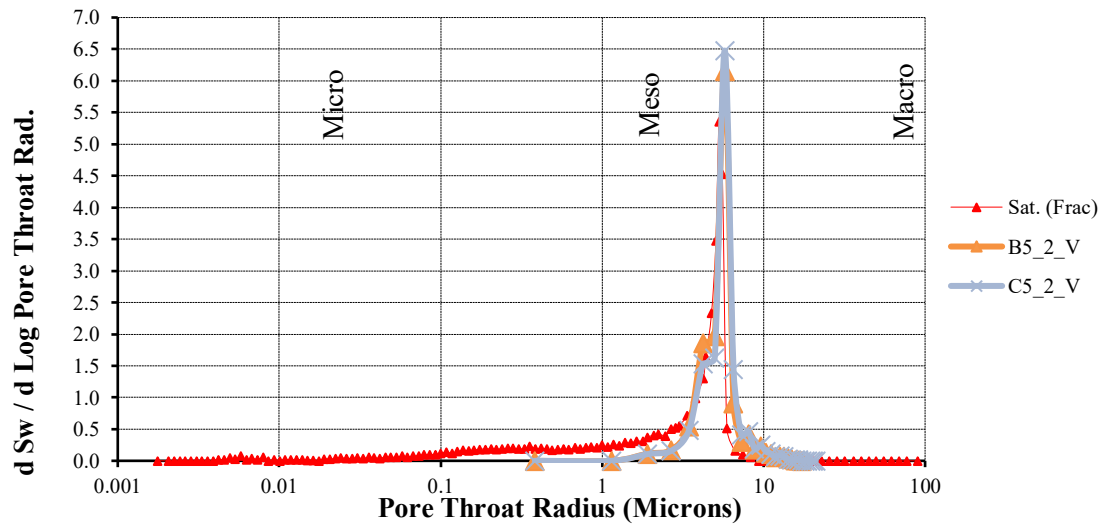
Figure 4.12 Pore throat size distribution for the B5_2_V/C5_2V. Red line represents the experimental data

Other cases were also done, considering that the value from the grain size distribution represents the minor axis, and the major is 1.7 times higher than the minor. This is representative for the cases when the sieve analysis manages to sort all the elongated grains based on the smallest diameter. In this situation, many of the ellipses will be larger than in previous cases. The variation is based on the same cases as before (V and VI), in the same intervals. So it is good to see what will be the effect if the axis is changed in such a way that the smaller axis of the ellipses is directly represented from the original grain size. The P_c curves for these simulations can be seen in Figure 4.13.

The cases VIII and IX show a lower capillary pressure than before. The difference in curves is somehow kept and looks like this change shifted the whole graph. This is caused by the fact that now the ellipses are in general larger than in other cases. For the case B5_2_IX (where the interval between 15 and 35 μm is considered to be representative of the minor axis of ellipses), the results show one of the best fit with the pore throat radius distribution (Figure 4.15). However, it is different from the case where major axis was represented from the GSD a minor was 1.7 times smaller. Considering that all the grain will pass by the smaller diameter means that the ellipses now are some of the biggest grains inside the model. Therefore the axes are changed and now the case that was having a higher pressure than the experimental data before become feasible. This can be seen in the sensitivity analysis (Figure 4.14). The cases with

ellipses between 38 and 62 microns on the minor axis have one of the highest deviations. One key take away here is that choosing how the data is analyzed can be significant to the overall results.
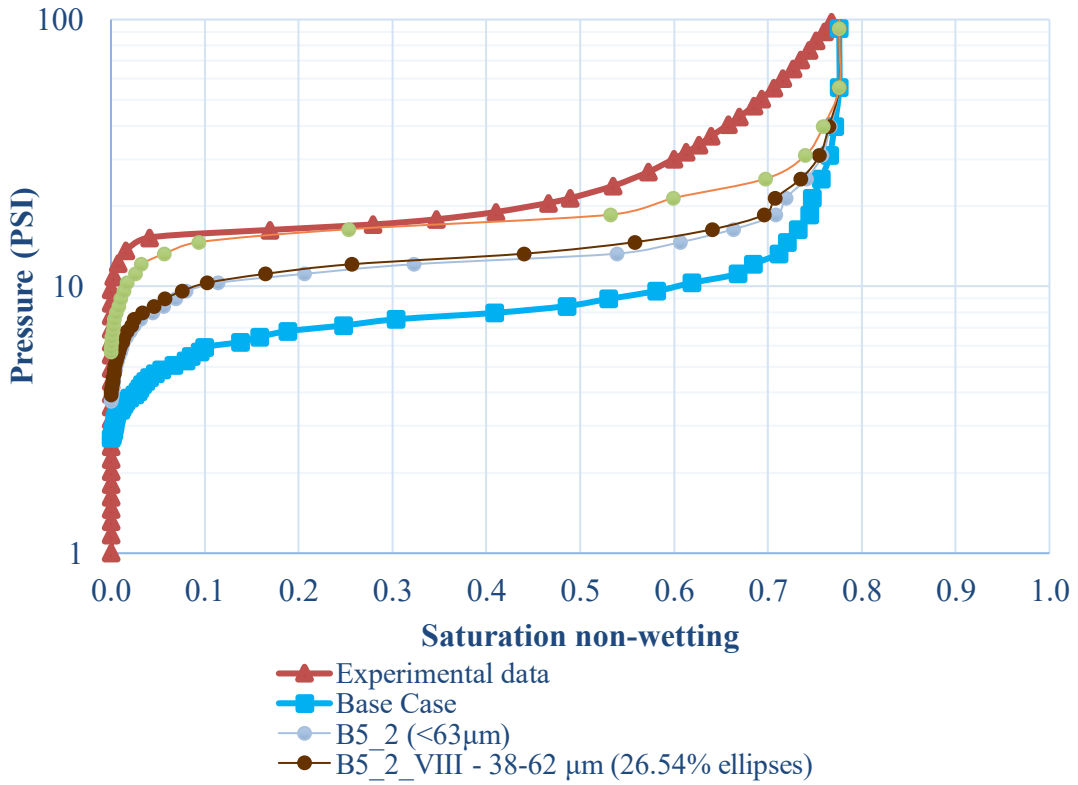
Figure 4.13 P_c curves of cases VIII, and X for sphere and ellipses.
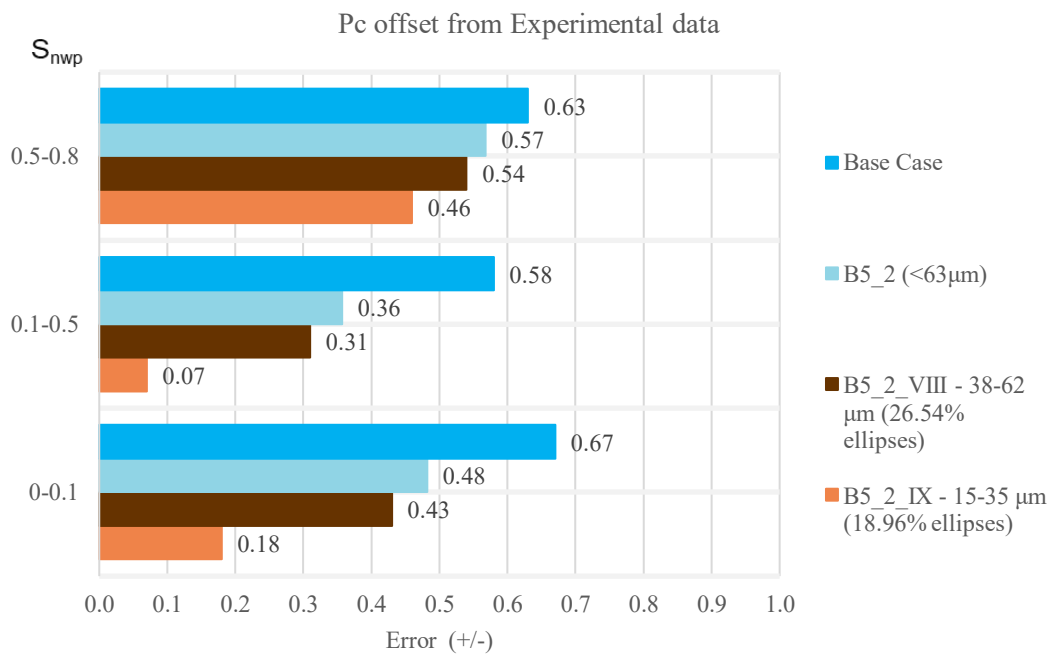
Figure 4.14 Sensitivity analysis for the sphere and ellipses cases when the major and minor axis are changed
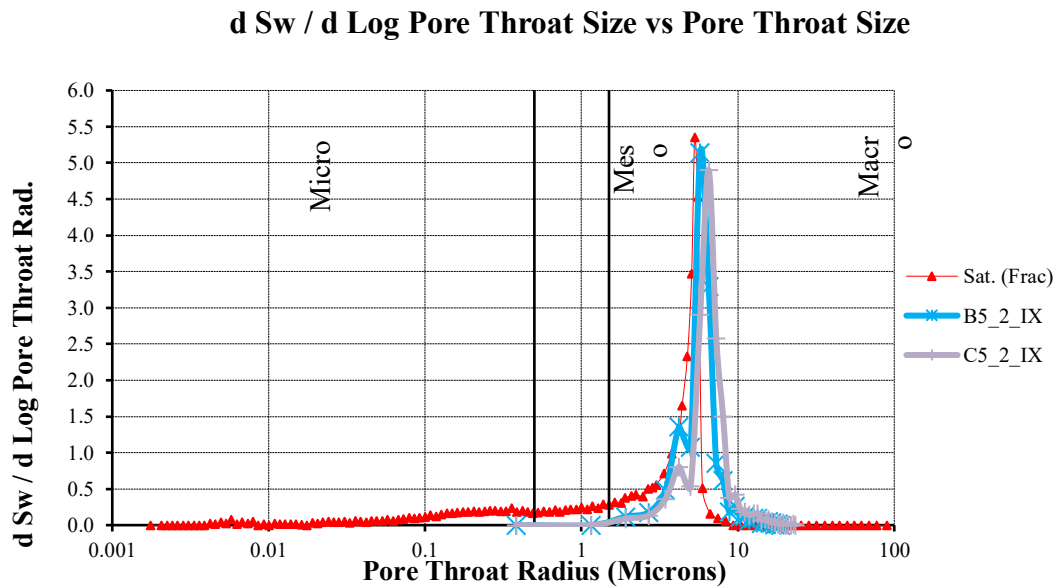
Figure 4.15 Pore throat size distribution for the B5_2_IX and C5_2_IX. Red line represents the experimental data

As presented in the methodology part, besides these cases, it was also tried to see how the anisotropy plays a role in the permeability measurements. All the simulations before were done isotropically, which means that in the orientation tensor the values on X, Y, Z direction were equal. The parameters chosen for the simulation of the cases were presented in Table 1.

In the anisotropic case, the permeability varies if the flow is directed only in specific directions. Simulations were based on the B5_2_III case, which has 37.46% of the grains over 63 μm ellipses. In Figure 4.16, it can be seen that in the direction in which the orientation occurs, the ellipses are more or less oriented into that direction.

In terms of absolute permeabilities, values around 1200 mD were obtained for each case in the direction of the oriented grains. For example for the case when they are oriented on the X directions, the permeabilities are 100 mD less due to the tortuous paths that are created and smaller pore throats that appear in the other two directions(Z, Y). In terms of capillary pressure, it could not be noticed a difference between this and the isotropic cases (Figure 4.17). The transport properties are somehow kept inside the model regarding the orientation of the grains, with only a small variation accounted for.

Anisotropy in X direction   Anisotropy in Y direction   Anisotropy in Z direction
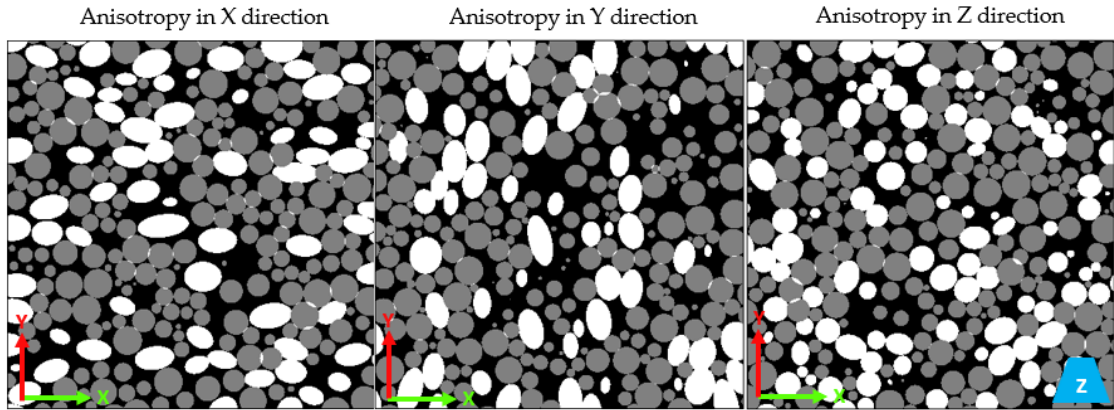
Figure 4.16 Images from the 3D model simulated in GeoDict and displayed in ImageJ. Here the orientation values in the tensor are 1(maximum) for each direction and 0 for the others
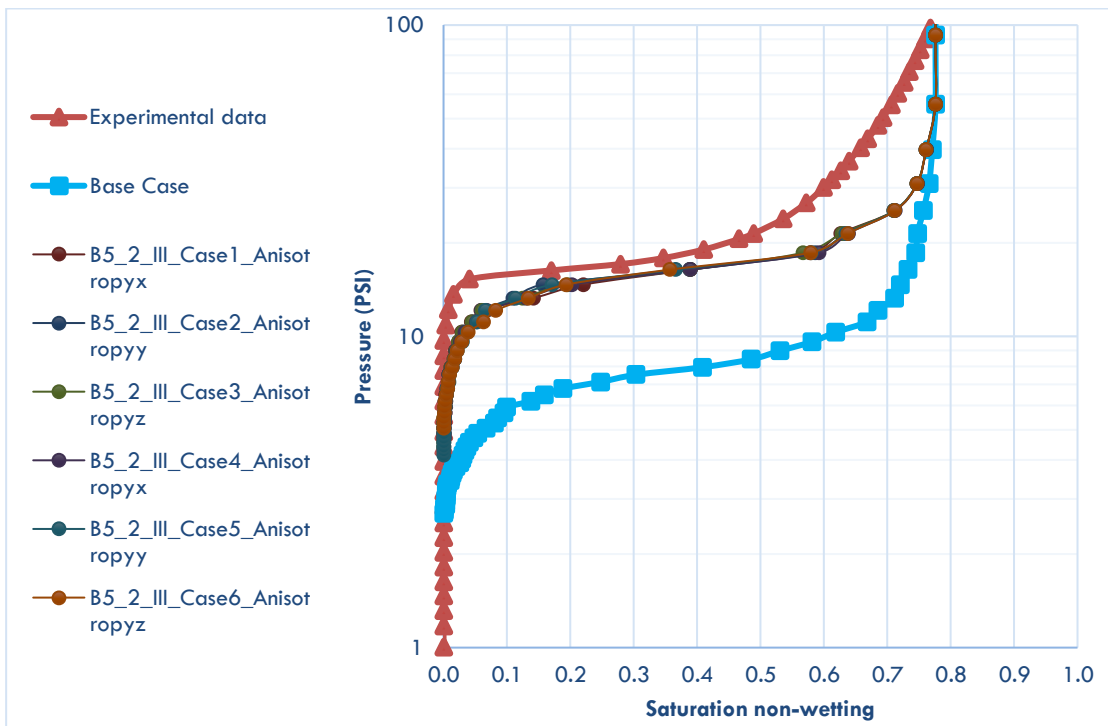
Figure 4.17 Capillary pressure curves for the anisotropic cases

As a summary regarding the improvement of the whole workflow in constructing rocks based on a randomly generated procedure, starting with the original grain size distribution the deviation from the experimental data is enhanced.

In Table 5 it can be seen the improvement rate in percentages for each of the simulations where the parameters were changed. It is noticeable that the only variation of bins is not creating a high effect and only after selecting to distribute in the intervals with a high percentage of grains, the results are improved. Either way, given the fact that the rock is heterogeneous, is hard to match the same transport properties by only using spheres. The moment ellipses are introduced a higher improvement of over 33% on the whole pore throat radius space is obtained. It is still

cumbersome to match the last part of the curve due to the low resolution of the micropores that needs higher computational power. There only 27-28% improvement could be reached. Overall, the entry pressure and plateau are better fitted with an improvement of 79% and 93% respectively. Hence, a further study might be needed to optimize the curve fitting for the higher saturation.

Table 5 Improvement referenced to the base case.

Saturation ranges	Sp(Base Case)	Sp(Varying bins)	Sp (Distribution<38μm) - A	Sp (Distribution<63μm) - B	Sp (Distribution<125μm) - C	Sp+Ell (ell = 63 - 250μm)	Sp+Ell(ell = 15- 63μm)	Sp+Ell(ell = 15- 63) *Diam - inv*
0-0.1	-	11.94 %	28.81 %	28.09 %	20.90 %	71.64 %	79.10 %	73.13 %
0.1-0.5	-	13.79 %	36.71 %	38.44 %	27.59 %	93.10 %	93.10 %	87.93 %
0.5-0.8	-	3.17 %	9.63 %	9.86 %	7.94 %	28.57 %	28.57 %	26.98 %
Overall	-	5.56 %	13.89 %	13.89 %	9.72 %	33.33 %	33.33 %	31.94 %

Based on the improvement presented the parameters were ranked on their rate of improvement. The effect is also explained in Table 6.

Table 6 Parameters from simulations and their effect on the models created

#	Parameters	Effect
1	Shape	High improvement achieved. Modifying the shape creates heterogeneity for improvement in the overall results. As the number of ellipses increases higher Capillary Pressure is obtained.
2	Ellipses dimensions	High improvement achieved. Having ellipses in the lower dimensions has a bigger effect on the P_c-curve. This is caused by the fact that the packing of smaller grains creates smaller pore throats, therefore increasing the capillary pressure.
3	Distribution under certain intervals	Medium impact from the original GSD. It results in higher capillary pressure when the distribution is done in smaller intervals. The drawback is that is not representing the heterogeneity in the model. The benefit is that the simulation is faster.
4	Varying in bins	Low improvement from original GSD. Creates variations between highest and lowest pressure. Helps identify the ranges in which the preliminary results are.
5	Anisotropy	No improvement

4.3 Spheres & Ellipses sedimentation simulations results

The results for the process-based modelling (Bakke and Øren, 1997; Øren, Bakke and Arntzen, 1998; Øren and Bakke, 2002) showed that due to the way the simulator in building the model, the entry pressure is heavily affected. Two faces of the cube are filled with grains in such a way that large cavities remain. The results for the MICP simulated experiment and pore throat radius distribution can be seen below. It was decided to not proceed further with this method as the random packings are already a better choice and yield tangible results, with different simulations scenarios.
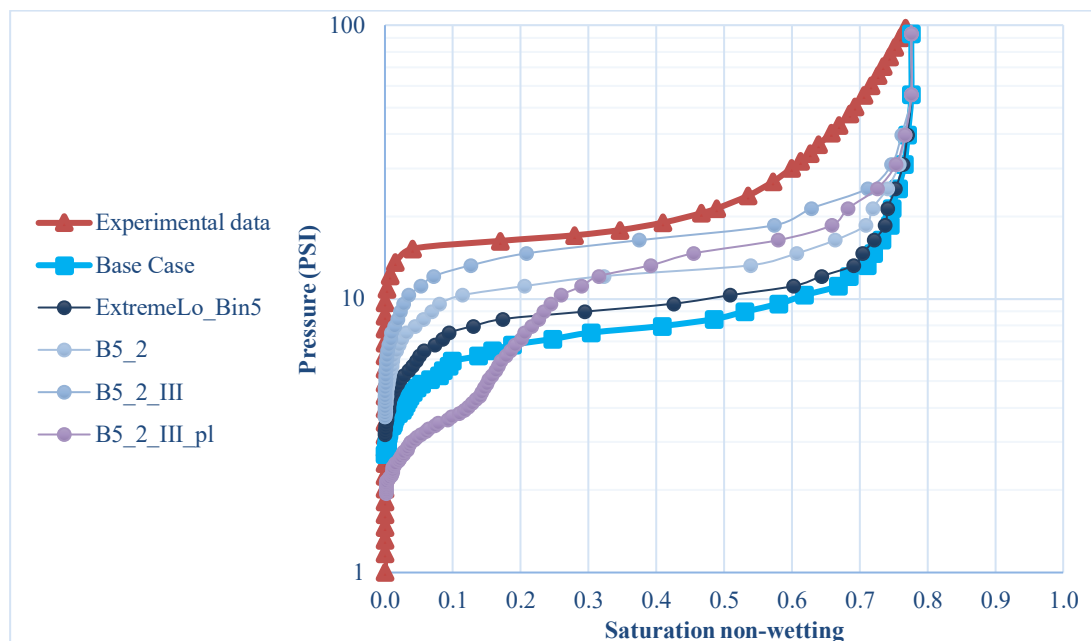
Figure 4.18 Capillary pressure curve for the case where pile grains and sinter and crystallization was used. Based on the GSD of B5_2_III

In terms of pore throat radius distribution, it is showing a very different situation, and the models look like it has a double porosity. Even though such a thing is not possible, it might be caused by the voids on the boundaries that have larger pore throats than the ones inside the model.

d Sw / d Log Pore Throat Size vs Pore Throat Size
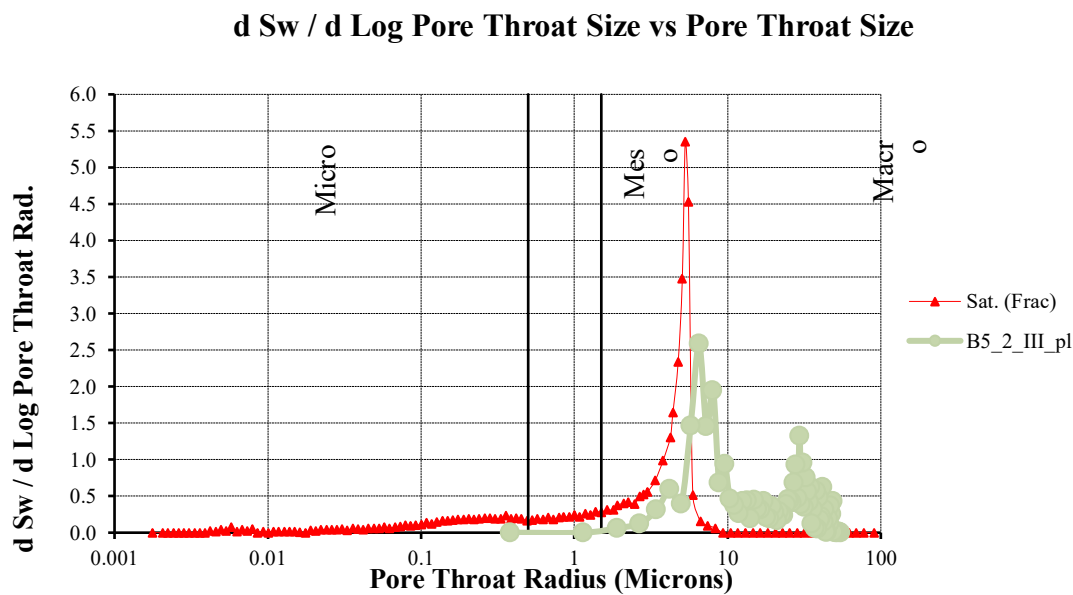
Figure 4.19 Pore throat size distribution for the case with pile grains simulation and sinter and crystallization. Based on the GSD of B5_2_III. Red line represents the experimental data

4.4 Developed workflow and relative permeabilities

After the matching of the pore throat radius was conducted and different models obtained promising results in the entry pressure and plateau region, relative permeabilities for a few probes, were calculated along with the development of a workflow for analyzing the data and getting the same transport properties as the real rocks.

Relative permeabilities curve were obtained for some models with both spheres and spheres and ellipses. (Figure 4.20, Figure 4.21). Although they were obtained, the validity of them is low as the curve fitting was not realized on the whole saturation range. Another problem encountered is that during the imbibition simulation, the pore morphology method cannot measure the forced part. The simulation stops at P_c=0 as the process cannot go further, and we do not have a good understanding of the forced part of the imbibition. Nevertheless, we get a residual oil saturation (S_{or}), but this cannot be considered. Moreover, the pore morphological approach that the software uses also does not consider the ganglion dynamics (Berg *et al.*, 2016). While the simulation is performed since the oil phase is deemed to be solid, the inaccessible pore space is increased much faster, thus resulting in a higher residual oil saturation as the water cannot displace the oil.

The sensitive analysis for the relative permeabilities, show less variation both in Imbibition and Drainage case even with spheres or 50% ellipses. This shows promising results for future use

of this method in the case when we are clueless about how the real permeabilities look like in the field.
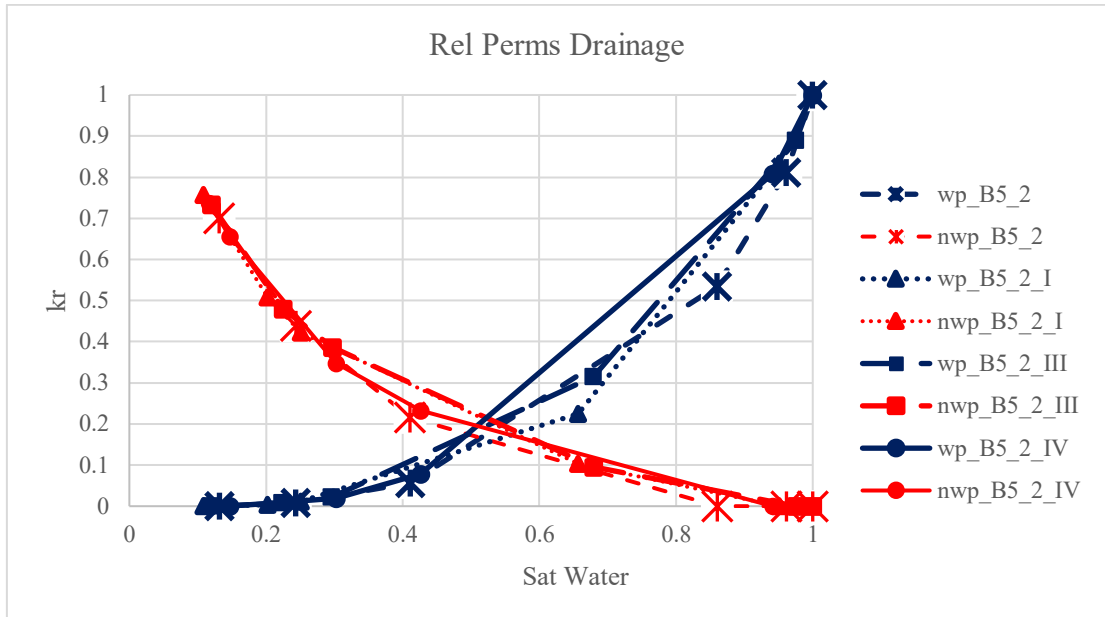
Figure 4.20 Relative permeabilities in the drainage case for the cases varying from the only sphere to cases with spheres
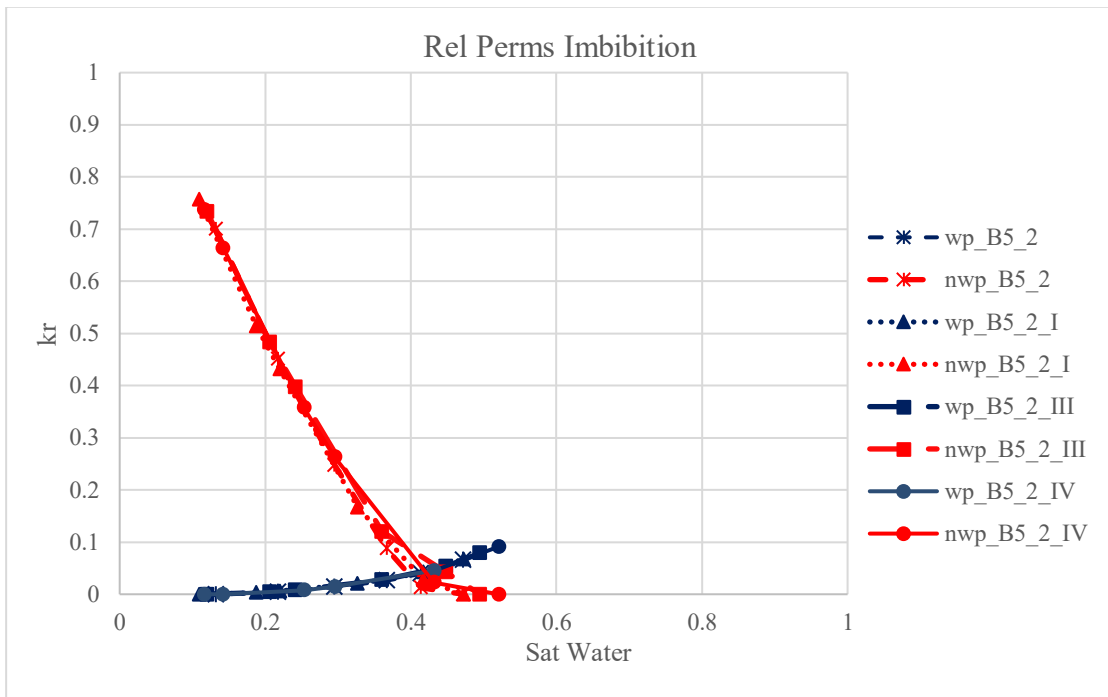
Figure 4.21 Relative permeabilities in the imbibition case for the cases varying from the only sphere to cases with spheres

The workflow that can be extracted after running multiple simulations on probe B16390 can be summarized in the diagram below.
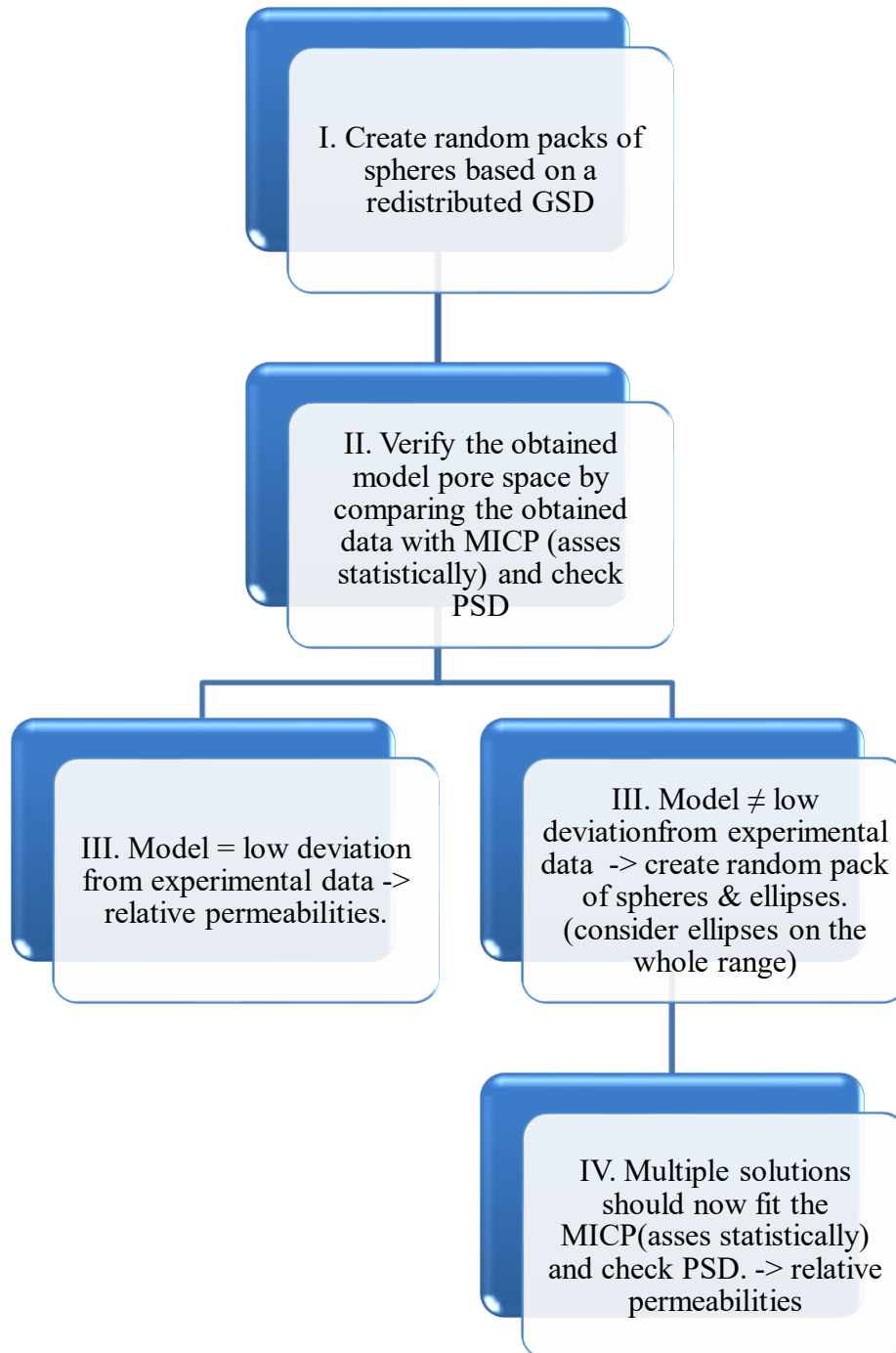
Figure 4.22 Diagram of the workflow designed to mimic the transport properties and derive relative permeabilities

Chapter 5

Conclusion

5.1 Summary

The results obtained by sphere packs compared with other cases from literature (Bryant and Blunt, 1992; Bryant, King and Mellor, 1993; Hilpert and Miller, 2001; Silin et al., 2011) show that with only randomly packed spheres a suitable match cannot be obtained. The rock is not homogeneous and therefore the sphere packs are not a good representation for such a case.

Sieve analysis done on smaller sieve intervals coupled with a change of shape can create a 3D rock while evaluating the unconsolidated material. Multiple models give the same MICP response and fit the PSD. Multiple solutions exist for the same rock.

The time frame for the simulation is relatively small once a proper working workflow is established. In the end, the workflow was developed to create 3D models of unconsolidated rocks on basis of a grain size distribution. However further investigations are needed to fit the capillary pressure curve behaviour close to the resolution limit.

Computational and model limitations should be clearly defined. The porosity provides a good measure as stopping criteria but might need some reevaluation on basis of the aforenamed limitations. Many bins create a problem with simulators handling the data. Pore morphology methods have a problem with modelling imbibition processes.

Distributing higher percentages in smaller grains results in higher capillary pressure. Permeability is also higher in the case where variation takes place in the bigger dimension grains.

It is easier to fit the plateau of a capillary pressure curve and the entry pressure than with the saturations close to the resolution limit. The deviations from experimental data are acceptable and the models represent the pore throat size distributions in a reasonable way for Meso and Macro pores. The rock models created did not represent micropores at all. Therefore, a later study should come to address this problem.

Factors that are influencing the applicability of the workflow are shape, ellipses dimension, distribution under certain intervals and the number of bins. Each affects the model individually but the one with the highest effect is the shape. Once ellipses are considered the capillary pressure is changing dramatically. Anisotropy does not have any influence on the MICP curve.

In the case when the model is created by simulating the sedimentation and overgrowth of minerals, the results did not match the experimental data at all. Due to problems with the model generation that leaves bigger cavities on the deposition faces, closure effects appear.

5.2   Future work

As the workflow still has a problem in evaluating the pore space in the smaller sizes, a next study based on that region should be conducted. Moreover, since only one probe could be analyzed given the scarcity of the data, this workflow should be validated on multiple heterogeneous probes until a clear methodology can be implemented to work in any rock from any basin around the world. Finally, the study can be expanded to assess the influence of other models of grains beside sphere and ellipses and comprise factors like wettability and contact angles for a better flow simulation.

Chapter 6

References

Bakke, S. and Øren, P. E. (1997) '3-D pore-scale modelling of sandstones and flow simulations in the pore networks', *SPE Journal*, 2(2), pp. 136–149. doi: 10.2118/35479-PA.

Berg, C. F., Lopez, O. and Berland, H. (2017) 'Industrial applications of digital rock technology', *Journal of Petroleum Science and Engineering*, 157(March), pp. 131–147. doi: 10.1016/j.petrol.2017.06.074.

Berg, S. *et al.* (2016) 'Connected pathway relative permeability from pore-scale imaging of imbibition', *Advances in Water Resources*, 90(February), pp. 24–35. doi: 10.1016/j.advwatres.2016.01.010.

Blunt, M. J. *et al.* (2013) 'Pore-scale imaging and modelling', *Advances in Water Resources*, 51(January), pp. 197–216. doi: 10.1016/j.advwatres.2012.03.003.

Bosl, W. J. and Nur, A. (1998) 'A study of porosity and permeability using a lattice Boltzmann simulation', *Geophysical Research Letters*, 25(9), pp. 1475–1478. doi: 10.1029/98GL00859.

Bryant, S. and Blunt, M. (1992) 'Prediction of relative permeability in simple porous media', *Physical Review A*, 46(4), pp. 2004–2011. doi: 10.1103/PhysRevA.46.2004.

Bryant, S. L., King, P. R. and Mellor, D. W. (1993) 'Network model evaluation of permeability and spatial correlation in a real random sphere packing', *Transport in Porous Media*, 11(1), pp. 53–70. doi: 10.1007/BF00614635.

Celia Magno, M. *et al.* (2018) 'A comparison between Laser Granulometer and Sedigraph in grain size analysis of marine sediments', *Measurement: Journal of the International Measurement Confederation*, 128(January 2018), pp. 231–236. doi: 10.1016/j.measurement.2018.06.055.

Coelho, D., Thovert, J.-F. and Adler, P. M. (1997) 'Geometrical and transport properties of

random packings of spheres and aspherical particles', *Physical Review E*, 77(6), p. 066306. Available at: https://doi.org/10.1103/PhysRevE.55.1959.

Fatt, I. (1956) 'The Network Model of Porous Media', *Transactions of the AIME*, 207(01), pp. 144–181. doi: 10.2118/574-g.

Fingerle, M., Rief, S. and Planas, B. (2020) *Grain Geo Manual 2020*. Math2Market.

Finney, J. L. (1970) 'Random packings and the structure of simple liquids. I. The geometry of random close packing', *Proceedings of the Royal Society of London. A. Mathematical and Physical Sciences*, 319(1539), pp. 479–493. doi: 10.1098/rspa.1970.0189.

Glover, P. (2016) 'Chapter 1 Introduction', in *MSc Course Formation Evaluation University of Leeds*, pp. 1–5.

Goldfarb, E. J., Ikeda, K. and Tisato, N. (2018) 'Constraining the effect of image resolution in digital rock physics without segmentation', in *SEG Technical Program Expanded Abstracts 2018*. Society of Exploration Geophysicists, pp. 3688–3692. doi: 10.1190/segam2018-2997871.1.

Goral, J. *et al.* (2020) 'Confinement Effect on Porosity and Permeability of Shales', *Scientific Reports*, 10(1). doi: 10.1038/s41598-019-56885-y.

Guodong, J., Patzek, T. and Silin, D. (2004) 'Direct Prediction of the Absolute Permeability of Unconsolidated and Consolidated Reservoir Rock'. doi: 10.2523/90084-ms.

Handoyo *et al.* (2017) 'Introduction to Digital Rock Physics and Predictive Rock Properties of Reservoir Sandstone', *IOP Conference Series: Earth and Environmental Science*, 62(1), p. 012022. doi: 10.1088/1755-1315/62/1/012022.

Hazlett, R. D. (1995) 'Simulation of capillary-dominated displacements in microtomographic images of reservoir rocks', *Transport in Porous Media*, 20(1–2), pp. 21–35. doi: 10.1007/BF00616924.

Hilden, J., Linden, S. and Planas, B. (2020) *Flow Dict Manual 2020*.

Hilpert, M. and Miller, C. T. (2001) 'Pore-morphology-based simulation of drainage in totally wetting porous media', *Advances in Water Resources*, 24(3–4), pp. 243–255. doi: 10.1016/S0309-1708(00)00056-7.

Hunter, S., Hofmann, R. and Espejo, I. (2018) 'Integrating grain-scale geology in digital rock physics', *Leading Edge*, 37(6), pp. 428–434. doi: 10.1190/tle37060428.1.

Huntley, H. (1974) 'The golden ellipse', *The fibonacci quarterly*, 12, pp. 38–40.

Iowa, U. of (2020) *Stereology*. Available at: https://cmrf.research.uiowa.edu/stereology-

0#:~:text=The principle of Delesse,has an area of ap. (Accessed: 7 October 2020).

King, M. J. *et al.* (1986) 'Simultaneous determination of Residual saturation and capillary pressure curves utilizing the ultracentrifuge', *Proceedings - SPE Annual Technical Conference and Exhibition*. doi: 10.2118/15595-ms.

Lehmann, P. *et al.* (2006) 'Tomographical Imaging and Mathematical Description of Porous Media Used for the Prediction of Fluid Distribution', *Vadose Zone Journal*, 5(1), pp. 80–97. doi: 10.2136/vzj2004.0177.

Linden, S., Wiegmann, A. and Hagen, H. (2015) 'The LIR space partitioning system applied to the Stokes equations', *Graphical Models*, 82, pp. 58–66. doi: 10.1016/j.gmod.2015.06.003.

Liu, T., Jin, X. and Wang, M. (2018) 'Critical Resolution and Sample Size of Digital Rock Analysis for Unconventional Reservoirs', *Energies*, 11(7), p. 1798. doi: 10.3390/en11071798.

Lopez, O. *et al.* (2010) 'Investigation Into the Reliability of Predictive Pore-Scale Modeling for Siliciclastic Reservoir Rocks', *International Symposium of the Society of Core Analysts*, pp. 1–12. Available at: papers2://publication/uuid/CF5F6D43-D75A-4842-93AC-DEB5A1EAC677.

Matsumura, Y., Jenne, D. and Jackson, T. L. (2015) 'Numerical simulation of fluid flow through random packs of ellipses', *Physics of Fluids*, 27(2). doi: 10.1063/1.4907409.

McPhee, C., Reed, J. and Zubizarreta, I. (2015) 'Core Analysis A Best Practice Guide', in *Development in Petroleum Sciences*, pp. 2–829. doi: 10.1016/B978-0-444-63533-4.09991-1.

Mitiguy, P. (2009) 'Chapter 2 - Vectors', in *Course Notes Standford Advanced Dynamics: ME331B*, pp. 5–13.

Øren, P. E. and Bakke, S. (2002) 'Process based reconstruction of sandstones and prediction of transport properties', *Transport in Porous Media*, 46(2–3), pp. 311–343. doi: 10.1023/A:1015031122338.

Øren, P. E. and Bakke, S. (2003) 'Reconstruction of Berea sandstone and pore-scale modelling of wettability effects', *Journal of Petroleum Science and Engineering*, 39(3–4), pp. 177–199. doi: 10.1016/S0920-4105(03)00062-7.

Øren, P. E., Bakke, S. and Arntzen, O. J. (1998) 'Extending Predictive Capabilities to Network Models', *SPE Journal*, 3(4), pp. 324–335. doi: 10.2118/52052-pa.

Pickell, J. J., Swanson, B. F. and Hickman, W. B. (1966) 'Application of Air-Mercury and Oil-Air Capillary Pressure Data In the Study of Pore Structure and Fluid Distribution', *Society of Petroleum Engineers Journal*, 6(01), pp. 55–61. doi: 10.2118/1227-pa.

Ramstad, T. *et al.* (2012) 'Relative Permeability Calculations from Two-Phase Flow Simulations Directly on Digital Images of Porous Rocks', *Transport in Porous Media*, 94(2), pp. 487–504. doi: 10.1007/s11242-011-9877-8.

Rassenfoss, S. (2011) 'Digital rocks out to become a core technology', *JPT, Journal of Petroleum Technology*, 63(5), pp. 36–41. doi: 10.2118/0511-0036-JPT.

Rosen, R. *et al.* (2007) 'Recent Experience With Unconsolidated Core Analysis', *Society*, pp. 1–6.

Silin, D. *et al.* (2011) 'Microtomography and Pore-Scale Modeling of Two-Phase Fluid Distribution', *Transport in Porous Media*, 86(2), pp. 495–515. doi: 10.1007/s11242-010-9636-2.

Silin, D. and Patzek, T. (2006) 'Pore space morphology analysis using maximal inscribed spheres', *Physica A: Statistical Mechanics and its Applications*, 371(2), pp. 336–360. doi: 10.1016/j.physa.2006.04.048.

Di Stefano, C., Ferro, V. and Mirabile, S. (2010) 'Comparison between grain-size analyses using laser diffraction and sedimentation methods', *Biosystems Engineering*, 106(2), pp. 205–215. doi: 10.1016/j.biosystemseng.2010.03.013.

Swanson, B. F. (1979) 'Visualizing Pores and Nonwetting Phase in Porous Rock.', *JPT, Journal of Petroleum Technology*, 31(1), pp. 10–18. doi: 10.2118/6857-PA.

Ward, C. W. (1962) 'METHOD AND A APARATUS FOR SIFTNG'.

Widera, A., Linden, S. and Planas, B. (2020) *Satu Dict Manual 2020*.

Appendix A

Original Data

WFT Lab ID	Shape	Depth (m or ft.)	Lithofacies	Length (cm)	Diameter (cm)	L*A Bulk volume (ml)	Grain volume (ml)	Grain density (g/cc)	Porosity (frac.)	Hg Bulk volume (ml)	Arch Bulk volume (ml)	K_L (mD)	Comment
B16397	1.5" plug	1450 - 1452	Helvetian	3.86	3.82	44.24	36.7	2.72	0.202		46.0	24.0	
B16407a	1" plug	2205 - 2208	Helvetian	3.80	2.50	18.65	15.7	2.69	0.147	18.40	17.9	18.2	
B16407b	1" plug	2205 - 2208	Helvetian	2.97	2.50	14.58	12.2	2.69	0.151	14.38	14.4	10.5	
B16411a	1" plug	1727 - 1732	Helvetian	3.89	2.49	18.94	15.6	2.68	0.147	18.27	18.5	21.5	
B16411b	1" plug	1727 - 1732	Helvetian	4.72	2.50	23.17	19.3	2.68	0.146	22.54	23.0	51.9	
B16408	1" plug	2205 - 2208	Helvetian	1.38	2.49	6.72	5.7	2.68	0.159	6.72		NMP	To short for successful K_L measurement
B16387	Chip	300 - 302	Dacian				18.3	2.67	0.353		28.2		
B16388	Chip	300 - 302	Dacian				23.7	2.68	0.347		36.2		
B16389	Chip	515 - 519	Dacian				27.0	2.66			NMP		Sample disintegrated during saturation
B16390a	Chip	515 - 519	Dacian				6.1	2.79	0.392	10.0			Sample disintegrated during saturation
B16391	Chip	528 - 532	Dacian					2.73	0.379			1.41E-03	Crushed rock analysis
B16392	Chip	528 - 532	Dacian					2.72	0.358			9.36E-04	Crushed rock analysis
B16393	Chip	150 - 153	Dacian					2.71	0.277			5.31E-04	Crushed rock analysis
B16394	Chip	150 - 153	Dacian					2.72	0.268			8.59E-04	Crushed rock analysis
B16395	Chip	1655 - 1657	Helvetian				24.5	2.70	0.145		28.7		
B16396	Chip	1655 - 1657	Helvetian				27.4	2.75	0.245	36.29	37.5		
B16398	Chip	1450 - 1452	Helvetian				28.1	2.70	0.139	32.66			
B16399B	Chip	1515 - 1517	Helvetian				11.8	2.66	0.279		16.4		
B16401	Chip	2004 - 2006	Helvetian				15.2	2.71	0.186		18.7		
B16402	Chip	2004 - 2006	Helvetian				11.5	2.75	0.197	14.36			
B16403	Chip	1425 - 1429	Helvetian				32.7	2.71	0.105	36.52			
B16404	Chip	1425 - 1429	Helvetian				9.0	2.77	0.113	10.09			
B16405	Chip	1996 - 1999	Helvetian				29.8	2.67	0.139	34.65			
B16406	Chip	1996 - 1999	Helvetian				35.2	2.67	0.120		40.0		
B16409	Chip	2141 - 2143	Helvetian				7.4	2.75	0.178		9.0		
B16410	Chip	2141 - 2143	Helvetian				39.5	2.69	0.190		48.7		
B16412	Chip	1727 - 1732	Helvetian				33.3	2.67	0.184		40.8		

Grain Size Distribution – Probe B16390

Depth	: 515 - 519 m
Original total weight	: 20.033 g
Retained total weight	: 19.955 g
Material source:	Core chips

SIEVE APPARATURE	WEIGHT RETAINED	WEIGHT PERCENTAGES RETAINED	
μ	g	ind. %	Cum. %
1000	0.005	0.03	0.03
500	0.014	0.07	0.10
250	0.108	0.54	0.64
125	0.749	3.75	4.39
63	9.898	49.60	53.99
38	5.299	26.55	80.55
15	3.768	18.88	99.43
Less than 15	0.114	0.57	100.00

Sample no.	WFTL lab ID	Sample type	Φ (He Por)	GD	K Swanson	Φ	Sw - Pore throat radius 0.1 micron	Sw - Pore throat radius 0.26 micron	Pore Throat Rad. (microns)	Hg Injection Pressure (psia)
			amb.	amb.						
			20°C	20°C	MICP	MICP	MICP	MICP	(Mode)	Pth
	(m/ft)		(fraction)	(g/ml)	(mD)	(fraction)	(fraction)	(fraction)	(micron)	(psia)
1	B16387	End trim	0.353	2.68	3.50	0.321	0.367	0.635	0.149	6.91
2	B16388	End trim	0.385	2.71	0.867	0.335	0.385	0.938	0.240	184.54
3	B16390	End trim	0.422	2.72	349	0.404	0.057	0.131	5.554	10.86
4	B16391	End trim	0.365	2.72	3.48	0.333	0.228	0.469	0.417	30.04
5	B16392	End trim	0.419	2.77	n/a	n/a	n/a	n/a	n/a	n/a
6	B16393	End trim	0.270	2.73	0.714	0.239	0.331	0.681	0.118	32.34
7	B16394	End trim	0.345	2.88	n/a	n/a	n/a	n/a	n/a	n/a
8	B16395	End trim	0.163	2.73	0.007	0.124	1.000	1.000	0.024	1841.26
9	B16396	End trim	0.278	2.74	12.51	0.221	0.557	0.711	0.062	6.19
10	B16397	SCAL/1.5"/end trim	0.180	2.71	0.006	0.129	1.000	1.000	0.021	1992.67
11	B16398	End trim	0.152	2.70	0.033	0.115	0.773	0.893	0.019	114.45
12	B16401	End trim	0.186	2.69	3.72	0.153	0.182	0.316	1.003	17.07
13	B16402	End trim	0.193	2.67	4.14	0.145	0.190	0.310	2.039	10.85
14	B16403	End trim	0.099	2.70	25.8	0.081	0.533	0.704	0.079	1.18
15	B16404	End trim	0.088	2.70	0.021	0.061	0.614	0.848	0.039	97.18
16	B16405	End trim	0.139	2.68	1.55	0.088	0.186	0.291	0.932	8.66
17	B16406	End trim	0.128	2.68	1.38	0.086	0.192	0.309	1.170	26.85
18	B16407	CCA/1"/end trim	0.171	2.69	7.06	0.133	0.154	0.264	3.011	12.16
19	B16408	CCA/1"/end trim	0.160	2.67	2.88	0.114	0.173	0.290	1.620	12.17
20	B16409	End trim	0.205	2.69	11.1	0.138	0.115	0.193	3.011	10.85
21	B16410	End trim	0.193	2.69	3.87	0.140	0.185	0.313	1.483	12.16
22	B16411	SCAL/1"/end trim	0.167	2.68	2.35	0.110	0.173	0.313	1.079	12.16
23	B16412	End trim	0.201	2.66	11.9	0.172	0.120	0.212	1.736	7.75

Samples failed during analysis

Appendix B

Naming criteria for the simulations with spheres

The naming of each case is explained in the list below. For a graphical explanation, the figures are presented with each case.

- Flat = flat distribution
- Normal = normal Gaussian Distribution
- ExtremeNor = normal distribution with more extreme values in the middle
- Parabolic = distribution that looks like a parabola
- ExtremePara = parabolic distribution that is more extreme on the sides
- HighUp = the bigger diameter grains have a higher percentage distributed in an interval than the bigger ones
- HighLo = the smaller diameter grains have a higher percentage distributed in an interval than the bigger ones
- ExtremeUp = the bigger diameter grains have the highest percentage distributed in an interval; smaller diameters have minimal
- ExtremeLo = the smaller diameter grains have the highest percentage distributed in an interval; bigger diameters have minimal)

For the cases A, B, C they were based on the following:

- A, B, C (3_1) = based on HighLo_Bin3
- A, B, C (3_2) = based on ExtremeLo_Bin3
- A, B, C (4_1) = based on ExtremeLo_Bin4
- A, B, C (5_1) = based on HighLo_Bin5
- A, B, C (5_1) = based on ExtremeLo_Bin5
- A, B, C (6_1) = based on ExtremeLo_Bin6

- A, B, C (7_1) = based on HighLo_Bin7

Here is an example from the probe B16390, with the grains having a diameter between 63 and 125 μm. The example is for the case when the bin size is 4. The other cases for different bins have the same trend.

Original	Flat	Normal	ExtremeNor	Parabolic	ExtremePara

	HighUp	HighLo	ExtremeUp	ExtremeLo
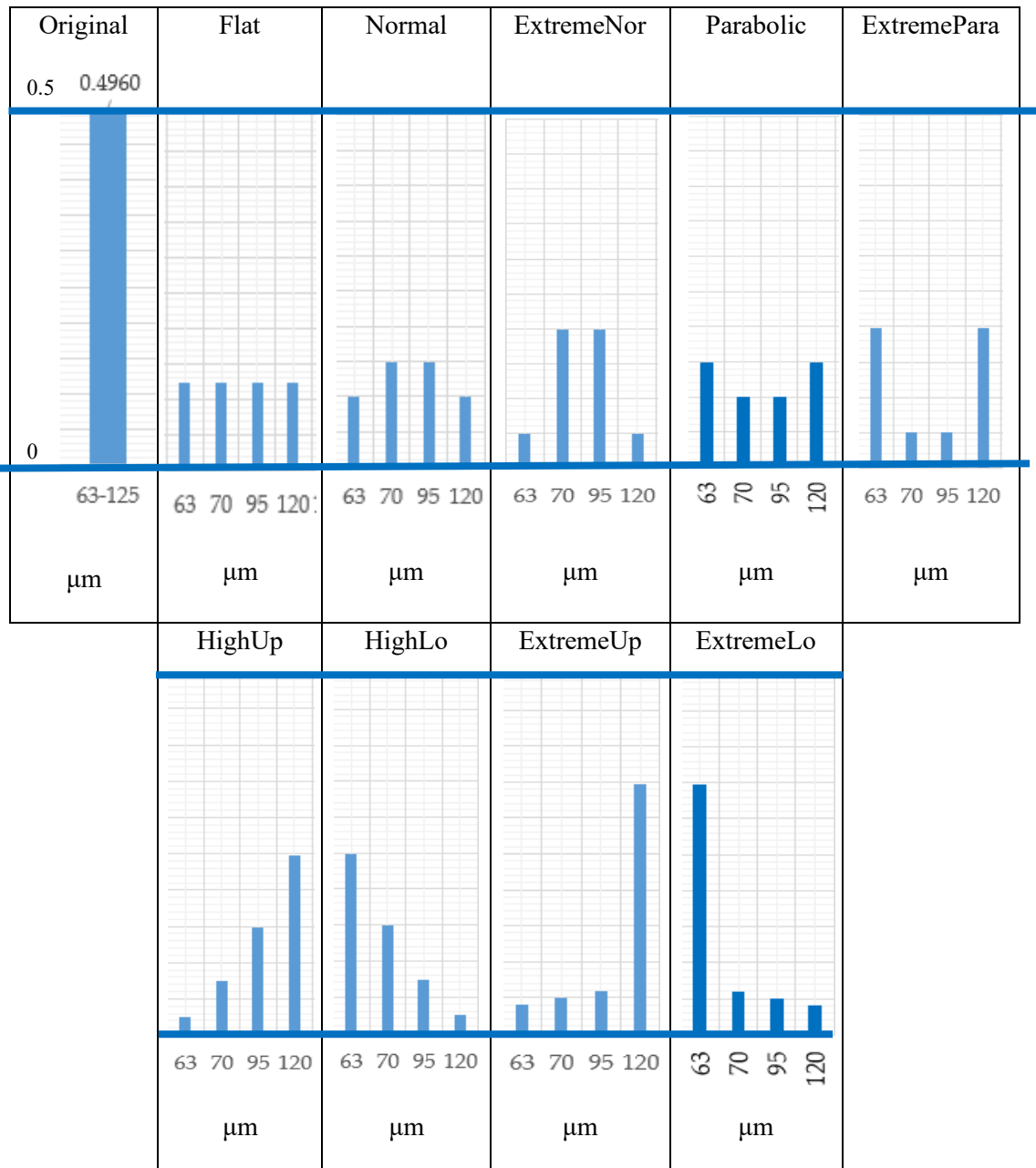
Simulations with spheres input data

The first and second column represents percentages. The third column represents the grain dimension in microns.

Flat_Bin2

0.10	0.0010	500
0.27	0.0027	400
0.27	0.0027	250
1.88	0.0188	175
1.88	0.0188	125
24.80	0.2480	100
24.80	0.2480	63
13.27	0.1327	50
13.27	0.1327	38
9.44	0.0944	30
9.44	0.0944	15
0.29	0.0029	13
0.29	0.0029	4
100.0000	1.0000	

HighUp_Bin2

param			
	0.10	0.0010	500
0.7	0.38	0.0038	400
0.3	0.16	0.0016	250
0.7	2.63	0.0263	175
0.3	1.13	0.0113	125
0.7	34.72	0.3472	100
0.3	14.88	0.1488	63
0.7	18.58	0.1858	50
0.3	7.96	0.0796	38
0.7	13.23	0.1323	30
0.3	5.67	0.0567	15
0.7	0.40	0.0040	13
0.3	0.17	0.0017	4
	100.0000	1.0000	

HighLo_Bin2

param			
	0.10	0.0010	500
0.3	0.16	0.0016	400
0.7	0.38	0.0038	250
0.3	1.13	0.0113	175
0.7	2.63	0.0263	125
0.3	14.88	0.1488	100
0.7	34.72	0.3472	63
0.3	7.96	0.0796	50
0.7	18.58	0.1858	38
0.3	5.67	0.0567	30
0.7	13.23	0.1323	15
0.3	0.17	0.0017	13
0.7	0.40	0.0040	4
	100.0000	1.0000	

ExtremeUp_Bin2

param			
	0.10	0.0010	500
0.95	0.51	0.0051	400
0.05	0.03	0.0003	250
0.95	3.56	0.0356	175
0.05	0.19	0.0019	125
0.95	47.12	0.4712	100
0.05	2.48	0.0248	63
0.95	25.21	0.2521	50
0.05	1.33	0.0133	38
0.95	17.96	0.1796	30
0.05	0.95	0.0095	15
0.95	0.54	0.0054	13
0.05	0.03	0.0003	4
	100.0000	1.0000	

ExtremeLo_Bin2

param			
	0.10	0.0010	500
0.05	0.03	0.0003	400
0.95	0.51	0.0051	250
0.05	0.19	0.0019	175
0.95	3.56	0.0356	125
0.05	2.48	0.0248	100
0.95	47.12	0.4712	63
0.05	1.33	0.0133	50
0.95	25.21	0.2521	38
0.05	0.95	0.0095	30
0.95	17.96	0.1796	15
0.05	0.03	0.0003	13
0.95	0.54	0.0054	4
	100.0000	1.0000	

Flat_Bin3

0.10	0.0010	500
0.18	0.0018	400
0.18	0.0018	300
0.18	0.0018	250
1.25	0.0125	225
1.25	0.0125	175
1.25	0.0125	125
16.53	0.1653	120
16.53	0.1653	90
16.53	0.1653	63
8.85	0.0885	60
8.85	0.0885	50
8.85	0.0885	38
6.30	0.0630	36
6.30	0.0630	22
6.30	0.0630	15
0.19	0.0019	12
0.19	0.0019	8
0.19	0.0019	4
100.00	1.0000	

Normal_Bin3

	0.10	0.0010	500
0.3	0.16	0.0016	400
0.4	0.22	0.0022	300
0.3	0.16	0.0016	250
0.3	1.13	0.0113	225
0.4	1.50	0.0150	175
0.3	1.13	0.0113	125
0.3	14.88	0.1488	120
0.4	19.84	0.1984	90
0.3	14.88	0.1488	63
0.3	7.96	0.0796	60
0.4	10.62	0.1062	50
0.3	7.96	0.0796	38
0.3	5.67	0.0567	36
0.4	7.56	0.0756	22
0.3	5.67	0.0567	15
0.3	0.17	0.0017	12
0.4	0.23	0.0023	8
0.3	0.17	0.0017	4
	100.00	1.0000	

ExtremeNor_Bin3

	0.10	0.0010	500
0.1	0.05	0.0005	400
0.8	0.43	0.0043	300
0.1	0.05	0.0005	250
0.1	0.38	0.0038	225
0.8	3.00	0.0300	175
0.1	0.38	0.0038	125
0.1	4.96	0.0496	120
0.8	39.68	0.3968	90
0.1	4.96	0.0496	63
0.1	2.65	0.0265	60
0.8	21.23	0.2123	50
0.1	2.65	0.0265	38
0.1	1.89	0.0189	36
0.8	15.12	0.1512	22
0.1	1.89	0.0189	15
0.1	0.06	0.0006	12
0.8	0.46	0.0046	8
0.1	0.06	0.0006	4
	100.00	1.0000	

HighUp_Bin3

	0.10	0.0010	500
0.5	0.27	0.0027	400
0.4	0.22	0.0022	300
0.1	0.05	0.0005	250
0.5	1.88	0.0188	225
0.4	1.50	0.0150	175
0.1	0.38	0.0038	125
0.5	24.80	0.2480	120
0.4	19.84	0.1984	90
0.1	4.96	0.0496	63
0.5	13.27	0.1327	60
0.4	10.62	0.1062	50
0.1	2.65	0.0265	38
0.5	9.45	0.0945	36
0.4	7.56	0.0756	22
0.1	1.89	0.0189	15
0.5	0.29	0.0029	12
0.4	0.23	0.0023	8
0.1	0.06	0.0006	4
	100.00	1.0000	

HighLo_Bin3

	0.10	0.0010	500
0.1	0.05	0.0005	400
0.4	0.22	0.0022	300
0.5	0.27	0.0027	250
0.1	0.38	0.0038	225
0.4	1.50	0.0150	175
0.5	1.88	0.0188	125
0.1	4.96	0.0496	120
0.4	19.84	0.1984	90
0.5	24.80	0.2480	63
0.1	2.65	0.0265	60
0.4	10.62	0.1062	50
0.5	13.27	0.1327	38
0.1	1.89	0.0189	36
0.4	7.56	0.0756	22
0.5	9.45	0.0945	15
0.1	0.06	0.0006	12
0.4	0.23	0.0023	8
0.5	0.29	0.0029	4
	100.00	1.0000	

ExtremeUp_Bin3

	0.10	0.0010	500
0.7	0.38	0.0038	400
0.2	0.11	0.0011	300
0.1	0.05	0.0005	250
0.7	2.63	0.0263	225
0.2	0.75	0.0075	175
0.1	0.38	0.0038	125
0.7	34.72	0.3472	120
0.2	9.92	0.0992	90
0.1	4.96	0.0496	63
0.7	18.58	0.1858	60
0.2	5.31	0.0531	50
0.1	2.65	0.0265	38
0.7	13.23	0.1323	36
0.2	3.78	0.0378	22
0.1	1.89	0.0189	15
0.7	0.40	0.0040	12
0.2	0.11	0.0011	8
0.1	0.06	0.0006	4
	100.00	1.0000	

ExtremeLo_Bin3

	0.10	0.0010	500
0.1	0.05	0.0005	400
0.2	0.11	0.0011	300
0.7	0.38	0.0038	250
0.1	0.38	0.0038	225
0.2	0.75	0.0075	175
0.7	2.63	0.0263	125
0.1	4.96	0.0496	120
0.2	9.92	0.0992	90
0.7	34.72	0.3472	63
0.1	2.65	0.0265	60
0.2	5.31	0.0531	50
0.7	18.58	0.1858	38
0.1	1.89	0.0189	36
0.2	3.78	0.0378	22
0.7	13.23	0.1323	15
0.1	0.06	0.0006	12
0.2	0.11	0.0011	8
0.7	0.40	0.0040	4
	100.00	1.0000	

Parabolic_Bin3

	0.10	0.0010	500
0.4	0.22	0.0022	400
0.2	0.11	0.0011	300
0.4	0.22	0.0022	250
0.4	1.50	0.0150	225
0.2	0.75	0.0075	175
0.4	1.50	0.0150	125
0.4	19.84	0.1984	120
0.2	9.92	0.0992	90
0.4	19.84	0.1984	63
0.4	10.62	0.1062	60
0.2	5.31	0.0531	50
0.4	10.62	0.1062	38
0.4	7.56	0.0756	36
0.2	3.78	0.0378	22
0.4	7.56	0.0756	15
0.4	0.23	0.0023	12
0.2	0.11	0.0011	8
0.4	0.23	0.0023	4
	100.00	1.0000	

Flat_Bin4

0.10	0.0010	500
0.135	0.0014	450
0.135	0.0014	400
0.135	0.0014	300
0.135	0.0014	250
0.9375	0.0094	240
0.9375	0.0094	200
0.9375	0.0094	160
2.625	0.0263	125
12.4	0.1240	120
12.4	0.1240	95
12.4	0.1240	70
12.4	0.1240	63
6.635	0.0664	62
6.635	0.0664	54
6.635	0.0664	46
6.635	0.0664	38
4.725	0.0473	34
4.725	0.0473	27
4.725	0.0473	20
4.725	0.0473	15
0.1425	0.0014	13
0.1425	0.0014	10
0.1425	0.0014	7
0.1425	0.0014	4
100.00	1.0000	

ExtremeNor_Bin4

	0.10	0.0010	500
0.1	0.054	0.0005	450
0.4	0.216	0.0022	400
0.4	0.216	0.0022	300
0.1	0.054	0.0005	250
0.1	0.375	0.0038	240
0.4	1.5	0.0150	200
0.4	1.5	0.0150	160
0.1	0.375	0.0038	125
0.1	4.96	0.0496	120
0.4	19.84	0.1984	95
0.4	19.84	0.1984	70
0.1	4.96	0.0496	63
0.1	2.654	0.0265	62
0.4	10.616	0.1062	54
0.4	10.616	0.1062	46
0.1	2.654	0.0265	38
0.1	1.89	0.0189	34
0.4	7.56	0.0756	27
0.4	7.56	0.0756	20
0.1	1.89	0.0189	15
0.1	0.057	0.0006	13
0.4	0.228	0.0023	10
0.4	0.228	0.0023	7
0.1	0.057	0.0006	4
	100.00	1.0000	

ExtremePara_Bin4

	0.10	0.0010	500
0.4	0.216	0.0022	450
0.1	0.054	0.0005	400
0.1	0.054	0.0005	300
0.4	0.216	0.0022	250
0.4	1.5	0.0150	240
0.1	0.375	0.0038	200
0.1	0.375	0.0038	160
0.4	1.5	0.0150	125
0.4	19.84	0.1984	120
0.1	4.96	0.0496	95
0.1	4.96	0.0496	70
0.4	19.84	0.1984	63
0.4	10.616	0.1062	62
0.1	2.654	0.0265	54
0.1	2.654	0.0265	46
0.4	10.616	0.1062	38
0.4	7.56	0.0756	34
0.1	1.89	0.0189	27
0.1	1.89	0.0189	20
0.4	7.56	0.0756	15
0.4	0.228	0.0023	13
0.1	0.057	0.0006	10
0.1	0.057	0.0006	7
0.4	0.228	0.0023	4
	100.00	1.0000	

Parabolic_Bin4

	0.10	0.0010	500
0.3	0.162	0.0016	450
0.2	0.108	0.0011	400
0.2	0.108	0.0011	300
0.3	0.162	0.0016	250
0.3	1.125	0.0113	240
0.2	0.75	0.0075	200
0.2	0.75	0.0075	160
0.3	1.125	0.0113	125
0.3	14.88	0.1488	120
0.2	9.92	0.0992	95
0.2	9.92	0.0992	70
0.3	14.88	0.1488	63
0.3	7.962	0.0796	62
0.2	5.308	0.0531	54
0.2	5.308	0.0531	46
0.3	7.962	0.0796	38
0.3	5.67	0.0567	34
0.2	3.78	0.0378	27
0.2	3.78	0.0378	20
0.3	5.67	0.0567	15
0.3	0.171	0.0017	13
0.2	0.114	0.0011	10
0.2	0.114	0.0011	7
0.3	0.171	0.0017	4
	100.00	1.0000	

Normal_Bin4

	0.10	0.0010	500
0.2	0.108	0.0011	450
0.3	0.162	0.0016	400
0.3	0.162	0.0016	300
0.2	0.108	0.0011	250
0.2	0.75	0.0075	240
0.3	1.125	0.0113	200
0.3	1.125	0.0113	160
0.2	0.75	0.0075	125
0.2	9.92	0.0992	120
0.3	14.88	0.1488	95
0.3	14.88	0.1488	70
0.2	9.92	0.0992	63
0.2	5.308	0.0531	62
0.3	7.962	0.0796	54
0.3	7.962	0.0796	46
0.2	5.308	0.0531	38
0.2	3.78	0.0378	34
0.3	5.67	0.0567	27
0.3	5.67	0.0567	20
0.2	3.78	0.0378	15
0.2	0.114	0.0011	13
0.3	0.171	0.0017	10
0.3	0.171	0.0017	7
0.2	0.114	0.0011	4
	100.00	1.0000	

HighUp_Bin4

	0.10	0.0010	500
0.5	0.27	0.0027	450
0.3	0.162	0.0016	400
0.2	0.081	0.0008	300
0.1	0.027	0.0003	250
0.5	1.875	0.0188	240
0.3	1.125	0.0113	200
0.2	0.5625	0.0056	160
0.1	0.375	0.0038	125
0.5	24.8	0.2480	120
0.3	14.88	0.1488	95
0.2	7.44	0.0744	70
0.1	2.48	0.0248	63
0.5	13.27	0.1327	62
0.3	7.962	0.0796	54
0.2	3.981	0.0398	46
0.1	1.327	0.0133	38
0.5	9.45	0.0945	34
0.3	5.67	0.0567	27
0.2	2.835	0.0284	20
0.1	0.945	0.0095	15
0.5	0.285	0.0029	13
0.3	0.171	0.0017	10
0.2	0.0855	0.0009	7
0.1	0.0285	0.0003	4
	100.00	1.0000	

HighLo_Bin4

	0.10	0.0010	500
0.1	0.027	0.0003	450
0.2	0.081	0.0008	400
0.3	0.162	0.0016	300
0.5	0.27	0.0027	250
0.1	0.1875	0.0019	240
0.2	0.5625	0.0056	200
0.3	1.125	0.0113	160
0.5	1.875	0.0188	125
0.1	2.48	0.0248	120
0.2	7.44	0.0744	95
0.3	14.88	0.1488	70
0.5	24.8	0.2480	63
0.1	1.327	0.0133	62
0.2	3.981	0.0398	54
0.3	7.962	0.0796	46
0.5	13.27	0.1327	38
0.1	0.945	0.0095	34
0.2	2.835	0.0284	27
0.3	5.67	0.0567	20
0.5	9.45	0.0945	15
0.1	0.0285	0.0003	13
0.2	0.0855	0.0009	10
0.3	0.171	0.0017	7
0.5	0.285	0.0029	4
	100.00	1.0000	

ExtremeUp_Bin4

	0.10	0.0010	500
0.7	0.378	0.0038	450
0.1	0.0648	0.0006	400
0.1	0.054	0.0005	300
0.1	0.0432	0.0004	250
0.7	2.625	0.0263	240
0.1	0.45	0.0045	200
0.1	0.375	0.0038	160
0.1	0.3	0.0030	125
0.7	34.72	0.3472	120
0.1	5.952	0.0595	95
0.1	4.96	0.0496	70
0.1	3.968	0.0397	63
0.7	18.578	0.1858	62
0.1	3.1848	0.0318	54
0.1	2.654	0.0265	46
0.1	2.1232	0.0212	38
0.7	13.23	0.1323	34
0.1	2.268	0.0227	27
0.1	1.89	0.0189	20
0.1	1.512	0.0151	15
0.7	0.399	0.0040	13
0.1	0.0684	0.0007	10
0.1	0.057	0.0006	7
0.1	0.0456	0.0005	4
	100.00	1.0000	

ExtremeLo_Bin4

	0.10	0.0010	500
0.1	0.0432	0.0004	450
0.1	0.054	0.0005	400
0.1	0.0648	0.0006	300
0.7	0.378	0.0038	250
0.1	0.3	0.0030	240
0.1	0.375	0.0038	200
0.1	0.45	0.0045	160
0.7	2.625	0.0263	125
0.1	3.968	0.0397	120
0.1	4.96	0.0496	95
0.1	5.952	0.0595	70
0.7	34.72	0.3472	63
0.1	2.1232	0.0212	62
0.1	2.654	0.0265	54
0.1	3.1848	0.0318	46
0.7	18.578	0.1858	38
0.1	1.512	0.0151	34
0.1	1.89	0.0189	27
0.1	2.268	0.0227	20
0.7	13.23	0.1323	15
0.1	0.0456	0.0005	13
0.1	0.057	0.0006	10
0.1	0.0684	0.0007	7
0.7	0.399	0.0040	4
	100.00	1.0000	

Flat_Bin5				Normal_Bin5				Parabolic_Bin5				HighLo_Bin5				HighUp_Bin5				ExtremeLo_Bin5				ExtremeUp_Bin5		
0.1000	0.0010	**500**		0.10	0.0010	**500**		0.10	0.0010	**500**		0.10	0.0010	**500**		0.10	0.0010	**500**		0.10	0.0010	**500**		0.10	0.0010	**500**
0.1080	0.0011	**450**	0.1	0.054	0.0005	**450**	0.32	0.1728	0.0017	**450**	0.05	0.027	0.0003	**450**	0.45	0.243	0.0024	**450**	0.05	0.027	0.0003	**450**	0.65	0.351	0.0035	**450**
0.1080	0.0011	**400**	0.2	0.108	0.0011	**400**	0.15	0.081	0.0008	**400**	0.1	0.054	0.0005	**400**	0.25	0.135	0.0014	**400**	0.07	0.0378	0.0004	**400**	0.13	0.0702	0.0007	**400**
0.1080	0.0011	**350**	0.4	0.216	0.0022	**350**	0.06	0.0324	0.0003	**350**	0.15	0.081	0.0008	**350**	0.15	0.081	0.0008	**350**	0.1	0.054	0.0005	**350**	0.1	0.054	0.0005	**350**
0.1080	0.0011	**300**	0.2	0.108	0.0011	**300**	0.15	0.081	0.0008	**300**	0.25	0.135	0.0014	**300**	0.1	0.054	0.0005	**300**	0.13	0.0702	0.0007	**300**	0.07	0.0378	0.0004	**300**
0.1080	0.0011	**250**	0.1	0.054	0.0005	**250**	0.32	0.1728	0.0017	**250**	0.45	0.243	0.0024	**250**	0.05	0.027	0.0003	**250**	0.65	0.351	0.0035	**250**	0.05	0.027	0.0003	**250**
0.7500	0.0075	**245**	0.1	0.375	0.0038	**245**	0.32	1.2	0.0120	**245**	0.05	0.1875	0.0019	**245**	0.45	1.6875	0.0169	**245**	0.05	0.1875	0.0019	**245**	0.65	2.4375	0.0244	**245**
0.7500	0.0075	**215**	0.2	0.75	0.0075	**215**	0.15	0.5625	0.0056	**215**	0.1	0.375	0.0038	**215**	0.25	0.9375	0.0094	**215**	0.07	0.2625	0.0026	**215**	0.13	0.4875	0.0049	**215**
0.7500	0.0075	**185**	0.4	1.5	0.0150	**185**	0.06	0.225	0.0023	**185**	0.15	0.5625	0.0056	**185**	0.15	0.5625	0.0056	**185**	0.1	0.375	0.0038	**185**	0.1	0.375	0.0038	**185**
0.7500	0.0075	**155**	0.2	0.75	0.0075	**155**	0.15	0.5625	0.0056	**155**	0.25	0.9375	0.0094	**155**	0.1	0.375	0.0038	**155**	0.13	0.4875	0.0049	**155**	0.07	0.2625	0.0026	**155**
0.7500	0.0075	**125**	0.1	0.375	0.0038	**125**	0.32	1.2	0.0120	**125**	0.45	1.6875	0.0169	**125**	0.05	0.1875	0.0019	**125**	0.65	2.4375	0.0244	**125**	0.05	0.1875	0.0019	**125**
9.9200	0.0992	**124**	0.1	4.96	0.0496	**124**	0.32	15.872	0.1587	**124**	0.05	2.48	0.0248	**124**	0.45	22.32	0.2232	**124**	0.05	2.48	0.0248	**124**	0.65	32.24	0.3224	**124**
9.9200	0.0992	**105**	0.2	9.92	0.0992	**105**	0.15	7.44	0.0744	**105**	0.1	4.96	0.0496	**105**	0.25	12.4	0.1240	**105**	0.07	3.472	0.0347	**105**	0.13	6.448	0.0645	**105**
9.9200	0.0992	**90**	0.4	19.84	0.1984	**90**	0.06	2.976	0.0298	**90**	0.15	7.44	0.0744	**90**	0.15	7.44	0.0744	**90**	0.1	4.96	0.0496	**90**	0.1	4.96	0.0496	**90**
9.9200	0.0992	**75**	0.2	9.92	0.0992	**75**	0.15	7.44	0.0744	**75**	0.25	12.4	0.1240	**75**	0.1	4.96	0.0496	**75**	0.13	6.448	0.0645	**75**	0.07	3.472	0.0347	**75**
9.9200	0.0992	**63**	0.1	4.96	0.0496	**63**	0.32	15.872	0.1587	**63**	0.45	22.32	0.2232	**63**	0.05	2.48	0.0248	**63**	0.65	32.24	0.3224	**63**	0.05	2.48	0.0248	**63**
5.3080	0.0531	**62**	0.1	2.654	0.0265	**62**	0.32	8.4928	0.0849	**62**	0.05	1.327	0.0133	**62**	0.45	11.943	0.1194	**62**	0.05	1.327	0.0133	**62**	0.65	17.251	0.1725	**62**
5.3080	0.0531	**56**	0.2	5.308	0.0531	**56**	0.15	3.981	0.0398	**56**	0.1	2.654	0.0265	**56**	0.25	6.635	0.0664	**56**	0.07	1.8578	0.0186	**56**	0.13	3.4502	0.0345	**56**
5.3080	0.0531	**50**	0.4	10.616	0.1062	**50**	0.06	1.5924	0.0159	**50**	0.15	3.981	0.0398	**50**	0.15	3.981	0.0398	**50**	0.1	2.654	0.0265	**50**	0.1	2.654	0.0265	**50**
5.3080	0.0531	**44**	0.2	5.308	0.0531	**44**	0.15	3.981	0.0398	**44**	0.25	6.635	0.0664	**44**	0.1	2.654	0.0265	**44**	0.13	3.4502	0.0345	**44**	0.07	1.8578	0.0186	**44**
5.3080	0.0531	**38**	0.1	2.654	0.0265	**38**	0.32	8.4928	0.0849	**38**	0.45	11.943	0.1194	**38**	0.05	1.327	0.0133	**38**	0.65	17.251	0.1725	**38**	0.05	1.327	0.0133	**38**
3.7800	0.0378	**35**	0.1	1.89	0.0189	**35**	0.32	6.048	0.0605	**35**	0.05	0.945	0.0095	**35**	0.45	8.505	0.0851	**35**	0.05	0.945	0.0095	**35**	0.65	12.285	0.1229	**35**
3.7800	0.0378	**31**	0.2	3.78	0.0378	**31**	0.15	2.835	0.0284	**31**	0.1	1.89	0.0189	**31**	0.25	4.725	0.0473	**31**	0.07	1.323	0.0132	**31**	0.13	2.457	0.0246	**31**
3.7800	0.0378	**25**	0.4	7.56	0.0756	**25**	0.06	1.134	0.0113	**25**	0.15	2.835	0.0284	**25**	0.15	2.835	0.0284	**25**	0.1	1.89	0.0189	**25**	0.1	1.89	0.0189	**25**
3.7800	0.0378	**20**	0.2	3.78	0.0378	**20**	0.15	2.835	0.0284	**20**	0.25	4.725	0.0473	**20**	0.1	1.89	0.0189	**20**	0.13	2.457	0.0246	**20**	0.07	1.323	0.0132	**20**
3.7800	0.0378	**15**	0.1	1.89	0.0189	**15**	0.32	6.048	0.0605	**15**	0.45	8.505	0.0851	**15**	0.05	0.945	0.0095	**15**	0.65	12.285	0.1229	**15**	0.05	0.945	0.0095	**15**
0.1140	0.0011	**12**	0.1	0.057	0.0006	**12**	0.32	0.1824	0.0018	**12**	0.05	0.0285	0.0003	**12**	0.45	0.2565	0.0026	**12**	0.05	0.0285	0.0003	**12**	0.65	0.3705	0.0037	**12**
0.1140	0.0011	**10**	0.2	0.114	0.0011	**10**	0.15	0.0855	0.0009	**10**	0.1	0.057	0.0006	**10**	0.25	0.1425	0.0014	**10**	0.07	0.0399	0.0004	**10**	0.13	0.0741	0.0007	**10**
0.1140	0.0011	**8**	0.4	0.228	0.0023	**8**	0.06	0.0342	0.0003	**8**	0.15	0.0855	0.0009	**8**	0.15	0.0855	0.0009	**8**	0.1	0.057	0.0006	**8**	0.1	0.057	0.0006	**8**
0.1140	0.0011	**6**	0.2	0.114	0.0011	**6**	0.15	0.0855	0.0009	**6**	0.25	0.1425	0.0014	**6**	0.1	0.057	0.0006	**6**	0.13	0.0741	0.0007	**6**	0.07	0.0399	0.0004	**6**
0.1140	0.0011	**4**	0.1	0.057	0.0006	**4**	0.32	0.1824	0.0018	**4**	0.45	0.2565	0.0026	**4**	0.05	0.0285	0.0003	**4**	0.65	0.3705	0.0037	**4**	0.05	0.0285	0.0003	**4**
100.00	1.0000			100.00	1.0000			100.00	1.0000			100.00	1.0000			100.00	1.0000			100.00	1.0000			100.00	1.0000	

Flat_Bin6

	0.10	0.0010	500
0.54	0.0900	0.0009	455
	0.0900	0.0009	414
	0.0900	0.0009	373
	0.0900	0.0009	332
	0.0900	0.0009	291
	0.0900	0.0009	250
3.75	0.6250	0.0063	235
	0.6250	0.0063	215
	0.6250	0.0063	195
	0.6250	0.0063	175
	0.6250	0.0063	150
	0.6250	0.0063	125
49.6	8.2667	0.0827	113
	8.2667	0.0827	103
	8.2667	0.0827	93
	8.2667	0.0827	83
	8.2667	0.0827	73
	8.2667	0.0827	63
26.54	4.4233	0.0442	62
	4.4233	0.0442	58
	4.4233	0.0442	53
	4.4233	0.0442	48
	4.4233	0.0442	43
	4.4233	0.0442	38
18.9	3.1500	0.0315	35
	3.1500	0.0315	31
	3.1500	0.0315	27
	3.1500	0.0315	23
	3.1500	0.0315	19
	3.1500	0.0315	15
0.57	0.0950	0.0010	14
	0.0950	0.0010	12
	0.0950	0.0010	10
	0.0950	0.0010	8
	0.0950	0.0010	6
	0.0950	0.0010	4
	100.00	1.0000	

Normal_Bin6

	0.10	0.0010	500
0.05	0.027	0.0003	455
0.1	0.054	0.0005	414
0.35	0.189	0.0019	373
0.35	0.189	0.0019	332
0.1	0.054	0.0005	291
0.05	0.027	0.0003	250
0.05	0.1875	0.0019	235
0.1	0.375	0.0038	215
0.35	1.3125	0.0131	195
0.35	1.3125	0.0131	175
0.1	0.375	0.0038	150
0.05	0.1875	0.0019	125
0.05	2.48	0.0248	113
0.1	4.96	0.0496	103
0.35	17.36	0.1736	93
0.35	17.36	0.1736	83
0.1	4.96	0.0496	73
0.05	2.48	0.0248	63
0.05	1.327	0.0133	62
0.1	2.654	0.0265	58
0.35	9.289	0.0929	53
0.35	9.289	0.0929	48
0.1	2.654	0.0265	43
0.05	1.327	0.0133	38
0.05	0.945	0.0095	35
0.1	1.89	0.0189	31
0.35	6.615	0.0662	27
0.35	6.615	0.0662	23
0.1	1.89	0.0189	19
0.05	0.945	0.0095	15
0.05	0.0285	0.0003	14
0.1	0.057	0.0006	12
0.35	0.1995	0.0020	10
0.35	0.1995	0.0020	8
0.1	0.057	0.0006	6
0.05	0.0285	0.0003	4
	100.00	1.0000	

Parabolic_Bin6

	0.10	0.0010	500
0.35	0.189	0.0019	455
0.1	0.054	0.0005	414
0.05	0.027	0.0003	373
0.05	0.027	0.0003	332
0.1	0.054	0.0005	291
0.35	0.189	0.0019	250
0.35	1.3125	0.0131	235
0.1	0.375	0.0038	215
0.05	0.1875	0.0019	195
0.05	0.1875	0.0019	175
0.1	0.375	0.0038	150
0.35	1.3125	0.0131	125
0.35	17.36	0.1736	113
0.1	4.96	0.0496	103
0.05	2.48	0.0248	93
0.05	2.48	0.0248	83
0.1	4.96	0.0496	73
0.35	17.36	0.1736	63
0.35	9.289	0.0929	62
0.1	2.654	0.0265	58
0.05	1.327	0.0133	53
0.05	1.327	0.0133	48
0.1	2.654	0.0265	43
0.35	9.289	0.0929	38
0.35	6.615	0.0662	35
0.1	1.89	0.0189	31
0.05	0.945	0.0095	27
0.05	0.945	0.0095	23
0.1	1.89	0.0189	19
0.35	6.615	0.0662	15
0.35	0.1995	0.0020	14
0.1	0.057	0.0006	12
0.05	0.0285	0.0003	10
0.05	0.0285	0.0003	8
0.1	0.057	0.0006	6
0.35	0.1995	0.0020	4
	100.00	1.0000	

HighUp_Bin6

	0.10	0.0010	500
0.5	0.27	0.0027	455
0.15	0.081	0.0008	414
0.13	0.0702	0.0007	373
0.1	0.054	0.0005	332
0.07	0.0378	0.0004	291
0.05	0.027	0.0003	250
0.5	1.875	0.0188	235
0.15	0.5625	0.0056	215
0.13	0.4875	0.0049	195
0.1	0.375	0.0038	175
0.07	0.2625	0.0026	150
0.05	0.1875	0.0019	125
0.5	24.8	0.2480	113
0.15	7.44	0.0744	103
0.13	6.448	0.0645	93
0.1	4.96	0.0496	83
0.07	3.472	0.0347	73
0.05	2.48	0.0248	63
0.5	13.27	0.1327	62
0.15	3.981	0.0398	58
0.13	3.4502	0.0345	53
0.1	2.654	0.0265	48
0.07	1.8578	0.0186	43
0.05	1.327	0.0133	38
0.5	9.45	0.0945	35
0.15	2.835	0.0284	31
0.13	2.457	0.0246	27
0.1	1.89	0.0189	23
0.07	1.323	0.0132	19
0.05	0.945	0.0095	15
0.5	0.285	0.0029	14
0.15	0.0855	0.0009	12
0.13	0.0741	0.0007	10
0.1	0.057	0.0006	8
0.07	0.0399	0.0004	6
0.05	0.0285	0.0003	4
	100.00	1.0000	

HighLo_Bin6

	0.10	0.0010	500
0.05	0.027	0.0003	455
0.07	0.0378	0.0004	414
0.1	0.054	0.0005	373
0.13	0.0702	0.0007	332
0.15	0.081	0.0008	291
0.5	0.27	0.0027	250
0.05	0.1875	0.0019	235
0.07	0.2625	0.0026	215
0.1	0.375	0.0038	195
0.13	0.4875	0.0049	175
0.15	0.5625	0.0056	150
0.5	1.875	0.0188	125
0.05	2.48	0.0248	113
0.07	3.472	0.0347	103
0.1	4.96	0.0496	93
0.13	6.448	0.0645	83
0.15	7.44	0.0744	73
0.5	24.8	0.2480	63
0.05	1.327	0.0133	62
0.07	1.8578	0.0186	58
0.1	2.654	0.0265	53
0.13	3.4502	0.0345	48
0.15	3.981	0.0398	43
0.5	13.27	0.1327	38
0.05	0.945	0.0095	35
0.07	1.323	0.0132	31
0.1	1.89	0.0189	27
0.13	2.457	0.0246	23
0.15	2.835	0.0284	19
0.5	9.45	0.0945	15
0.05	0.0285	0.0003	14
0.07	0.0399	0.0004	12
0.1	0.057	0.0006	10
0.13	0.0741	0.0007	8
0.15	0.0855	0.0009	6
0.5	0.285	0.0029	4
	100.00	1.0000	

ExtremeLo_Bin6

	0.10	0.0010	500
0.02	0.0108	0.0001	455
0.05	0.027	0.0003	414
0.07	0.0378	0.0004	373
0.1	0.054	0.0005	332
0.13	0.0702	0.0007	291
0.63	0.3402	0.0034	250
0.02	0.075	0.0008	235
0.05	0.1875	0.0019	215
0.07	0.2625	0.0026	195
0.1	0.375	0.0038	175
0.13	0.4875	0.0049	150
0.63	2.3625	0.0236	125
0.02	0.992	0.0099	113
0.05	2.48	0.0248	103
0.07	3.472	0.0347	93
0.1	4.96	0.0496	83
0.13	6.448	0.0645	73
0.63	31.248	0.3125	63
0.02	0.5308	0.0053	62
0.05	1.327	0.0133	56
0.07	1.8578	0.0186	50
0.1	2.654	0.0265	46
0.13	3.4502	0.0345	42
0.63	16.72	0.1672	38
0.02	0.378	0.0038	35
0.05	0.945	0.0095	31
0.07	1.323	0.0132	27
0.1	1.89	0.0189	23
0.13	2.457	0.0246	19
0.63	11.907	0.1191	15
0.02	0.0114	0.0001	14
0.05	0.0285	0.0003	12
0.07	0.0399	0.0004	10
0.1	0.057	0.0006	8
0.13	0.0741	0.0007	6
0.63	0.3591	0.0036	4
	100.00	1.0000	

ExtremeUp_Bin6

	0.10	0.0010	500
0.63	0.3402	0.0034	455
0.13	0.0702	0.0007	414
0.1	0.054	0.0005	373
0.07	0.0378	0.0004	332
0.05	0.027	0.0003	291
0.02	0.0108	0.0001	250
0.63	2.3625	0.0236	235
0.13	0.4875	0.0049	215
0.1	0.375	0.0038	195
0.07	0.2625	0.0026	175
0.05	0.1875	0.0019	150
0.02	0.075	0.0008	125
0.63	31.248	0.3125	113
0.13	6.448	0.0645	103
0.1	4.96	0.0496	93
0.07	3.472	0.0347	83
0.05	2.48	0.0248	73
0.02	0.992	0.0099	63
0.63	16.72	0.1672	62
0.13	3.4502	0.0345	56
0.1	2.654	0.0265	50
0.07	1.8578	0.0186	46
0.05	1.327	0.0133	42
0.02	0.5308	0.0053	38
0.63	11.907	0.1191	35
0.13	2.457	0.0246	31
0.1	1.89	0.0189	27
0.07	1.323	0.0132	23
0.05	0.945	0.0095	19
0.02	0.378	0.0038	15
0.63	0.3591	0.0036	14
0.13	0.0741	0.0007	12
0.1	0.057	0.0006	10
0.07	0.0399	0.0004	8
0.05	0.0285	0.0003	6
0.02	0.0114	0.0001	4
	100.00	1.0000	

Flat_Bin7			Normal_Bin7				Parabolic_Bin7				HighUp_Bin7				HighLo_Bin7			
0.10000	0.0010	**500**		0.10000	0.0010	**500**		0.10000	0.0010	**500**		0.10000	0.0010	**500**		0.10000	0.0010	**500**
0.07714	0.0008	**450**	0.03	0.0162	0.0002	**450**	0.27	0.1458	0.0015	**450**	0.5	0.27	0.0027	**450**	0.02	0.0108	0.0001	**450**
0.07714	0.0008	**415**	0.07	0.0378	0.0004	**415**	0.15	0.081	0.0008	**415**	0.15	0.081	0.0008	**415**	0.03	0.0162	0.0002	**415**
0.07714	0.0008	**380**	0.15	0.081	0.0008	**380**	0.07	0.0378	0.0004	**380**	0.13	0.0702	0.0007	**380**	0.07	0.0378	0.0004	**380**
0.07714	0.0008	**345**	0.5	0.27	0.0027	**345**	0.02	0.0108	0.0001	**345**	0.1	0.054	0.0005	**345**	0.1	0.054	0.0005	**345**
0.07714	0.0008	**310**	0.15	0.081	0.0008	**310**	0.07	0.0378	0.0004	**310**	0.07	0.0378	0.0004	**310**	0.13	0.0702	0.0007	**310**
0.07714	0.0008	**285**	0.07	0.0378	0.0004	**285**	0.15	0.081	0.0008	**285**	0.03	0.0162	0.0002	**285**	0.15	0.081	0.0008	**285**
0.07714	0.0002	**250**	0.03	0.0162	0.0002	**250**	0.27	0.1458	0.0015	**250**	0.02	0.0108	0.0001	**250**	0.5	0.27	0.0027	**250**
0.53571	0.0054	**233**	0.03	0.1125	0.0011	**233**	0.27	1.0125	0.0101	**233**	0.5	1.875	0.0188	**233**	0.02	0.075	0.0008	**233**
0.53571	0.0054	**215**	0.07	0.2625	0.0026	**215**	0.15	0.5625	0.0056	**215**	0.15	0.5625	0.0056	**215**	0.03	0.1125	0.0011	**215**
0.53571	0.0054	**197**	0.15	0.5625	0.0056	**197**	0.07	0.2625	0.0026	**197**	0.13	0.4875	0.0049	**197**	0.07	0.2625	0.0026	**197**
0.53571	0.0054	**179**	0.5	1.875	0.0188	**179**	0.02	0.075	0.0008	**179**	0.1	0.375	0.0038	**179**	0.1	0.375	0.0038	**179**
0.53571	0.0054	**161**	0.15	0.5625	0.0056	**161**	0.07	0.2625	0.0026	**161**	0.07	0.2625	0.0026	**161**	0.13	0.4875	0.0049	**161**
0.53571	0.0054	**143**	0.07	0.2625	0.0026	**143**	0.15	0.5625	0.0056	**143**	0.03	0.1125	0.0011	**143**	0.15	0.5625	0.0056	**143**
0.53571	0.0054	**125**	0.03	0.1125	0.0011	**125**	0.27	1.0125	0.0101	**125**	0.02	0.075	0.0008	**125**	0.5	1.875	0.0188	**125**
7.08571	0.0709	**117**	0.03	1.488	0.0149	**117**	0.27	13.392	0.1339	**117**	0.5	24.8	0.2480	**117**	0.02	0.992	0.0099	**117**
7.08571	0.0709	**108**	0.07	3.472	0.0347	**108**	0.15	7.44	0.0744	**108**	0.15	7.44	0.0744	**108**	0.03	1.488	0.0149	**108**
7.08571	0.0709	**99**	0.15	7.44	0.0744	**99**	0.07	3.472	0.0347	**99**	0.13	6.448	0.0645	**99**	0.07	3.472	0.0347	**99**
7.08571	0.0709	**90**	0.5	24.8	0.2480	**90**	0.02	0.992	0.0099	**90**	0.1	4.96	0.0496	**90**	0.1	4.96	0.0496	**90**
7.08571	0.0709	**81**	0.15	7.44	0.0744	**81**	0.07	3.472	0.0347	**81**	0.07	3.472	0.0347	**81**	0.13	6.448	0.0645	**81**
7.08571	0.0709	**72**	0.07	3.472	0.0347	**72**	0.15	7.44	0.0744	**72**	0.03	1.488	0.0149	**72**	0.15	7.44	0.0744	**72**
7.08571	0.0709	**63**	0.03	1.488	0.0149	**63**	0.27	13.392	0.1339	**63**	0.02	0.992	0.0099	**63**	0.5	24.8	0.2480	**63**
3.79143	0.0379	**62**	0.03	0.7962	0.0080	**62**	0.27	7.1658	0.0717	**62**	0.5	13.27	0.1327	**62**	0.02	0.5308	0.0053	**62**
3.79143	0.0379	**58**	0.07	1.8578	0.0186	**58**	0.15	3.981	0.0398	**58**	0.15	3.981	0.0398	**58**	0.03	0.7962	0.0080	**58**
3.79143	0.0379	**54**	0.15	3.981	0.0398	**54**	0.07	1.8578	0.0186	**54**	0.13	3.4502	0.0345	**54**	0.07	1.8578	0.0186	**54**
3.79143	0.0379	**50**	0.5	13.27	0.1327	**50**	0.02	0.5308	0.0053	**50**	0.1	2.654	0.0265	**50**	0.1	2.654	0.0265	**50**
3.79143	0.0379	**46**	0.15	3.981	0.0398	**46**	0.07	1.8578	0.0186	**46**	0.07	1.8578	0.0186	**46**	0.13	3.4502	0.0345	**46**
3.79143	0.0379	**42**	0.07	1.8578	0.0186	**42**	0.15	3.981	0.0398	**42**	0.03	0.7962	0.0080	**42**	0.15	3.981	0.0398	**42**
3.79143	0.0379	**38**	0.03	0.7962	0.0080	**38**	0.27	7.1658	0.0717	**38**	0.02	0.5308	0.0053	**38**	0.5	13.27	0.1327	**38**
2.70000	0.0270	**33**	0.03	0.567	0.0057	**33**	0.27	5.103	0.0510	**33**	0.5	9.45	0.0945	**33**	0.02	0.378	0.0038	**33**
2.70000	0.0270	**30**	0.07	1.323	0.0132	**30**	0.15	2.835	0.0284	**30**	0.15	2.835	0.0284	**30**	0.03	0.567	0.0057	**30**
2.70000	0.0270	**27**	0.15	2.835	0.0284	**27**	0.07	1.323	0.0132	**27**	0.13	2.457	0.0246	**27**	0.07	1.323	0.0132	**27**
2.70000	0.0270	**24**	0.5	9.45	0.0945	**24**	0.02	0.378	0.0038	**24**	0.1	1.89	0.0189	**24**	0.1	1.89	0.0189	**24**
2.70000	0.0270	**21**	0.15	2.835	0.0284	**21**	0.07	1.323	0.0132	**21**	0.07	1.323	0.0132	**21**	0.13	2.457	0.0246	**21**
2.70000	0.0270	**18**	0.07	1.323	0.0132	**18**	0.15	2.835	0.0284	**18**	0.03	0.567	0.0057	**18**	0.15	2.835	0.0284	**18**
2.70000	0.0270	**15**	0.03	0.567	0.0057	**15**	0.27	5.103	0.0510	**15**	0.02	0.378	0.0038	**15**	0.5	9.45	0.0945	**15**
0.08143	0.0008	**14**	0.03	0.0171	0.0002	**14**	0.27	0.1539	0.0015	**14**	0.5	0.285	0.0029	**14**	0.02	0.0114	0.0001	**14**
0.08143	0.0008	**12.5**	0.07	0.0399	0.0004	**12.5**	0.15	0.0855	0.0009	**12.5**	0.15	0.0855	0.0009	**12.5**	0.03	0.0171	0.0002	**12.5**
0.08143	0.0008	**11**	0.15	0.0855	0.0009	**11**	0.07	0.0399	0.0004	**11**	0.13	0.0741	0.0007	**11**	0.07	0.0399	0.0004	**11**
0.08143	0.0008	**9.5**	0.5	0.285	0.0029	**9.5**	0.02	0.0114	0.0001	**9.5**	0.1	0.057	0.0006	**9.5**	0.1	0.057	0.0006	**9.5**
0.08143	0.0008	**7**	0.15	0.0855	0.0009	**7**	0.07	0.0399	0.0004	**7**	0.07	0.0399	0.0004	**7**	0.13	0.0741	0.0007	**7**
0.08143	0.0008	**5.5**	0.07	0.0399	0.0004	**5.5**	0.15	0.0855	0.0009	**5.5**	0.03	0.0171	0.0002	**5.5**	0.15	0.0855	0.0009	**5.5**
0.08143	0.0008	**4**	0.03	0.0171	0.0002	**4**	0.27	0.1539	0.0015	**4**	0.02	0.0114	0.0001	**4**	0.5	0.285	0.0029	**4**
100.00	1.0000			100.00	1.0000			100.00	1.0000			100.00	1.0000			100.00	1.0000	

Simulations varying only below 38 μm (Case A)

A3_1

	0.1000	0.0010	500
	0.5400	0.0054	250
	3.7500	0.0375	125
	49.6000	0.4960	63
	26.5400	0.2654	38
0.1	1.89	0.0189	36
0.4	7.56	0.0756	22
0.5	9.45	0.0945	15
0.1	0.06	0.0006	12
0.4	0.23	0.0023	8
0.5	0.29	0.0029	4
	100.0000	1.0000	

A3_2

	0.1000	0.0010	500
	0.5400	0.0054	250
	3.7500	0.0375	125
	49.6000	0.4960	63
	26.5400	0.2654	38
0.1	1.89	0.0189	36
0.2	3.78	0.0378	22
0.7	13.23	0.1323	15
0.1	0.06	0.0006	12
0.2	0.11	0.0011	8
0.7	0.40	0.0040	4
	100.0000	1.0000	

A4_1

	0.1000	0.0010	500
	0.5400	0.0054	250
	3.7500	0.0375	125
	49.6000	0.4960	63
	26.5400	0.2654	38
0.08	1.512	0.0151	34
0.1	1.89	0.0189	27
0.12	2.268	0.0227	20
0.7	13.23	0.1323	15
0.08	0.0456	0.0005	13
0.1	0.057	0.0006	10
0.12	0.0684	0.0007	7
0.7	0.399	0.0040	4
	100.00	1.0000	

A5_1

	0.1000	0.0010	500
	0.5400	0.0054	250
	3.7500	0.0375	125
	49.6000	0.4960	63
	26.5400	0.2654	38
0.05	0.945	0.0095	35
0.1	1.89	0.0189	31
0.15	2.835	0.0284	25
0.25	4.725	0.0473	20
0.45	8.505	0.0851	15
0.05	0.0285	0.0003	12
0.1	0.057	0.0006	10
0.15	0.0855	0.0009	8
0.25	0.1425	0.0014	6
0.45	0.2565	0.0026	4

A5_2

	0.1000	0.0010	500
	0.5400	0.0054	250
	3.7500	0.0375	125
	49.6000	0.4960	63
	26.5400	0.2654	38
0.05	0.945	0.0095	35
0.07	1.323	0.0132	31
0.1	1.89	0.0189	25
0.13	2.457	0.0246	20
0.65	12.285	0.1229	15
0.05	0.0285	0.0003	12
0.07	0.0399	0.0004	10
0.1	0.057	0.0006	8
0.13	0.0741	0.0007	6
0.65	0.3705	0.0037	4

A6_1

	0.1000	0.0010	500
	0.5400	0.0054	250
	3.7500	0.0375	125
	49.6000	0.4960	63
	26.5400	0.2654	38
0.02	0.378	0.0038	35
0.05	0.945	0.0095	31
0.07	1.323	0.0132	27
0.1	1.89	0.0189	23
0.13	2.457	0.0246	19
0.63	11.907	0.1191	15
0.02	0.0114	0.0001	14
0.05	0.0285	0.0003	12
0.07	0.0399	0.0004	10
0.1	0.057	0.0006	8
0.13	0.0741	0.0007	6
0.63	0.3591	0.0036	4
	100.00	1.0000	

A7_1

	0.1000	0.0010	500
	0.5400	0.0054	250
	3.7500	0.0375	125
	49.6000	0.4960	63
	26.5400	0.2654	38
0.02	0.378	0.0038	33
0.03	0.567	0.0057	30
0.07	1.323	0.0132	27
0.1	1.89	0.0189	24
0.13	2.457	0.0246	21
0.15	2.835	0.0284	18
0.5	9.45	0.0945	15
0.02	0.0114	0.0001	14
0.03	0.0171	0.0002	12.5
0.07	0.0399	0.0004	11
0.1	0.057	0.0006	9.5
0.13	0.0741	0.0007	7
0.15	0.0855	0.0009	5.5
0.5	0.285	0.0029	4
	100.00	1.0000	

Simulations varying only below 63 µm (Case B)

B3_1

	0.1000	0.0010	500
	0.5400	0.0054	250
	3.7500	0.0375	125
	49.6000	0.4960	63
0.1	2.65	0.0265	60
0.4	10.62	0.1062	50
0.5	13.27	0.1327	38
0.1	1.89	0.0189	36
0.4	7.56	0.0756	22
0.5	9.45	0.0945	15
0.1	0.06	0.0006	12
0.4	0.23	0.0023	8
0.5	0.29	0.0029	4
	100.0000	1.0000	

B3_2

	0.1000	0.0010	500
	0.5400	0.0054	250
	3.7500	0.0375	125
	49.6000	0.4960	63
0.1	2.65	0.0265	60
0.2	5.31	0.0531	50
0.7	18.58	0.1858	38
0.1	1.89	0.0189	36
0.2	3.78	0.0378	22
0.7	13.23	0.1323	15
0.1	0.06	0.0006	12
0.2	0.11	0.0011	8
0.7	0.40	0.0040	4
	100.0000	1.0000	

B4_1

	0.1000	0.0010	500
	0.5400	0.0054	250
	3.7500	0.0375	125
	49.6000	0.4960	63
0.08	2.1232	0.0212	62
0.1	2.654	0.0265	54
0.12	3.1848	0.0318	46
0.7	18.578	0.1858	38
0.08	1.512	0.0151	34
0.1	1.89	0.0189	27
0.12	2.268	0.0227	20
0.7	13.23	0.1323	15
0.08	0.0456	0.0005	13
0.1	0.057	0.0006	10
0.12	0.0684	0.0007	7
0.7	0.399	0.0040	4
	100.0000	1.0000	

B5_1

	0.1000	0.0010	500
	0.5400	0.0054	250
	3.7500	0.0375	125
	49.6000	0.4960	63
0.05	1.327	0.0133	62
0.1	2.654	0.0265	56
0.15	3.981	0.0398	50
0.25	6.635	0.0664	44
0.45	11.943	0.1194	38
0.05	0.945	0.0095	35
0.1	1.89	0.0189	31
0.15	2.835	0.0284	25
0.25	4.725	0.0473	20
0.45	8.505	0.0851	15
0.05	0.0285	0.0003	12
0.1	0.057	0.0006	10
0.15	0.0855	0.0009	8
0.25	0.1425	0.0014	6
0.45	0.2565	0.0026	4
	100.0000	1.0000	

B5_2

	0.1000	0.0010	500
	0.5400	0.0054	250
	3.7500	0.0375	125
	49.6000	0.4960	63
0.05	1.327	0.0133	62
0.07	1.8578	0.0186	56
0.1	2.654	0.0265	50
0.13	3.4502	0.0345	44
0.65	17.251	0.1725	38
0.05	0.945	0.0095	35
0.07	1.323	0.0132	31
0.1	1.89	0.0189	25
0.13	2.457	0.0246	20
0.65	12.285	0.1229	15
0.05	0.0285	0.0003	12
0.07	0.0399	0.0004	10
0.1	0.057	0.0006	8
0.13	0.0741	0.0007	6
0.65	0.3705	0.0037	4
	100.0000	1.0000	

B6_1

	0.1000	0.0010	500
	0.5400	0.0054	250
	3.7500	0.0375	125
	49.6000	0.4960	63
0.02	0.5308	0.0053	62
0.05	1.327	0.0133	56
0.07	1.8578	0.0186	50
0.1	2.654	0.0265	46
0.13	3.4502	0.0345	42
0.63	16.7202	0.1672	38
0.02	0.378	0.0038	35
0.05	0.945	0.0095	31
0.07	1.323	0.0132	27
0.1	1.89	0.0189	23
0.13	2.457	0.0246	19
0.63	11.907	0.1191	15
0.02	0.0114	0.0001	14
0.05	0.0285	0.0003	12
0.07	0.0399	0.0004	10
0.1	0.057	0.0006	8
0.13	0.0741	0.0007	6
0.63	0.3591	0.0036	4
	100.0000	1.0000	

B7_1

	0.1000	0.0010	500
	0.5400	0.0054	250
	3.7500	0.0375	125
	49.6000	0.4960	63
0.02	0.5308	0.0053	62
0.03	0.7962	0.0080	58
0.07	1.8578	0.0186	54
0.1	2.654	0.0265	50
0.13	3.4502	0.0345	46
0.15	3.981	0.0398	42
0.5	13.27	0.1327	38
0.02	0.378	0.0038	33
0.03	0.567	0.0057	30
0.07	1.323	0.0132	27
0.1	1.89	0.0189	24
0.13	2.457	0.0246	21
0.15	2.835	0.0284	18
0.5	9.45	0.0945	15
0.02	0.0114	0.0001	14
0.03	0.0171	0.0002	12.5
0.07	0.0399	0.0004	11
0.1	0.057	0.0006	9.5
0.13	0.0741	0.0007	7
0.15	0.0855	0.0009	5.5
0.5	0.285	0.0029	4
	100.0000	1.0000	

Simulations varying only below 25 μm (Case C)

C3_1

	0.1000	0.0010	**500**
	0.5400	0.0054	**250**
	3.7500	0.0375	**125**
0.1	4.96	0.0496	**120**
0.4	19.84	0.1984	**90**
0.5	24.80	0.2480	**63**
0.1	2.65	0.0265	**60**
0.4	10.62	0.1062	**50**
0.5	13.27	0.1327	**38**
0.1	1.89	0.0189	**36**
0.4	7.56	0.0756	**22**
0.5	9.45	0.0945	**15**
0.1	0.06	0.0006	**12**
0.4	0.23	0.0023	**8**
0.5	0.29	0.0029	**4**
	100.0000	1.0000	

C3_2

	0.1000	0.0010	**500**
	0.5400	0.0054	**250**
	3.7500	0.0375	**125**
0.1	4.96	0.0496	**120**
0.2	9.92	0.0992	**90**
0.7	34.72	0.3472	**63**
0.1	2.65	0.0265	**60**
0.2	5.31	0.0531	**50**
0.7	18.58	0.1858	**38**
0.1	1.89	0.0189	**36**
0.2	3.78	0.0378	**22**
0.7	13.23	0.1323	**15**
0.1	0.06	0.0006	**12**
0.2	0.11	0.0011	**8**
0.7	0.40	0.0040	**4**
	100.0000	1.0000	

C4_1

	0.1000	0.0010	**500**
	0.5400	0.0054	**250**
	3.7500	0.0375	**125**
0.08	3.968	0.0397	**120**
0.1	4.96	0.0496	**95**
0.12	5.952	0.0595	**70**
0.7	34.72	0.3472	**63**
0.08	2.1232	0.0212	**62**
0.1	2.654	0.0265	**54**
0.12	3.1848	0.0318	**46**
0.7	18.578	0.1858	**38**
0.08	1.512	0.0151	**34**
0.1	1.89	0.0189	**27**
0.12	2.268	0.0227	**20**
0.7	13.23	0.1323	**15**
0.08	0.0456	0.0005	**13**
0.1	0.057	0.0006	**10**
0.12	0.0684	0.0007	**7**
0.7	0.399	0.0040	**4**
	100.00	1.0000	

C5_1

	0.1000	0.0010	**500**
	0.5400	0.0054	**250**
	3.7500	0.0375	**125**
0.05	2.48	0.0248	**124**
0.1	4.96	0.0496	**105**
0.15	7.44	0.0744	**90**
0.25	12.4	0.1240	**75**
0.45	22.32	0.2232	**63**
0.05	1.327	0.0133	**62**
0.1	2.654	0.0265	**56**
0.15	3.981	0.0398	**50**
0.25	6.635	0.0664	**44**
0.45	11.943	0.1194	**38**
0.05	0.945	0.0095	**35**
0.1	1.89	0.0189	**31**
0.15	2.835	0.0284	**25**
0.25	4.725	0.0473	**20**
0.45	8.505	0.0851	**15**
0.05	0.0285	0.0003	**12**
0.1	0.057	0.0006	**10**
0.15	0.0855	0.0009	**8**
0.25	0.1425	0.0014	**6**
0.45	0.2565	0.0026	**4**
	100.00	1.0000	

C5_2

	0.1000	0.0010	**500**
	0.5400	0.0054	**250**
	3.7500	0.0375	**125**
0.05	2.48	0.0248	**124**
0.07	3.472	0.0347	**105**
0.1	4.96	0.0496	**90**
0.13	6.448	0.0645	**75**
0.65	32.24	0.3224	**63**
0.05	1.327	0.0133	**62**
0.07	1.8578	0.0186	**56**
0.1	2.654	0.0265	**50**
0.13	3.4502	0.0345	**44**
0.65	17.251	0.1725	**38**
0.05	0.945	0.0095	**35**
0.07	1.323	0.0132	**31**
0.1	1.89	0.0189	**25**
0.13	2.457	0.0246	**20**
0.65	12.285	0.1229	**15**
0.05	0.0285	0.0003	**12**
0.07	0.0399	0.0004	**10**
0.1	0.057	0.0006	**8**
0.13	0.0741	0.0007	**6**
0.65	0.3705	0.0037	**4**
	100.00	1.0000	

C6_1

	0.1000	0.0010	**500**
	0.5400	0.0054	**250**
	3.7500	0.0375	**125**
0.02	0.992	0.0099	**113**
0.05	2.48	0.0248	**103**
0.07	3.472	0.0347	**93**
0.1	4.96	0.0496	**83**
0.13	6.448	0.0645	**73**
0.63	31.248	0.3125	**63**
0.02	0.5308	0.0053	**62**
0.05	1.327	0.0133	**56**
0.07	1.8578	0.0186	**50**
0.1	2.654	0.0265	**46**
0.13	3.4502	0.0345	**42**
0.63	16.7202	0.1672	**38**
0.02	0.378	0.0038	**35**
0.05	0.945	0.0095	**31**
0.07	1.323	0.0132	**27**
0.1	1.89	0.0189	**23**
0.13	2.457	0.0246	**19**
0.63	11.907	0.1191	**15**
0.02	0.0114	0.0001	**14**
0.05	0.0285	0.0003	**12**
0.07	0.0399	0.0004	**10**
0.1	0.057	0.0006	**8**
0.13	0.0741	0.0007	**6**
0.63	0.3591	0.0036	**4**
	100.00	1.0000	

C7_1

	0.1000	0.0010	**500**
	0.5400	0.0054	**250**
	3.7500	0.0375	**125**
0.02	0.992	0.0099	**117**
0.03	1.488	0.0149	**108**
0.07	3.472	0.0347	**99**
0.1	4.96	0.0496	**90**
0.13	6.448	0.0645	**81**
0.15	7.44	0.0744	**72**
0.5	24.8	0.2480	**63**
0.02	0.5308	0.0053	**62**
0.03	0.7962	0.0080	**58**
0.07	1.8578	0.0186	**54**
0.1	2.654	0.0265	**50**
0.13	3.4502	0.0345	**46**
0.15	3.981	0.0398	**42**
0.5	13.27	0.1327	**38**
0.02	0.378	0.0038	**33**
0.03	0.567	0.0057	**30**
0.07	1.323	0.0132	**27**
0.1	1.89	0.0189	**24**
0.13	2.457	0.0246	**21**
0.15	2.835	0.0284	**18**
0.5	9.45	0.0945	**15**
0.02	0.0114	0.0001	**14**
0.03	0.0171	0.0002	**12.5**
0.07	0.0399	0.0004	**11**
0.1	0.057	0.0006	**9.5**
0.13	0.0741	0.0007	**7**
0.15	0.0855	0.0009	**5.5**
0.5	0.285	0.0029	**4**
	100.00	1.0000	

Appendix D

Simulations with spheres and ellipses input data

The fourth column represents the percentage while the fifth column represents the grain size. This data was input into GeoDict.

B5_2_I

Major Axis

Initial				
0.64	0.6400	0.0064	0.1458	**250**
3.75	3.7500	0.0375	0.8542	**125**
	4.3900	0.0439	1.0000	

Minor Axis

4.39	4.3900	0.0439	1.0000	**73.53**
	4.3900	0.0439	1.0000	

Spheres

49.60	49.6000	0.4960	0.5188	**63**
26.54	1.327	0.0133	0.0139	**62**
	1.8578	0.0186	0.0194	**56**
	2.654	0.0265	0.0278	**50**
	3.4502	0.0345	0.0361	**44**
	17.251	0.1725	0.1804	**38**
18.90	0.945	0.0095	0.0099	**35**
	1.323	0.0132	0.0138	**31**
	1.89	0.0189	0.0198	**25**
	2.457	0.0246	0.0257	**20**
	12.285	0.1229	0.1285	**15**
0.57	0.0285	0.0003	0.0003	**12**
	0.0399	0.0004	0.0004	**10**
	0.057	0.0006	0.0006	**8**
	0.0741	0.0007	0.0008	**6**
	0.3705	0.0037	0.0039	**4**
	95.6100	0.9561	1.0000	

B5_2_II

Major Axis

Initial				
0.64	0.6400	0.0064	0.0306	**250**
3.75	3.7500	0.0375	0.1792	**125**
16.53	16.5333	0.1653	0.7902	**94**
	20.9233	0.2092	1.0000	

Minor Axis

4.39	4.3900	0.0439	0.2098	**73.53**
16.53	16.5333	0.1653	0.7902	**55.29**
	20.9233	0.2092	1.0000	

Spheres

33.07	33.0667	0.3307	0.4182	**63**
26.54	1.327	0.0133	0.0168	**62**
	1.8578	0.0186	0.0235	**56**
	2.654	0.0265	0.0336	**50**
	3.4502	0.0345	0.0436	**44**
	17.251	0.1725	0.2182	**38**
18.90	0.945	0.0095	0.0120	**35**
	1.323	0.0132	0.0167	**31**
	1.89	0.0189	0.0239	**25**
	2.457	0.0246	0.0311	**20**
	12.285	0.1229	0.1554	**15**
0.57	0.0285	0.0003	0.0004	**12**
	0.0399	0.0004	0.0005	**10**
	0.057	0.0006	0.0007	**8**
	0.0741	0.0007	0.0009	**6**
	0.3705	0.0037	0.0047	**4**
	79.0767	0.7908	1.0000	

B5_2_III

Major Axis

Initial				
0.64	0.6400	0.0064	0.0171	**250**
3.75	3.7500	0.0375	0.1001	**125**
33.07	33.0667	0.3307	0.8828	**94**
	37.4567	0.3746	1.0000	

Minor Axis

4.39	4.3900	0.0439	0.1172	**73.53**
33.07	33.0667	0.3307	0.8828	**55.29**
	37.4567	0.3746	1.0000	

Spheres

16.53	16.5333	0.1653	0.2644	**63**
26.54	1.327	0.0133	0.0212	**62**
	1.8578	0.0186	0.0297	**56**
	2.654	0.0265	0.0424	**50**
	3.4502	0.0345	0.0552	**44**
	17.251	0.1725	0.2758	**38**
18.90	0.945	0.0095	0.0151	**35**
	1.323	0.0132	0.0212	**31**
	1.89	0.0189	0.0302	**25**
	2.457	0.0246	0.0393	**20**
	12.285	0.1229	0.1964	**15**
0.57	0.0285	0.0003	0.0005	**12**
	0.0399	0.0004	0.0006	**10**
	0.057	0.0006	0.0009	**8**
	0.0741	0.0007	0.0012	**6**
	0.3705	0.0037	0.0059	**4**
	62.5433	0.6254	1.0000	

B5_2_IV

Major Axis

Initial				
0.64	0.6400	0.0064	0.0119	**250**
3.75	3.7500	0.0375	0.0695	**125**
49.60	49.6000	0.4960	0.9187	**94**
	53.9900	0.5399	1.0000	

Minor Axis

4.39	4.3900	0.0439	0.0813	**73.53**
49.60	49.6000	0.4960	0.9187	**55.29**
	53.9900	0.5399	1.0000	

Spheres

26.54	1.327	0.0133	0.0288	**62**
	1.8578	0.0186	0.0404	**56**
	2.654	0.0265	0.0577	**50**
	3.4502	0.0345	0.0750	**44**
	17.251	0.1725	0.3749	**38**
18.90	0.945	0.0095	0.0205	**35**
	1.323	0.0132	0.0288	**31**
	1.89	0.0189	0.0411	**25**
	2.457	0.0246	0.0534	**20**
	12.285	0.1229	0.2670	**15**
0.57	0.0285	0.0003	0.0006	**12**
	0.0399	0.0004	0.0009	**10**
	0.057	0.0006	0.0012	**8**
	0.0741	0.0007	0.0016	**6**
	0.3705	0.0037	0.0081	**4**
	46.0100	0.4601	1.0000	

B5_2_V

Initial	Major Axis			
26.54	1.327	0.0133	0.0500	62
	1.8578	0.0186	0.0700	56
	2.654	0.0265	0.1000	50
	3.4502	0.0345	0.1300	44
	17.251	0.1725	0.6500	38
	26.54	0.265	1.0000	

	Minor Axis			
26.54	26.54	0.265	1	22.35

	Spheres			
0.64	0.6400	0.0064	0.0087	250
3.75	3.7500	0.0375	0.0510	125
49.60	49.6	0.4960	0.6752	63
18.90	0.945	0.0095	0.0129	35
	1.323	0.0132	0.0180	31
	1.89	0.0189	0.0257	25
	2.457	0.0246	0.0334	20
	12.285	0.1229	0.1672	15
0.57	0.0285	0.0003	0.0004	12
	0.0399	0.0004	0.0005	10
	0.057	0.0006	0.0008	8
	0.0741	0.0007	0.0010	6
	0.3705	0.0037	0.0050	4
	73.4600	0.7346	1.0000	

B5_2_VI

Initial	Major Axis			
18.90	0.945	0.0095	0.05	35
	1.323	0.0132	0.07	31
	1.89	0.0189	0.1	25
	2.457	0.0246	0.13	20
	12.285	0.1229	0.65	15
	18.9	0.189	1	

	Minor Axis			
18.90	18.9000	0.189	1	8.82

	Spheres			
0.64	0.6400	0.0064	0.0079	250
3.75	3.7500	0.0375	0.0462	125
49.6	49.6	0.4960	0.6116	63
26.54	1.327	0.0133	0.0164	62
	1.8578	0.0186	0.0229	56
	2.654	0.0265	0.0327	50
	3.4502	0.0345	0.0425	44
	17.251	0.1725	0.2127	38
0.57	0.0285	0.0003	0.0004	12
	0.0399	0.0004	0.0005	10
	0.057	0.0006	0.0007	8
	0.0741	0.0007	0.0009	6
	0.3705	0.0037	0.0046	4
	81.1000	0.8110	1.0000	

B5_2_VIII

Initial	Major Axis			
26.54	26.54	0.2654	1	105.4

	Minor Axis			
26.54	1.327	0.0133	0.0500	62
	1.8578	0.0186	0.0700	56
	2.654	0.0265	0.1000	50
	3.4502	0.0345	0.1300	44
	17.251	0.1725	0.6500	38
	26.54	0.2654	1.0000	

	Spheres			
0.64	0.6400	0.0064	0.0087	250
3.75	3.7500	0.0375	0.0510	125
49.60	49.6	0.4960	0.6752	63
18.90	0.945	0.0095	0.0129	35
	1.323	0.0132	0.0180	31
	1.89	0.0189	0.0257	25
	2.457	0.0246	0.0334	20
	12.285	0.1229	0.1672	15
0.57	0.0285	0.0003	0.0004	12
	0.0399	0.0004	0.0005	10
	0.057	0.0006	0.0008	8
	0.0741	0.0007	0.0010	6
	0.3705	0.0037	0.0050	4
	73.4600	0.7346	1.0000	

B5_2_IX

Initial	Major Axis			
18.90	18.9000	0.189	1	59.5

	Minor Axis			
18.90	0.945	0.0095	0.05	35
	1.323	0.0132	0.07	31
	1.89	0.0189	0.1	25
	2.457	0.0246	0.13	20
	12.285	0.1229	0.65	15
	18.9	0.189	1	

	Spheres			
0.64	0.6400	0.0064	0.0079	250
3.75	3.7500	0.0375	0.0462	125
49.6	49.6	0.4960	0.6116	63
26.54	1.327	0.0133	0.0164	62
	1.8578	0.0186	0.0229	56
	2.654	0.0265	0.0327	50
	3.4502	0.0345	0.0425	44
	17.251	0.1725	0.2127	38
0.57	0.0285	0.0003	0.0004	12
	0.0399	0.0004	0.0005	10
	0.057	0.0006	0.0007	8
	0.0741	0.0007	0.0009	6
	0.3705	0.0037	0.0046	4
	81.1000	0.8110	1.0000	

C5_2_V

Initial	Major Axis			
26.54	1.3270	0.0133	0.0500	62
	1.8578	0.0186	0.0700	56
	2.6540	0.0265	0.1000	50
	3.4502	0.0345	0.1300	44
	17.2510	0.1725	0.6500	38
	26.5400	0.2654	1.0000	

Initial	Minor Axis			
26.54	26.5400	0.2654	1.0000	22.35

Initial	Spheres			
0.64	0.6400	0.0064	0.0087	250
3.75	3.7500	0.0375	0.0510	125
49.6	2.4800	0.0248	0.0338	124
	3.4720	0.0347	0.0473	105
	4.9600	0.0496	0.0675	90
	6.4480	0.0645	0.0878	75
	32.2400	0.3224	0.4389	63
18.9	0.9450	0.0095	0.0129	35
	1.3230	0.0132	0.0180	31
	1.8900	0.0189	0.0257	25
	2.4570	0.0246	0.0334	20
	12.2850	0.1229	0.1672	15
0.57	0.0285	0.0003	0.0004	12
	0.0399	0.0004	0.0005	10
	0.0570	0.0006	0.0008	8
	0.0741	0.0007	0.0010	6
	0.3705	0.0037	0.0050	4
	73.4600	0.7346	1.0000	

C5_2_VI

Initial	Major Axis			
18.9	0.9450	0.0095	0.0500	35
	1.3230	0.0132	0.0700	31
	1.8900	0.0189	0.1000	25
	2.4570	0.0246	0.1300	20
	12.2850	0.1229	0.6500	15
	18.9000	0.1890	1.0000	

Initial	Minor Axis			
18.9	18.9000	0.1890	1.0000	8.82

Initial	Spheres			
0.64	0.6400	0.0064	0.0079	250
3.75	3.7500	0.0375	0.0462	125
49.6	2.4800	0.0248	0.0306	124
	3.4720	0.0347	0.0428	105
	4.9600	0.0496	0.0612	90
	6.4480	0.0645	0.0795	75
	32.2400	0.3224	0.3975	63
26.54	1.3270	0.0133	0.0164	62
	1.8578	0.0186	0.0229	56
	2.6540	0.0265	0.0327	50
	3.4502	0.0345	0.0425	44
	17.2510	0.1725	0.2127	38
0.57	0.0285	0.0003	0.0004	12
	0.0399	0.0004	0.0005	10
	0.0570	0.0006	0.0007	8
	0.0741	0.0007	0.0009	6
	0.3705	0.0037	0.0046	4
	81.1000	0.8110	1.0000	

C5_2_VIII

Initial	Major Axis			
26.5	26.54	0.2654	1	105.4

Initial	Minor Axis			
26.5	1.3270	0.0133	0.0500	62
	1.8578	0.0186	0.0700	56
	2.6540	0.0265	0.1000	50
	3.4502	0.0345	0.1300	44
	17.2510	0.1725	0.6500	38
	26.5400	0.2654	1.0000	

Initial	Spheres			
0.64	0.6400	0.0064	0.0087	250
3.75	3.7500	0.0375	0.0510	125
49.6	2.4800	0.0248	0.0338	124
	3.4720	0.0347	0.0473	105
	4.9600	0.0496	0.0675	90
	6.4480	0.0645	0.0878	75
	32.2400	0.3224	0.4389	63
18.9	0.9450	0.0095	0.0129	35
	1.3230	0.0132	0.0180	31
	1.8900	0.0189	0.0257	25
	2.4570	0.0246	0.0334	20
	12.2850	0.1229	0.1672	15
0.57	0.0285	0.0003	0.0004	12
	0.0399	0.0004	0.0005	10
	0.0570	0.0006	0.0008	8
	0.0741	0.0007	0.0010	6
	0.3705	0.0037	0.0050	4
	73.4600	0.7346	1.0000	

C5_2_IX

Major Axis				
18.9	18.90	0.189	1	59.50

Minor Axis				
18.9	0.9450	0.0095	0.0500	35
	1.3230	0.0132	0.0700	31
	1.8900	0.0189	0.1000	25
	2.4570	0.0246	0.1300	20
	12.2850	0.1229	0.6500	15
	18.9000	0.1890	1.0000	

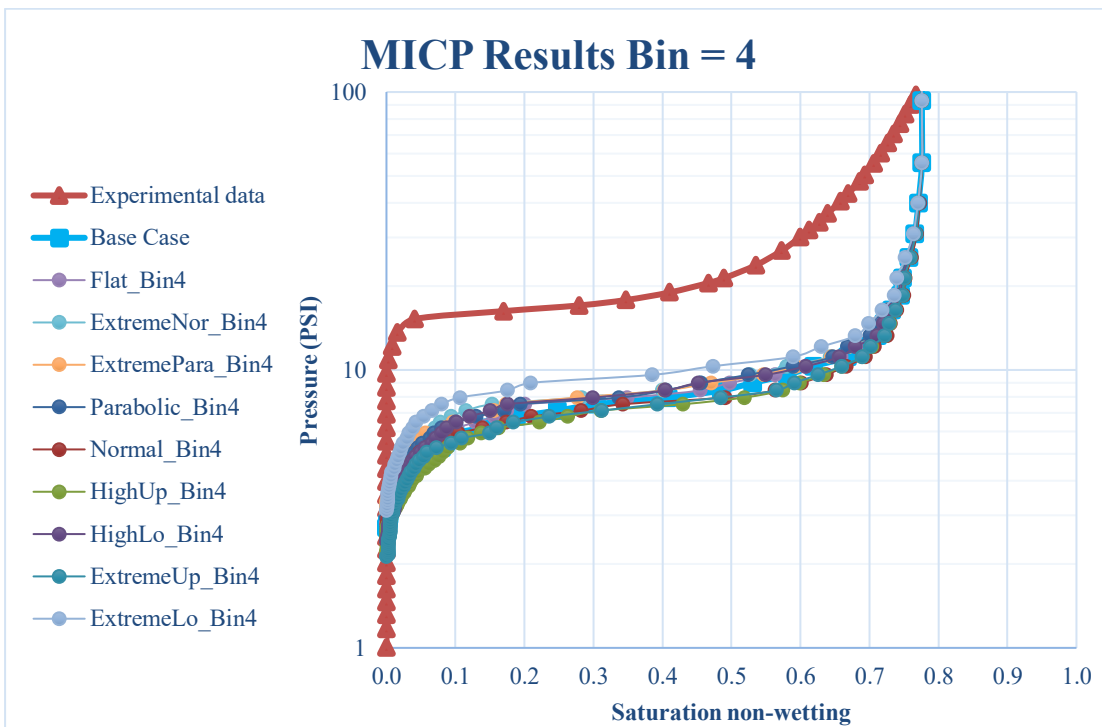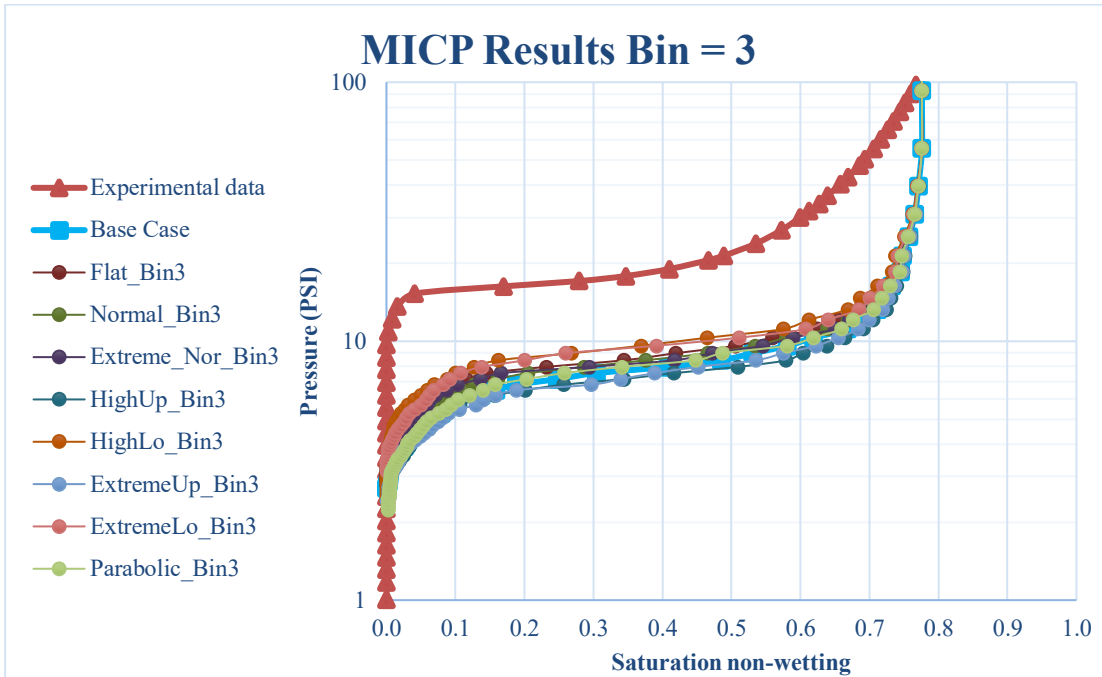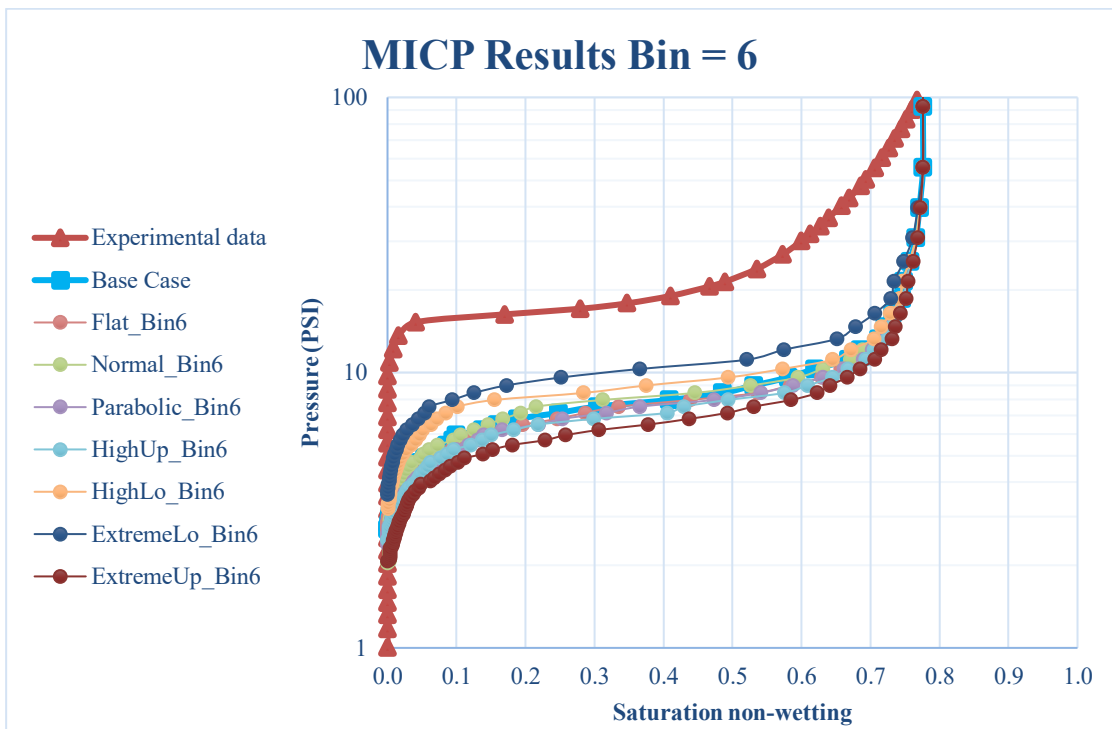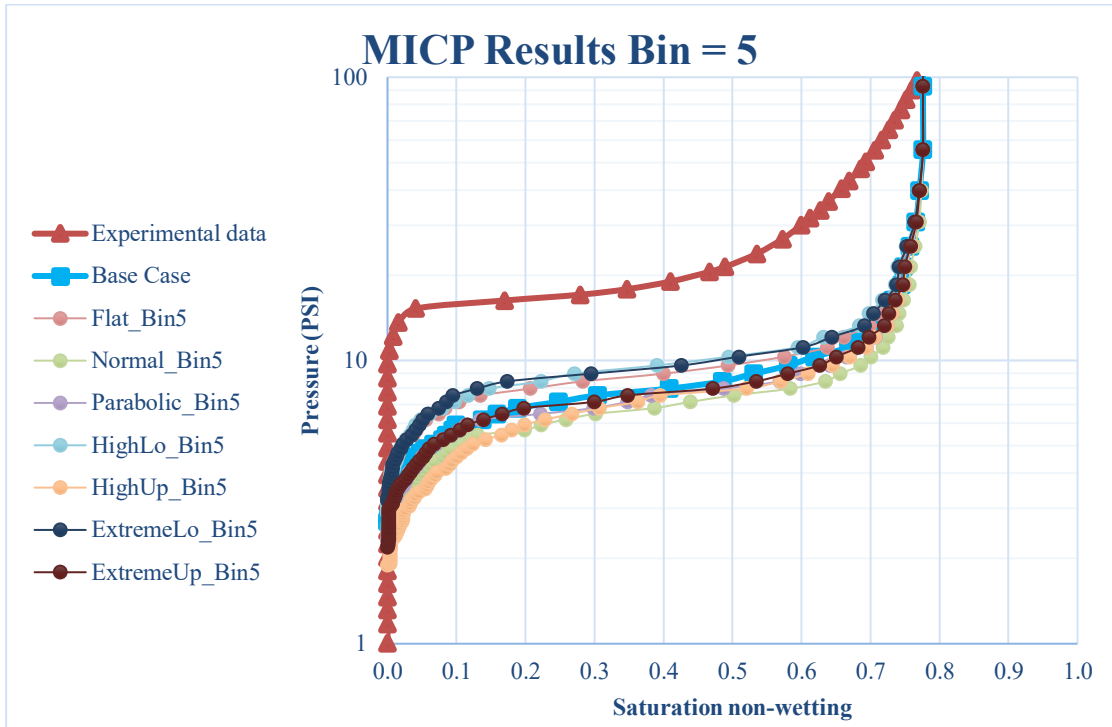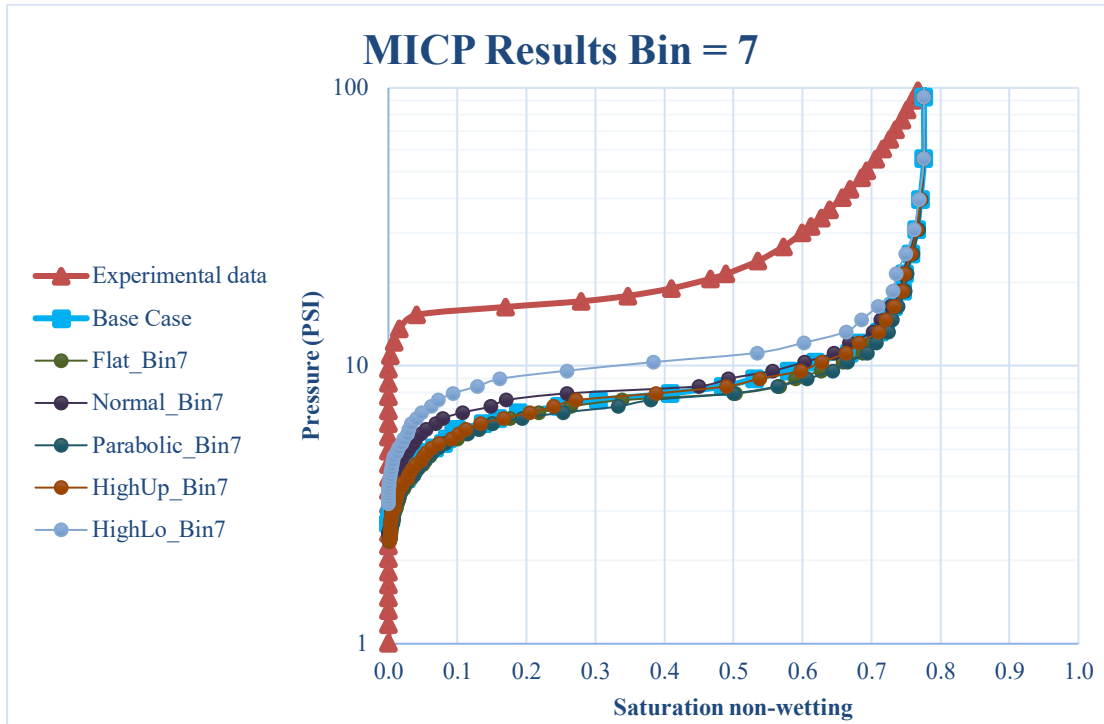| Spheres				
0.64	0.6400	0.0064	0.0079	250
3.75	3.7500	0.0375	0.0462	125
49.6	2.4800	0.0248	0.0306	124
	3.4720	0.0347	0.0428	105
	4.9600	0.0496	0.0612	90
	6.4480	0.0645	0.0795	75
	32.2400	0.3224	0.3975	63
26.54	1.3270	0.0133	0.0164	62
	1.8578	0.0186	0.0229	56
	2.6540	0.0265	0.0327	50
	3.4502	0.0345	0.0425	44
	17.2510	0.1725	0.2127	38
0.57	0.0285	0.0003	0.0004	12
	0.0399	0.0004	0.0005	10
	0.0570	0.0006	0.0007	8
	0.0741	0.0007	0.0009	6
	0.3705	0.0037	0.0046	4
	81.1000	0.8110	1.0000	

Appendix E

Result curves from simulated MICP

Results from simulations based only on spheres

MICP results Bin = 2

MICP Results Bin = 3

Legend: Experimental data, Base Case, Flat_Bin3, Normal_Bin3, Extreme_Nor_Bin3, HighUp_Bin3, HighLo_Bin3, ExtremeUp_Bin3, ExtremeLo_Bin3, Parabolic_Bin3

MICP Results Bin = 4

Legend: Experimental data, Base Case, Flat_Bin4, ExtremeNor_Bin4, ExtremePara_Bin4, Parabolic_Bin4, Normal_Bin4, HighUp_Bin4, HighLo_Bin4, ExtremeUp_Bin4, ExtremeLo_Bin4

MICP Results Bin = 5

Legend:
- Experimental data
- Base Case
- Flat_Bin5
- Normal_Bin5
- Parabolic_Bin5
- HighLo_Bin5
- HighUp_Bin5
- ExtremeLo_Bin5
- ExtremeUp_Bin5

MICP Results Bin = 6

Legend:
- Experimental data
- Base Case
- Flat_Bin6
- Normal_Bin6
- Parabolic_Bin6
- HighUp_Bin6
- HighLo_Bin6
- ExtremeLo_Bin6
- ExtremeUp_Bin6

Results from the cases with spheres when the variation occurred under a certain grain dimension

Simulations varying only below *38 μm* (Cases A)

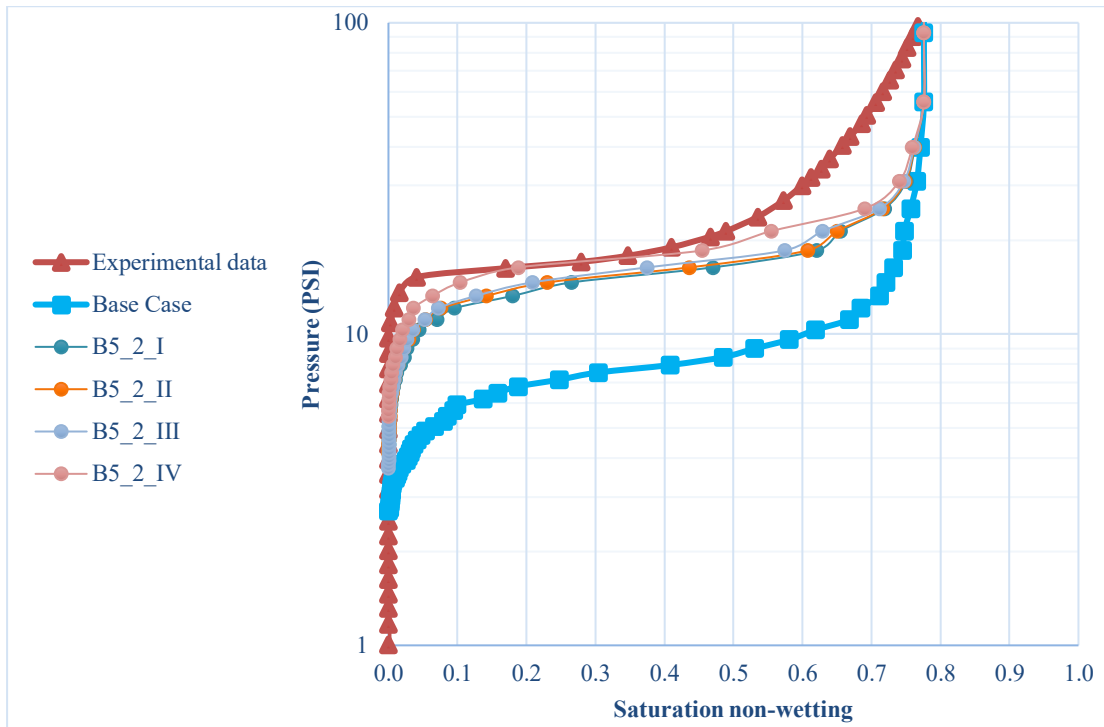Simulations varying only below 63 *µm* (Cases B)

Simulations varying only below *125 µm* (Cases C)

Results from the cases with spheres and ellipses when the variation was above 63 _μm_

Results from the cases with spheres and ellipses when the variation was below 63 _μm_